Title

Plasmonics in the near-infrared : spatial, spectral, and temporal studies of surface plasmon polaritons

Author

Tetz, Kevin

Publication Date

2006

UNIVERSITY OF CALIFORNIA, SAN DIEGO

Plasmonics in the Near-Infrared: Spatial, Spectral, and Temporal studies of Surface Plasmon Polaritons

A dissertation submitted in partial satisfaction of the
requirements for the degree Doctor of Philosophy
in
Electrical Engineering (Applied Physics)

by

Kevin Tetz

Committee in charge:

Professor Yeshaiahu Fainman, Chair
Professor Dimitry Basov
Professor Lu Jeu Sham
Professor Harry Wieder
Professor Edward Yu

2006

The dissertation of Kevin Tetz is approved, and it is acceptable in quality and form for publication on microfilm:

Lu J. Sham

Y Fainman

Chair

University of California, San Diego

2006

DEDICATION

There are many people who have helped me along the way, and I owe my deepest thanks and gratitude to you all. To Emily and my family: I would never have made it without your support. To my advisor, Professor Yeshaiahu Fainman, who made it all possible; and Professor Harry Wieder, who helped guide me every step of the way: you both taught me more than you will ever know. And to the entire Ultrafast and Nanoscale Optics group, past and present, who aided in nearly every experiment I attempted: in particular, I need to thank Dr. Lin Pang, who deserves all the credit for making the the best samples; Dr. Rostislav Rokitski, who shared his expertise in time-resolved spectroscopy; and Maziar Nezhad, who helped take this work in several new directions.

Thanks again
Kevin Tetz

TABLE OF CONTENTS

LIST OF FIGURES

LIST OF TABLES

ACKNOWLEDGEMENTS

The text of Chapter Two in part is a reprint of the material as it appears in the following publications:

- M. Nezhad, K. Tetz, and Y. Fainman, "Gain assisted propagation of surface plasmon polaritons on planar metallic waveguides", *Optics Express* **12**, 4072 (2004).

The dissertation author was the primary researcher and author. The co-authors listed in these publications directed and supervised the research which forms the basis for these chapter.

The text of Chapters Four and Seven in part is a reprint of the material as it appears in the following publications:

- K.A. Tetz, V. Lomakin, L.Pang, M. Nezhad, and Y. Fainman, "Polarization weighting of Fano-type transmission through metallic nanohole arrays", *submitted, Optics Express.*
- K. Tetz, L. Pang, and Y. Fainman, "High-resolution surface plasmon resonance sensor based on linewidth-optimized nanohole array transmittance",Opt. Lett. 31, 1528-1530 (2006).

The dissertation author was the primary researcher and author. The co-authors listed in these publications directed and supervised the research which forms the basis for these chapter.

The text of Chapters Five and Six in part is a reprint of the material as it appears in the following publication:

- Tetz K., Rokitski R., Nezhad M. and Fainman Y. "Excitation and Direct Imaging of Surface Plasmon Polariton Modes in a Two-dimensional Grating". *Applied Physics Letters*, vol. 86, no.11 2005.

- Rokitski R.[†], Tetz K.[†] and Fainman Y. "Propagation of Femtosecond Surface Plasmon Polariton Pulses on the Surface of a Nanostructured Metallic Film: Space-Time Complex Amplitude Characterization", Physical Review Letters, 95, 177401, 2005.

The dissertation author was the primary researcher and author. The co-authors listed in these publications directed and supervised the research which forms the basis for this chapter.

VITA

2000	Bachelor of Sceince, Electrical Engineering (Solid State Electronics), Brown University Richard A. Ionata Award for creativity and originality in a thesis Joseph A. Loferski Award for potential in graduate research
2002	Master of Science (Applied Physics: Photonics) University of California, San Diego
2006	Doctor of Philosophy (Applied Physics: Photonics) University of California, San Diego

PUBLICATIONS

K.A. Tetz, V. Lomakin, L.Pang, M. Nezhad, and Y. Fainman, “Polarization weighting of Fano-type transmission through metallic nanohole arrays”, *submitted, Optics Express.*

K. Tetz, L. Pang, and Y. Fainman, “High-resolution surface plasmon resonance sensor based on linewidth-optimized nanohole array transmittance”,Opt. Lett. 31, 1528-1530 (2006).

Rokitski R., Tetz K. and Fainman Y. “Propagation of Femtosecond Surface Plasmon Polariton Pulses on the Surface of a Nanostructured Metallic Film: Space-Time Complex Amplitude Characterization”, Physical Review Letters, 95, 177401, 2005.

Tetz K., Rokitski R., Nezhad M. and Fainman Y. “Excitation and Direct Imaging of Surface Plasmon Polariton Modes in a Two-dimensional Grating. Applied Physics Letters”, vol. 86, no.11 2005.

Above featured in: Editor’s Choice: Highlights of recent literature, Science, vol. 307, p. 1841 (2005).

C.Lynch, E. Chason, R. Beresford, L. B. Freund, K. Tetz, and K. W. Schwarz,, “Limits of strain relaxation in InGaAs/GaAs probed in real time by in-situ wafer curvature measurement”, J. Appl. Phys. 98, 073532 (2005).

C. Chen, K. Tetz, W. Nakagawa, and Y. Fainman, “Wide Field of View GaAs/AlxOy 1-D Photonic Crystal Filter”, Appl. Opt. Vol. 44, no. 8, pp. 1503-1511 (2005).

L. Pang, Y. Shen, K. Tetz and Y. Fainman “PMMA quantum dots composites fabricated via use of pre-polymerization”, Opt. Express, vol.13, no.1, January 2005, pp.44-9.

M. Nezhad, K. Tetz, and Y. Fainman, “Gain assisted propagation of surface plasmon polaritons on planar metallic waveguides”, Opt. Exp. 12, 4072 (2004).

C. Chen, K. Tetz, and Y. Fainman, “Resonant-Cavity-Enhanced (RCE) Quantum Efficiency PIN Photodiode with Flat-Top Passband Filter Functionality”, Appl Opt. Vol. 44, Issue 29, pp. 6131-6140 (October 2005).

CONFERENCE PAPERS AND PRESENTATIONS

K.A. Tetz, and Y. Fainman, ”Nanophotonic structures and devices with polymers”, American Chemical Society National Meeting C3-386, September 2006.

K.A. Tetz, Lin Pang, Maziar Zezhad, and Yeshaiahu Fainman, ”Optofluidic Plasmonics” Proc. SPIE 6124, 612404, August 2006.

K.A.Tetz, R. Rokitski, M. Nezhad, and Y. Fainman, ”Characterization of surface plasmon polariton pulse propagation on thin metallic films and two dimensional nanohole arrays,” IEEE/LEOS Annual Meeting, Sydney, Australia, November 2005.

K. A.Tetz, R. Rokitski, Y. Fainman; ”Spatio-Temporal Characterization of Ultrashort Surface Plasmon Polariton Pulses Propagating in Two-Dimensional Nanohole Arrays”, OSA NPIS, San Diego, CA, April 2005.

K. Tetz, R. Rokitski, M. Nezhad, and Y. Fainman, ”Excitation and Direct Imaging of Surface Plasmon Polariton Modes in the Near-Infrared”, IEEE/LEOS Annual Meeting, Rio Grande, Puerto Rico, Nov 2004.

M.P. Nezhad, K. Tetz, U. Levy, Y. Fainman ”Propagation of Surface Plasmon Polaritons on the Boundary of a Metal and a Gain Medium”, IEEE IEEE/LEOS Annual Meeting, Rio Grande, Puerto Rico, Nov 2004.

R. Rokitski, K.A. Tetz, and Y. Fainman ”Spatial and Temporal Imaging of Ultrashort Surface Plasmon Polariton Pulses”, IEEE/LEOS Annual Meeting, Rio Grande, Puerto Rico, Nov 2004.

Y. Sheng, L.Pang, K. Tetz and Y. Fainman ”Characterization of PMMA quantum dot composite fabricated by pre-polymerizing method”, SPIE Annual Meeting, Denver, Aug. 2004.

U. Levy, W. Nakagawa, K. Tetz, C. H. Tsai, M. Nazhad, S. Cheng "Nanophotonics: materials and devices", Photonics West 2004, San-Jose, California.

W. Nakagawa, K. Tetz, Y. Fainman, "Design of near-field optical nanostructure for enhanced second-harmonic generation", CLEO/QELS, Baltimore, June 2003.

K. Tetz, W. Nakagawa,, C.-H. Tsai, C.-H. Chen, S. Laut, L. Pang, Y. Fainman, "Optical resonant filters based on photonic crystal nanocavities", OSA Annual Meeting , Orlando, Sept. 2002.

K. Tetz, C.-H. Chen, H. H. Wieder, W. Nakagawa and Y. Fainman, "Design, Fabrication and Characterization of Narrowband Angularly-Insensitive Resonant Cavity Filter", IEEE/LEOS Annual Meeting, Glasgow, Scotland, Nov. 2002.

Y. Fainman, W. Nakagawa, C.-H. Chen, K. Tetz, L. Pang, and C.-H. Tsai, "Artificial Materials for Nanophotonics, IEEE/LEOS 13th Annual Workshop on Interconnections Within High Speed Digital Systems, Santa Fe, May 2002.

Chason E, Yin J, Tetz K, Beresford R, Freund LB, Gonzalez MU, Floro JA. "In situ measurements of stress relaxation during strained layer heteroepitaxy". Self-Organized Processes in Semiconductor Alloys. Symposium (Materials Research Society Symposium Proceedings Vol.583). Mater. Res. Soc. 2000, pp.167-75. Warrendale, PA, USA

PATENT

Optical Sensing based on Surface Plasmon Resonances in Nanostructures

ABSTRACT OF THE DISSERTATION

Plasmonics in the Near-Infrared: Spatial, Spectral, and Temporal studies of Surface Plasmon Polaritons

by

Kevin Tetz
Doctor of Philosophy in Electrical Engineering (Applied Physics)
University of California, San Diego, 2006
Professor Yeshaiahu Fainman, Chair

The field of nanophotonics is finding myriad applications in telecommunications and information technology, microscopy, lighting, and sensing. There is general interest in highly confined and nanoscale optical modes for a number of these applications, with a particular interest in structures that confine electromagnetic fields and energy in volumes smaller than than the free space wavelength. Plasmonics, the utilization of coupled photon-plasmon waves in systems with free electrons, in micro- and nanoscale geometric structures has attracted significant recent attention for these purposes.

In this dissertation we explore surface plasmon-polariton (SPP) fields, on nanostructured metal-dielectric boundaries, at frequencies in the near-infrared portion of the electromagnetic spectrum. To couple to these SPP modes from free-space propagating light, arrays of nanoholes etched in metal films are employed. We then utilize a variety of experimental techniques that investigate the physics of SPPs in space, time, and frequency. Various physical phenomena, including enhanced transmission effects and resonantly excited and propagating surface electromagnetic modes, are observed, studied, and explained.

We begin by discussing the basics of SPP excitation and modal propagation properties and present an analytical investigation of gain assisted propagation. We next investigate the spatial and spectral frequency dependent transmission through nanohole arrays. We present novel experimental and analytic results of polarization dependent Fano-type lineshape profiles present in enhanced transmission due to SPP excitation. We further present a method for excitation and direct imaging of SPPs from nanohole arrays and demonstrate coupling to a variety of modes with different in-plane propagating wavevector components. This method is extended to incorporate ultrashort laser pulse excitation and enables space-time imaging of ultrashort SPP fields, both in spatial amplitude and phase, with femtosecond time scale resolution. We ultimately describes the application of this work to the making of a highly parallelized sensor to measure chemical reactions at a surface by generating spatially resolved, reaction dependent, spatial and spectral frequency information.

I

Introduction

I.A Optics on the nanoscale

The field of nanophotonics is finding myriad applications in information technology, health care, lighting, and sensing. This dissertation explores the electrodynamics of surface plasmon-polariton fields on nanostructured metal-dielectric boundaries and describes how to make a sensor to measure chemical reactions at a surface by generating spatially resolved, reaction dependent, spatial and spectral frequency information.

Experts predict that nanolithography will reach a resolution of 16 nm by 2020, and that both top-down and bottom-up integration methods will become feasible, enabling reliable, scalable, power-efficient and cost-effective methods for the miniaturization of future systems. Over the past decade, significant progress has been made in the engineering of inhomogeneous composite materials (e.g., dielectrics, semiconductors, metals, organic, quantum dots) with unique optical properties such as polarization and spectral dispersion, negative refraction, nonlinear polarization and quantum interference.

Recently, nanophotonic structures that involve optical modes at the interface between metallic and dielectric materials have attracted renewed and increasing attention. This is part of a general interest in highly confined or nanoscale optical modes in any number of physical systems. In plasmonics specifically, the confinement is due to the strong light-matter interactions in systems with free electrons in micro- or nanoscale geometric structures. At these interfaces there is intrinsic field localization that facilitates nanoscale waveguiding, and there is the potential for full optical confinement on the nanoscale in three dimensions. Among other things, this may reduce average power requirements for nonlinear wave mixing and enable sub-diffraction limited imaging and waveguiding.

These unique features of surface plasmonic fields could lead to photonic devices that are much more compact than those achievable with current optical refraction technologies. Indeed, they may bridge the gap between photonics, biochemical sensing and CMOS-based electronics technologies. However, there are a number of fundamental issues still being addressed in the attempt to make practical plasmonic optical elements for future information technologies.

I.B Electromagnetic surface waves, surface plasmons, and plasmon polaritons

The eigenmodes of collective oscillations of the quasi-free electrons in metals are called plasmons. Because electrons carry a charge, these oscillations are inherently associated with an electromagnetic field. Therefore a theoretical description has to include this interplay of charges and fields. The boundary conditions for electromagnetic fields lead to different conditions for the occurrence of plasmons for the cases of bulk material, planar metal-dielectric interfaces and metal particles. It is therefore useful to distinguish these modes by speaking of bulk, surface or particle plasmons, respectively.

There are a number of geometries commonly encountered in the study of SP resonant modes, and these are illustrated in Fig. I.1. One common manifestation is in metallic resonant nanoparticles and spheroids, which have been studied extensively, most notably for their ability to enhance nonlinear wave mixing be-

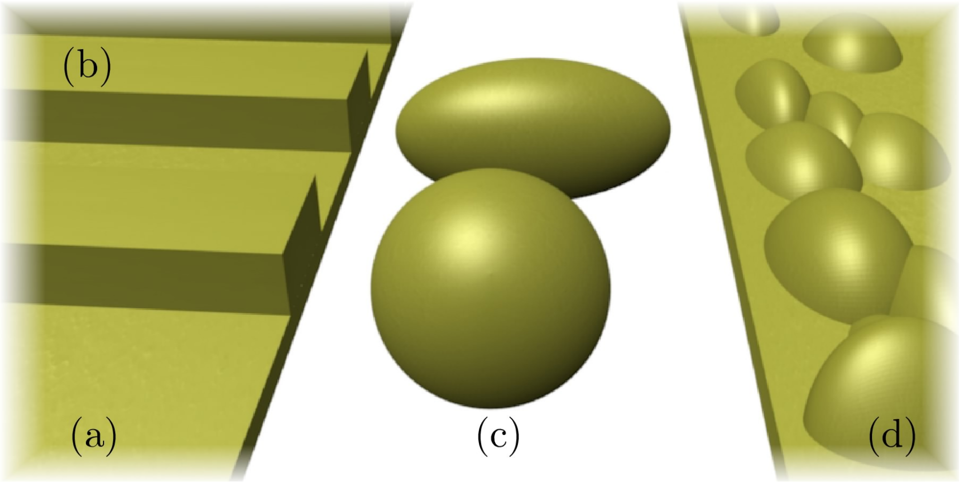

Figure I.1: Different plasmon resonance nanostructure geometries. (a) planar metal surface (b) currogated surface/grating (c) spherical and spheroidal nanoparticles (d) randomly rough metal surface

cause of the plasmonic resonance field enhancements (huge field enhancements also occur in various places in the case of a "rough" metallic surface). Such structures have historically been self-assembled in nature, and only recently, with advances in nanoscale fabrication and characterization techniques, has it become increasingly possible to study "engineered" structures designed to have specific resonant properties.

In this work, the focus is on on surface plasmons polaritons (SPPs), i.e., the electromagnetic eigenmodes at planar (or currogated) metal-dielectric interfaces.[1] SPPs in the optical regime have been extensively studied for several decades [1]. Historically, these surface plasmon modes were studied as early as the beginning of the 20th century by Zenneck (1907) and Sommerfeld (1909) in connection with wireless telegraphy and hence are sometimes called Zenneck modes. These early investigations focused on frequencies much smaller than that of visible

---

[1] There is considerable inconsistency in the literature in regards to the naming of these surface waves. In many cases authors refer to a surface plasmon or "SP", and indeed this is the term used by the most authoritative text on the subject by Raether [1]. We prefer to adopt the term surface plasmon polarition, or SPP, as is conveys the propagating nature of the excitation. This is in contrast to localized resonances that are present in plasmonic systems of various other geometries. For reference, there are 517 citations of "surface plasmon polariton" versus 11,777 for "surface plasmon".

light, where the optical properties of metals are very well described in terms of the Drude-Sommerfeld model, and the phenomenological difference of plasmonic surface waves and plane electromagnetic waves in free-space is very small. Because our work deals with optical properties, these early works are therefore of limited use despite the fact that the mathematical treatments are similar to those in the optical regime. There has been a variety of recent work that, among other things, has explored SPPs potential for building various integrated optical devices [2][3]. The intrinsic mode confinement, due to their surface nature, may have potential advantages for building sub-diffraction limited waveguides [4] and in facilitating full three-dimensional optical confinement[5][6].

Another closely related topic is that of negative index metamaterials. Since the paper “Experimental verification of a negative index of refraction” by Shelby, Smith and Shultz [7] in 2001, there have been over 818 citations as of October 2006. Also, “Negative refraction makes a perfect lens” by Pendry [8]in 2000 has 869 citations, in which a plasmonic layer is used to enhance evanescent wave propagation and enable subdiffraction limit resolution. A number of other interesting applications include:

- Biochemical sensors (linear/affinity binding, SERS, SECARS)
- optical nonlinearities: SHG, etc.
- near field probes and data storage
- enhanced light extraction/detection for detectors and thermo/photovoltaics
- sub diffraction limit lithography
- modulators
- spectral filters
- optical interconnects

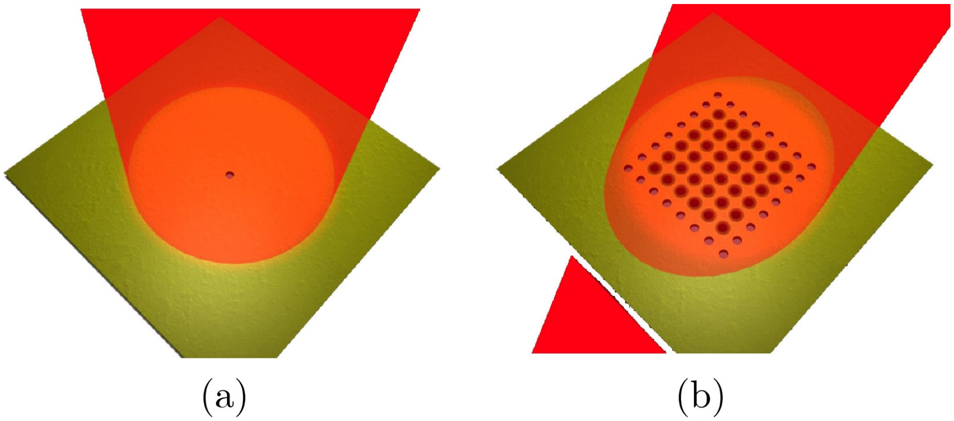

(a) (b)

Figure I.2: Schematic of light transmission: (a) through a small hole (a) through a hole array was reported to be orders of magnitude greater than the Bethe theory

I.B.1 Subwavelength hole arrays

The scientific community's interest in plasmonics was also recently sparked with the discovery of enhanced light transmission through nanoholes in an array or with surrounding surface corrugations. Even with a hole far below the cutoff of for the wavelength of the incident field, due to the resonant SPP excitation the amount of light scattered through the holes was several times larger than expected for an isolated subwavelength hole.

In 1998, Ebbesen and coworkers showed that arrays of subwavelength-diameter holes in metal films have extraordinary transmission properties, as illustrated in Fig. I.2 This seminal work (Refs. [9, 10, 11, 12], for example) sparked much interest. Indeed, at present, it has been cited at least 740 times[2] since its publication. Their transmission spectrum is strongly peaked, with intensities that can be an order of magnitude larger than expectedfrom standard electromagnetic theory for subwavelength apertures, developed by Bethe and adapted by Bouwkamp [13, 14]. The radiated diffraction pattern can be controlled by resonantly excited SPPs [15]. The extraordinary large peak transmission is commonly explained by resonant excitation of SPPs on the hole array. However, there

---

[2] Citations listed in the ISI Web of Science Database.

has been some debate on alternative explanations in the literature: one paper found an anti-correlation between optical transmission peaks and excitation of SPPs in 1-D arrays of slits [16], another focussed on the role of phase singularities, a third showed the non-negligible influence of the holes themselves through their shapes [17] and a fourth, coauthor of Ref. [9], in an interesting change of opinion, now advocates a diffracted evanescent wave model [18]. Most of this debate can probably be resolved by admitting that each of the viewpoints is a valid description of some part of the problem, and that SPPs, however useful a concept to explain a number of the optical properties of the nanohole arrays, may fall short in some respects or at particular frequencies. It is interesting to note that most of the optical properties of nanohole arrays can already be accounted for qualitatively by allowing for a (small) direct transmission through the holes, next to the indirect resonant- SPP contribution; This explains, for instance, the typical asymmetric peaks in the hole array spectra, which are similar to Fano resonances occurring in atomic physics [19]. The extension and elucidation of this concept is one of the major contributions of this work.

I.C Dissertation outline

This dissertation continues the investigation of both the basic physics of nanohole transmission mechanisms, as well as the extension to a sensing device application. To these ends, the dissertation is organized in the following manner.

- In Chapter II we discuss the basics of SPP propagation on a planar metal dielectric interface. This includes an overview of the basic propagation characteristics, as well as a summary of the commonly employed methods for optical coupling to these modes. In addition, we extend the basic theory with an analytic derivation of propagation characteristics of SPP waves in proximity to a gain region that can increase the propagation length.

- In Chapter III we describe the fabrication techniques used in making the nanoscale metallic structures used throughout this work. The various material deposition techniques, as well as e-beam and a holographic lithography techniques, are described. The latter is described in some detail, with a number of example structures, as the tool facilitating this capability was advanced during the course of this work. We finish with a brief description of the etching methods, and give a list of the primary sample structures utilized that account for the vast majority of the presented results.

- Chapter IV consists of the detailed study of the spectral transmission properties of the metal nanohole array. In particular, the polarization dependence of both resonant and nonresonant transmission properties detailed both experimentally and analytically.

- In Chapter V we describe the simultaneous excitation and direct far field imaging of the scattering from SPP modes in a two-dimensional metallic hole array grating. Conditions for the coupling and imaging are discussed, where the coupling is shown to be consistent with both measured and calculated dispersion relations. Excitation is accomplished at several different wavelengths [from 1.31 to 1.57 μm], incidence angles, and grating periods, enabling the observation of a number of distinct modes with various in-plane wave vectors.

- Chapter VI is an investigation of excitation and propagation of femtosecond SPP pulses using a time-resolved spatial heterodyne imaging technique to obtain spatial distributions of the electromagnetic field amplitude and phase versus time. This type of dynamic three dimensional characterization of the surface electromagnetic field can provide invaluable insight on SPP excitation and propagation along the surface of the film.

- In Chapter VII we investigate the use of metallic nanohole transmission in sensing applications. We demonstrate a surface plasmon resonance (SPR) sensor based on the nanohole array presented in previous chapters and specifically show polarization properties that facilitate narrowing the transmission linewidth (and hence maximize resolution) while operating in a regime that facilitates large area, with high spatial resolution, imaging.

- Chapter VIII summarizes the major contributions of this work and gives suggestions for future work to extend the results summarized herein.

II

Surface plasmon polaritons at the metal-dielectric interface

In this chapter, before embarking on the main topics of interest, it will be helpful to review the basics optical properties of metals. We then look at the properties of propagating SPPs at a planar interface, and further extend the conventional analysis to include a gain media adjacent to a metal layer for SPPs with increased propagation lengths. We then summarize the basic mechanisms involved in coupling of light to SPP modes- which will lead into the properties of nanohole arrays that will follow later in this dissertation.

II.A Optical properties of metal nanostructures

The understanding of the optical properties of metal nanostructures requires both electrodynamics and solid state theory. The basic concepts of these disciplines needed for the following chapters will be briefly introduced here. The material properties entering the electrodynamics treatment have to be explained by solid state theory. For more thorough treatments the reader is directed to more authoritative textbooks on electrodynamics by Jackson [20] and on solid state physics by Ashcroft and Mermin [21].

II.A.1 Optical properties of metals

A simple model for the behavior of free electrons in metals was developed by Drude (1900) based on the kinetic gas theory. It assumes independent and free electrons with a common relaxation time. Sommerfeld incorporated corrections originating from the Pauli-exclusion principle (Fermi-Dirac distribution). This free-electron model was later modified to include minor corrections from the band-structure of matter (effective mass) and termed the quasi-free-electron model. This Drude-Sommerfeld model describes very successfully many properties of metals despite its drastic assumptions. At optical frequencies it often fails due to the presence of interband transitions.

The basic picture of the properties of metals in the framework of this theory is a gas of independent electrons. These electrons move freely between independent collisions with unspecified collision centers (lattice ions, other electrons, defects, phonons, etc.) which occur at some average rate. Each collision leads to a complete loss of directional information and results in a random orientation of the electron velocity afterwards.

In an external field the electrons are accelerated between collisions resulting in a drift motion. Only electrons near the Fermi level contribute because the Pauli exclusion principle does not allow deeper lying electrons to change their electronic state. Band-structure corrections lead to a modification of this motion. These corrections are customarily incorporated into an effective mass m*, which is in general different from the free-electron mass m_e. Many properties of real metals, including their optical properties as described by the frequency dependent dielectric function ϵ, are quite well predicted from this simple model. The resulting equation for the dielectric function is:

$$\epsilon(\omega) = \epsilon_\infty - \frac{\omega_p^2}{\omega^2 - i\omega\gamma} \tag{II.1}$$

with ω_p the so-called plasma frequency and γ the electron relaxation rate. ϵ_∞ includes the contribution of the bound electrons to the polarizability. The plasma frequency ω_p is given by

$$\omega_p^2 = \frac{4\pi N e^2}{m^* \epsilon_\infty} \tag{II.2}$$

with N and m^* being the density and effective mass of the conduction electrons, respectively.

At the plasma frequency, the of collective oscillations of the quasi-free electrons oscillate resonantly, and these eigenmodes are deemed plasmons. Boundary conditions lead to different conditions for the occurrence of plasmons when the infinite metal is terminated by a surface. We explore the properties of these surface plasmons in the next section.

II.A.2 SPPs at a metal-dielectric interface

SPPs are electromagnetic modes bound to metal-dielectric interfaces, involving charges in the metal and electromagnetic fields in both media. The field intensity in the metal as well as the dielectric medium falls off exponentially in the direction normal to the surface. In the plane of the interface, the field intensity and charge distribution in the metal propagates as a longitudinal wave along the surface. Hence, SPPs propagate along the interface with electromagnetic fields, energy and charges highly localized within the interface area. Their properties depend strongly on the exact properties of both the metal (complex dielectric function, corrugations, roughness) and the dielectricum (refractive index). The strong localization of electromagnetic energy along the metal-dielectric interface can be used to guide light in small structures (Krenn et al., 2001).

The basics of SPP propagation on an planar surface are summarized in Raether [1]. The boundary between the dielectric medium and the metal is lies in the x-y plane as shown in Fig. II.1. We will assume SPP propagation in the positive x direction with the fields tailing off into the positive and negative z directions,

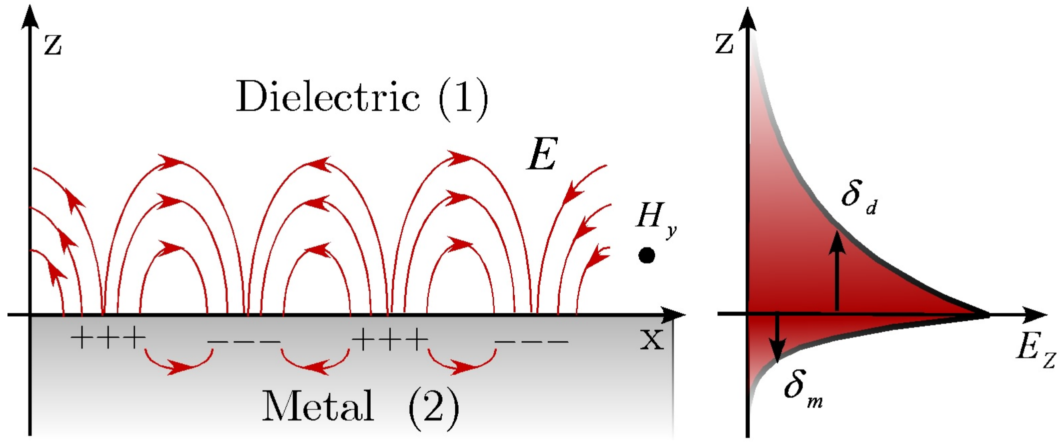

Figure II.1: SPP modes at a smooth metal-dielectric interface. The electromagnetic modes are TM polarized, and the fields are maximal at the interface and decay exponentially into both media with characteristic lengths δ_m and δ_d determined by the frequency and material parameters.

described by the following TM wave:

$$\left\{\begin{array}{l} \mathbf{E}_j = (E_x, 0, E_{z_j}) \exp(i(k_x x + k_{z_j} z - \omega t)) \\ \mathbf{H}_j = (0, H_y, 0) \exp(i(k_x x + k_{z_j} z - \omega t)) \end{array}\right. , \ j = 1, 2, \tag{II.3}$$

From Maxwell's equations and continuity at the boundary, we can write the following relationships:

$$\left\{\begin{array}{l} \frac{\varepsilon_1}{k_{z_1}} = \frac{\varepsilon_2}{k_{z_2}} \\ k_x^2 + k_{z_j}^2 = \varepsilon_j k_0^2 \\ E_x = \frac{k_{z_j}}{\omega \varepsilon_j} H_y, E_j = -\frac{k_x}{\omega \varepsilon_j} H_y \end{array}\right. , \ j = 1, 2, \tag{II.4}$$

where $k_0 = \frac{\omega}{c}$ is the free space wavenumber of the incident excitation photon. From Eqs. II.4, the SPP dispersion relations can be derived (see, for example, Ref. [1]):

$$\left\{\begin{array}{l} k_x^2 = k_0^2 \frac{\varepsilon_1 \varepsilon_2}{\varepsilon_1 + \varepsilon_2} \\ k_{z_j}^2 = k_0^2 \frac{\varepsilon_j^2}{\varepsilon_1 + \varepsilon_2} \end{array}\right. \tag{II.5}$$

The condition for Eq. II.5 to describe a wave bound to the interface is that $\Im(k_{z_j} > 0)$ (i.e. the solution decays away from the boundary). Assuming for the moment that ε_1 and ε_2 have negligible imaginary parts, this requires that . This condition is satisfied if region 1 is a low loss dielectric with positive real permittivity and region 2 is a low loss metal having a permittivity with a negative real part (i.e. the excitation frequency is less than the plasma frequency).

$$\delta_{\mathrm{d,m}} = \frac{1}{k_0}\left(\frac{\varepsilon_1 + \varepsilon_2'}{(\varepsilon_{1,2}')^2}\right)^{\frac{1}{2}} \tag{II.6}$$

Assuming that region 2 has a complex permittivity and (which is valid for low loss metals near the plasma resonance), Eq. II.5 can be written as:

$$k_x = k_x' + ik_x'' = k_0\left(\frac{\varepsilon_1(\varepsilon_2' + i\varepsilon_2'')}{\varepsilon_1 + \varepsilon_2' + i\varepsilon_2''}\right)^{\frac{1}{2}} \simeq k_0\left(\frac{\varepsilon_1\varepsilon_2'}{\varepsilon_1 + \varepsilon_2'}\right)^{\frac{1}{2}} + ik_0\left(\frac{\varepsilon_1\varepsilon_2'}{\varepsilon_1 + \varepsilon_2'}\right)^{\frac{3}{2}}\frac{\varepsilon_2''}{2(\varepsilon_2')^2}. \tag{II.7}$$

$$k_x^{'} = k_0\left(\frac{\varepsilon_1\varepsilon_2'}{\varepsilon_1 + \varepsilon_2'}\right)^{\frac{1}{2}} \tag{II.8}$$

$$k_x^{''} = k_0\left(\frac{\varepsilon_1\varepsilon_2'}{\varepsilon_1 + \varepsilon_2'}\right)^{\frac{3}{2}}\frac{\varepsilon_2^{''}}{2(\varepsilon_2^{'})^2} \tag{II.9}$$

The basic dispersion is shown in Fig. II.A.2. SPP waves can propagate along a metallic surface with a broad frequency spectrum from $\omega = 0$ to $\omega = \omega_p/\sqrt{1+\epsilon_1}$ depending on the wave vector $\mathbf{k}$.

This dispersion relation $\omega(\mathbf{k})$ defines a curve that lies to the right of the light line $\omega = ck_x$, meaning that the surface waves have a longer wave vector than the optical waves with the same energy $\hbar\omega$, propagating along the metal surface.

The imaginary part of k_x, k_x'', is responsible for lossy propagation of the SPP along the interface, with a characteristic propagation length

$$\delta_{SPP} = \frac{1}{2k_x''} = \frac{1}{k_0}\left(\frac{\varepsilon_1^{'} + \varepsilon_2}{\varepsilon_1^{'}\varepsilon_2}\right)^{\frac{3}{2}}\frac{\left(\varepsilon_2^{'}\right)^2}{\varepsilon_2^{''}}, \tag{II.10}$$

and lifetime τ_{SPP}

$$\tau_{\mathrm{SPP}} = \frac{\delta_{SP}}{v_g} = \frac{2\pi}{\omega''} = \frac{1}{ck_x'}\frac{4\pi\left(\varepsilon_2'\right)^2}{\varepsilon_2''}\frac{\varepsilon_1 + \varepsilon_2'}{\varepsilon_1\varepsilon_2'}. \tag{II.11}$$

As mentioned, this results from the non-zero imaginary component of the metal permittivity. Apart from choosing a metal with a high plasmonic resonance (i.e. $(\varepsilon_2')^2/\varepsilon_2''$) there seems to be no other method to increase the SPP propagation length in the metal-dielectric configuration. The plasmonic resonance, as a

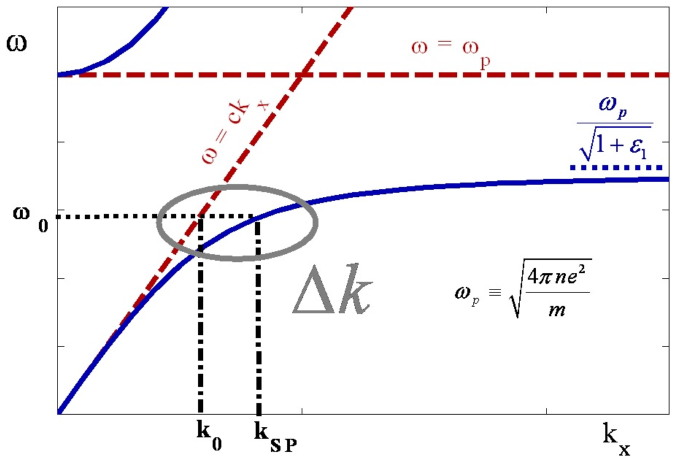

Figure II.2: Basic dispersion for SPPs on smooth metal interface. The bound SPP modes always low below the light line for a given frequency- that is, there is a momentum mismatch necessary to overcome to couple propagating photons to the SPP modes. In the large wavevector, asymptotic limit, the SPP approaches the reduced plasma frequency for the particular metal-dielectric pair.

figure of merit, is shown in Fig. II.3. The black box is the most thoroughly studied regime, while the yellow is the near-infrared portion of the electromagnetic spectrum employed in this work.

II.B Gain assisted propagation

Next, the propagation of a surface plasmon polariton across a metal-gain medium boundary is considered. It is shown that the presence of the gain medium can compensate for the absorption losses in the metal. The conditions for existence of an SPP and its lossless propagation are derived analytically for a single infinite metal-gain boundary. In addition, the cases of thin slab and stripe geometries are also investigated using finite element simulations. The calculated gain requirements suggest that lossless gain-assisted SPP propagation is achievable in practice.

The ability to guide optical fields through a prescribed route is critically

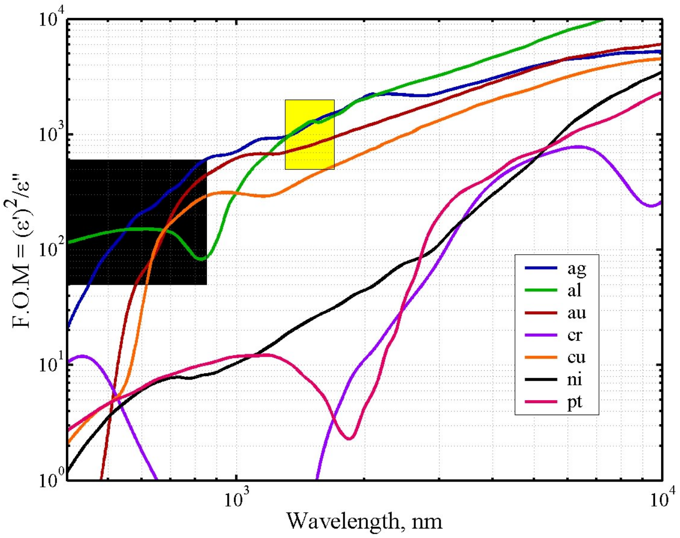

Figure II.3: Figure of merit of SPP oscillations for a given material. In the visible regime, silver is the most the most commonly employed metal. In the near- and mid-IR, gold, aluminum, and copper also become viable materials. Other common metals, particularly chromium often employed as an adhesion layer for gold, have particularly poor material properties for SPP oscillations.

important for realization of compact integrated optical devices and circuits. Traditionally, waveguides have been implemented through local modulation of the shape and/or refractive index profile of the optical dielectric medium, examples of such waveguides being step index, graded index, buried, ridge and rib architectures, which have been extensively investigated in the past three decades [22], [23]. A more exotic approach to guiding optical fields SPPs. These waves propagate along the interface between two media possessing permittivities with opposing signs. They can potentially be used to channel and concentrate light in dimensions much lower than the conventional diffraction limit [2], leading to dense integration of optical circuits. However, in practice a medium with negative permittivity is realized using a metal near the plasma frequency where the negative real component of the complex permittivity, ε', is accompanied by an energy dissipating imaginary part ε'', which results in lossy propagation of SPPs. Consequently, this energy dissipation limits the effective propagation length of SPPs to values in the micrometer to millimeter range, thereby creating an obvious obstacle in utilizing them in practical optical devices and circuits.

As a possible solution to this fundamental problem, we study the propagation of SPPs on metal waveguides in the presence of an optical gain medium. The influence of a gain medium on SPP propagation has previously received some attention. Plotz et. al. [24] have considered gain-enhanced total internal reflection (TIR) [25] in the presence of a metal film, where the gain medium enhances the free space TIR wave through the mediation of excited SPPs on the metal surface. The paper shows that above a certain threshold, a reflection singularity exists for any metal thickness. The authors also estimate the amount of gain required in the case of a silver metal film, which was found to surpass what was available in dye based gain media at that time. Sudarkin and Demkovich [26] continue this work by studying the propagation of SEWs on the boundary of a metal and a gain medium for transversally bounded and unbounded excitation laser beams. They also mention the possibility of creating a surface plasmon based laser.

In this section we will expand upon these concepts from a guided wave standpoint, by investigating gain-assisted propagation of SPPs on planar metal waveguides for different waveguide geometries. Instead of using Fresnel reflection coefficients for the analysis, as in [25] and citeSudarkin89, we will directly work with propagation constants and Poynting vectors, as these are better suited for treating wave propagation on the surface of planar slabs and stripes. Also, the Poynting vector approach will enable us to investigate the wavefront behavior when the gain is varied.

The analysis is carried out using classical electromagnetic wave theory for the case of an infinite metal-gain medium boundary, and later supported by finite element simulations of SPP propagation in thin slab and stripe waveguide configurations. Finally, we assess the practicality of implementation and experimental testing of our theoretical predictions.

II.B.1 Analytic solutions to gain assisted propagation at single planar interface

Replacing the passive dielectric medium in region 1 by a dielectric medium with gain will enable us to compensate for the losses in the metal, as evidenced by the calculations described below. We start by assigning to region 1 a gain medium with complex permittivity $\varepsilon_1 = \varepsilon_1' + i\varepsilon_1''$ (with negative ε_1'' representing gain) and investigating the conditions for a bound wave to propagate at the interface. At this point our only assumption is that ε_2' is negative and its absolute value is much larger than the other three permittivity components. The equations governing the SPP propagation for this material configuration are:

$$\begin{cases} k_x^2 = k_0^2 \frac{(\varepsilon_1'+i\varepsilon_1'')(\varepsilon_2'+i\varepsilon_2'')}{(\varepsilon_1'+\varepsilon_2')+i(\varepsilon_1''+\varepsilon_2'')} & (a) \\ \\ k_{z_i}^2 = k_0^2 \frac{(\varepsilon_j'+i\varepsilon_j')^2}{(\varepsilon_1'+\varepsilon_2')+i(\varepsilon_1''+\varepsilon_2'')} & (b) \end{cases} \tag{II.12}$$

First, we find the limits on ε_1'' which will result a bound solution (i.e. $\Im(k_{z_j} > 0)$). From Eq. II.12(b) we have:

$$\begin{aligned} k_{z_1} &= k_0 \frac{(\varepsilon_1'+i\varepsilon_1'')\sqrt{(\varepsilon_1'+\varepsilon_2')-i(\varepsilon_1''+\varepsilon_2'')}}{\sqrt{(\varepsilon_1'+\varepsilon_2')^2+(\varepsilon_1''+\varepsilon_2'')^2}} \\ \\ &= k_0 \sqrt{\frac{|\varepsilon_1'+\varepsilon_2'|}{(\varepsilon_1'+\varepsilon_2')^2+(\varepsilon_1''+\varepsilon_2'')^2}}(-\varepsilon_1''+i\varepsilon_1')\sqrt{1-i\frac{(\varepsilon_1''+\varepsilon_2'')}{(\varepsilon_1'+\varepsilon_2')}} \\ \\ &\simeq k_0 \sqrt{\frac{|\varepsilon_1'+\varepsilon_2'|}{(\varepsilon_1'+\varepsilon_2')^2+(\varepsilon_1''+\varepsilon_2'')^2}}(-\varepsilon_1''+i\varepsilon_1')(1-i\frac{(\varepsilon_1''+\varepsilon_2'')}{2(\varepsilon_1'+\varepsilon_2')}) \end{aligned} \tag{II.13}$$

From Eq. II.13 and the condition $\Im(k_{z_j} > 0)$, we have:

$$(\varepsilon_1'')^2 + \varepsilon_2''\varepsilon_1'' + 2\varepsilon_1'(\varepsilon_1' + \varepsilon_2') < 0 \tag{II.14}$$

which is satisfied if:

$$\frac{-\varepsilon_2'' - \sqrt{(\varepsilon_2'')^2 - 8\varepsilon_1'(\varepsilon_1' + \varepsilon_2')}}{2} < \varepsilon_1'' < \frac{-\varepsilon_2'' + \sqrt{(\varepsilon_2'')^2 - 8\varepsilon_1'(\varepsilon_1' + \varepsilon_2')}}{2} \tag{II.15}$$

The aforementioned conditions on ε_2' guarantee that these bounds are real and have opposite signs. This places a limit on the allowable amount of absorption or gain in the dielectric for bound waves to exist. The longitudinal propagation characteristics of the SPP are given by k_x in Eq. II.12, which simplifies to:

$$k_x^2 = \frac{k_0^2}{(\varepsilon_1' + \varepsilon_2')^2 + (\varepsilon_1'' + \varepsilon_2'')^2}[\varepsilon_1'((\varepsilon_2')^2 + \frac{|\varepsilon_1|^2}{\varepsilon_1'}\varepsilon_2' + (\varepsilon_2'')^2) + i\varepsilon_2'((\varepsilon_1')^2 + \frac{|\varepsilon_2|^2}{\varepsilon_2'}\varepsilon_1' + (\varepsilon_1')^2)] \tag{II.16}$$

where $|\varepsilon|^2 = (\varepsilon_1')^2 + (\varepsilon_2')^2$ Assuming ε_1',ε_2', and ε_2'' are fixed by the choice of the metal and gain medium, we solve for ε_1'' to find the roots of the imaginary part of Eq. II.16, which has to be zero for lossless propagation of the SPP. This results in:

$$\varepsilon_1'' = \frac{|\varepsilon_2|^2}{2\varepsilon_2''}(-1 \pm \sqrt{1 - \frac{4(\varepsilon_1')^2(\varepsilon_2'')^2}{|\varepsilon_2|^4}}) \simeq \begin{cases} -\frac{|\varepsilon_2|^2}{\varepsilon_2''} + \frac{(\varepsilon_1')^2\varepsilon_2''}{|\varepsilon_2|^2} & (a) \\ \\ -\frac{(\varepsilon_1')^2\varepsilon_2''}{|\varepsilon_2|^2} & (b) \end{cases} \tag{II.17}$$

where the approximation is valid assuming a metal with high plasmonic resonance (i.e. $(\varepsilon_2')^2/\varepsilon_2''$). The sign of ε_1'' is opposite to that of ε_2'', which implies gain in region 1. The magnitude of the solution in Eq. II.17(a) is very large and outside the bounds given in Eq. II.15, so we will only consider Eq. II.17(b). For this solution, the stronger the plasmonic resonance, the less gain is required for lossless propagation. Note also that this result is in approximate agreement with the result derived in [MazRef4], where the TIR reflection is enhanced for $|\varepsilon_1''/\varepsilon_2''|(\varepsilon_1'/\varepsilon_2')^2 > 1$. The reason for the slight difference is that the approximations used in [MazRef4] assume $|\varepsilon_2'| \simeq (\varepsilon_2')^2$, which is correct when $|\varepsilon_2'| \gg \varepsilon_2''$. To relate the value of derived in Eq. II.17(b) to the actual optical power gain, we use the following relation between ε_1'' and γ, the gain coefficient:

$$\gamma = -k_0\frac{\varepsilon_1''}{\sqrt{\varepsilon_1'}} \tag{II.18}$$

which, after substituting from Eq. II.17, gives the gain coefficient required for lossless SPP propagation:

$$\gamma_0 = \frac{2\pi}{\lambda_0}\frac{\varepsilon_2''(\varepsilon_1')^{\frac{3}{2}}}{\varepsilon_2'}. \tag{II.19}$$

Evidently if the gain coefficient is less than γ_0 the SPP propagation will still be lossy but the propagation length will increase accordingly. If the gain is increased past γ_0, the SPP amplitude (i.e. the amplitude of the fields in Eq. II.3) will increase as the SPP propagates along the interface. In practice, the gain medium will saturate at a specific amplitude level, which will inhibit further increase of the amplitude. An interesting point to note is that if the metal-gain medium interface is placed inside a longitudinal cavity and the gain is high enough to compensate for both cavity and SPP losses, sustained oscillations (i.e. lasing) will occur. The experimental realization of surface plasmon quantum cascade lasers in the middle to far infrared range [27], where surface plasmon losses are relatively small, give support to this prediction. However, the focus in this case is not low loss waveguiding, but rather benefiting from the fabrication advantages of a plasmonic waveguide (compared to a thicker dielectric waveguide in the far infrared) to create a laser cavity. In contrast we provide a rigorous quantitative analysis and a design methodology for the effect of a gain medium on SPP propagation, which, for high enough gain, can lead to the aforesaid lasing situation.

It is also interesting to explore the effect of gain on the wavefront tilt. Under zero gain conditions, the wavefront is tilted towards the interface as a result of the absorptive character of the metal. For our material system the wavefront tilt will be affected by the presence of gain, which we demonstrate by calculating the Poynting vector in region 1 using Eqs. II.3 and II.4:

$$\mathbf{P} = \frac{1}{2}\Re(\mathbf{E_1} \times \mathbf{H}^*) = \frac{|H_y|^2}{2\omega}[\Re(\frac{k_x}{\varepsilon_1})\hat{\mathbf{x}} + \Re(\frac{k_{z_1}}{\varepsilon_1})\hat{\mathbf{z}}] \tag{II.20}$$

Obviously, the tilt direction depends on the sign of $\Re(k_{z_1})$. From Eq. II.5(b) we have:

$$\Re(\frac{k_{z_1}}{\varepsilon_1}) = \Re(\frac{k_0}{\sqrt{\varepsilon_1' + \varepsilon_2' + i(\varepsilon_1'' + \varepsilon_2'')}}) \simeq \frac{k_0(\varepsilon_1'' + \varepsilon_2'')}{2(|\varepsilon_1' + \varepsilon_2'|)^{\frac{3}{2}}}. \tag{II.21}$$

We observe that the tilt direction changes at the point $\varepsilon_1'' = -\varepsilon_2''$, i.e., as the gain grows larger than this amount, the wavefront tilt increases away from the interface, until at the limit derived in Eq. II.15 the wave is no longer bound to the interface. It should be noted that this amount of gain can not be achieved in practice for the visible/infrared range, such that the wavefront will always be tilted towards the

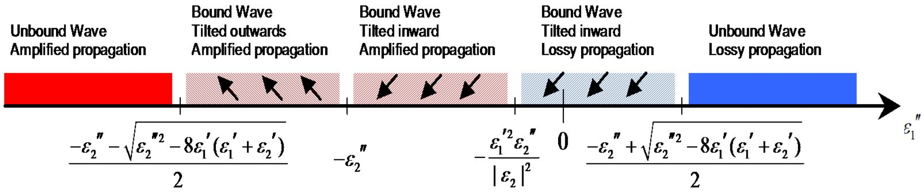

Figure II.4: Schematic illustration of various SPP propagation regimes as a function of ε_1''

metal surface. Fig. II.4 shows the different operating regions of the SPP versus ε_1''.

To justify the practical validity of a planar integration scheme based on gain-assisted SPPs we next use realistic material properties to verify that the gain limit indicated in Eq. II.19 is attainable in practice. For our simulations and calculations we will consider the propagation of an SPP excited by a 1550 nm light source propagating on a silver surface ($\varepsilon_2 = -116.38 + i11.1@1550$ nm) [28]. For the gain medium, we assume ε_1' to be 11.38, which approximates a InGaAsP-based gain medium. From Eqs. II.17(b) and II.19 we find $\varepsilon_1 = -0.106$ and $\gamma_0 = 1275cm^{-1}$ which is within the limits of currently available semiconductor based optical gain media [29][30]. Note that this estimated gain value is an approximate upper limit for lossless SPP propagation on a silver surface at 1550 nm in the assumed configuration, since Eq. II.19 shows that γ_0 decreases with decreasing ε_1' . Hence, we anticipate that using lower refractive index gain media will require lower gain compared to InGaAsP and similar high refractive index media. Examples of such gain media are quantum dots embedded in a glass matrix or polymer [31]. Also, other materials may also offer enough gain to satisfy the requirements of lossless propagation at other wavelengths [32].

Fig. II.5 shows the effect of varying gain on selected parameters of the SPP for the abovementioned material system, namely $\Im(k_x)$, the propagation length, $\Re(k_{z_1}/\varepsilon_1), and\Im(k_{z_1})$. From these, the gain values for lossless propagation, zero wavefront tilt and bound propagation limit are found to be equal to $1264.3cm^{-1}, 13341cm^{-1}and67045cm^{-1}$, respectively.

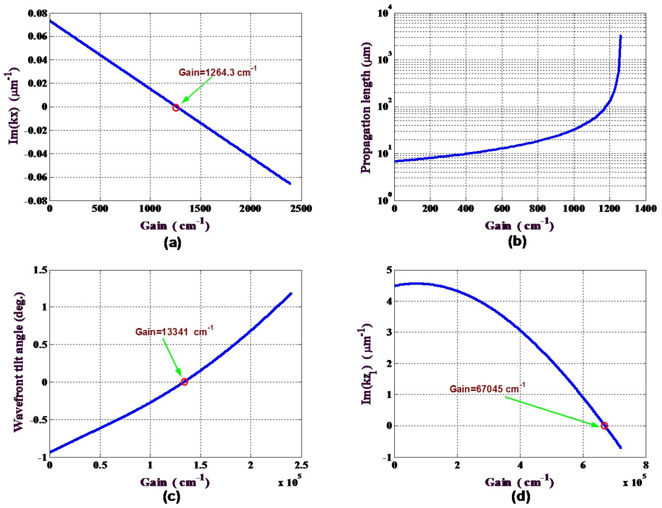

Figure II.5: Plots of: (a) $\Im(k_x)$, (b) propagation length, (c) wavefront tilt angle and (d) $\Im(k_{z_1})$ versus gain. The points corresponding to lossless propagation, zero wavefront tilt and bound surface wave limit, respectively, are also shown.

The slight discrepancies between these numbers and values predicted from Eqs. II.15, and II.19 are due to the first order Taylor approximations used throughout the derivations. Note that the propagation length becomes very sensitive to gain near γ_0, which may be of interest for switching and modulation purposes.

The preceding analysis may of future use for low loss SPP propagation, and experimental investigations are ongoing; however, throughout the rest is this dissertation, all dielectric layers will be assumed to have no optical gain. We now turn to the actual excitation of SPPs by freespace light.

II.C Optical excitation of SPP waves

SPPs may be excited either by free electrons [33] or light [34]. Electrons penetrating a solid transfer momentum $\hbar q$ and the energy ΔE_0 to the electrons of the solid. The physics of surface plasmons has been studied intensively with electrons and the fundamental properties of SPPs have been found in good agreement with the theoretical concepts [33]. However, due to a number of reasons, it is generally not convenient reach the regions of small k_x, and further the use of accelerated electrons in a vacuum environment severely hinder a number of studies one would like to perform.

In this work, we are exclusively interested in excitation of SPPs by photons (small in-plane wavevector regime). This process is complicated by the dispersion relation, requiring larger wave vector for the SPPs than for the photons exciting them. At a given photon energy $\hbar\omega$ the wave vector $k_0 = \omega/c$ has to be increased by some value in order to convert the photons into SPPs. Two methods are usually used to increase the wave vector of the free-space photons: grating coupling [35] and total internal reflection coupling [36, 37]. There are several variations on these two basic themes, and we show several of the most commonly employed methods of coupling to SPP waves in Fig. II.6. These include evanescent field coupling methods- via a prism in the Kretschmann-Raether and Otto configurations and with a nearfield scanning optical microscope (NSOM) tip (essentially a tapered optical fiber). Grating coupling may be accomplished via either periodically patterned surface structures or often simply random surface roughness.

When the light is reflected at the metal-dielectric boundary with a dielectric medium $\epsilon_3 > 1$ the projection of the wave vector on the surface is $k_x = \sqrt{\epsilon_3} k_0 \sin\theta_0$, where θ_0 is the incidence angle, and the dielectric constants $\epsilon_{1,2,3}$ for the substrate, metal layer, and superstrate, respectively. While this momentum is insufficient to excite SPPs on the metal-dielectric interface, if the metallic film is thin enough, electromagnetic field can couple into the surface mode on the second metal interface and excite the SPP at some incidence angle θ_0:

$$k_x = k_0\sqrt{\epsilon_3}\sin\theta_0 = k_0\left(\frac{\epsilon_1\epsilon_2}{\epsilon_1+\epsilon_2}\right)^{\frac{1}{2}} = k_{spp}. \tag{II.22}$$

This type of SPP excitation can be realized with nearly 100% efficiency (for a specific metal film thickness depending on the dielectric constant and wavelength of illumination) using prism coupling configurations, first demonstrated by Kretschmann [36] and Otto [37].

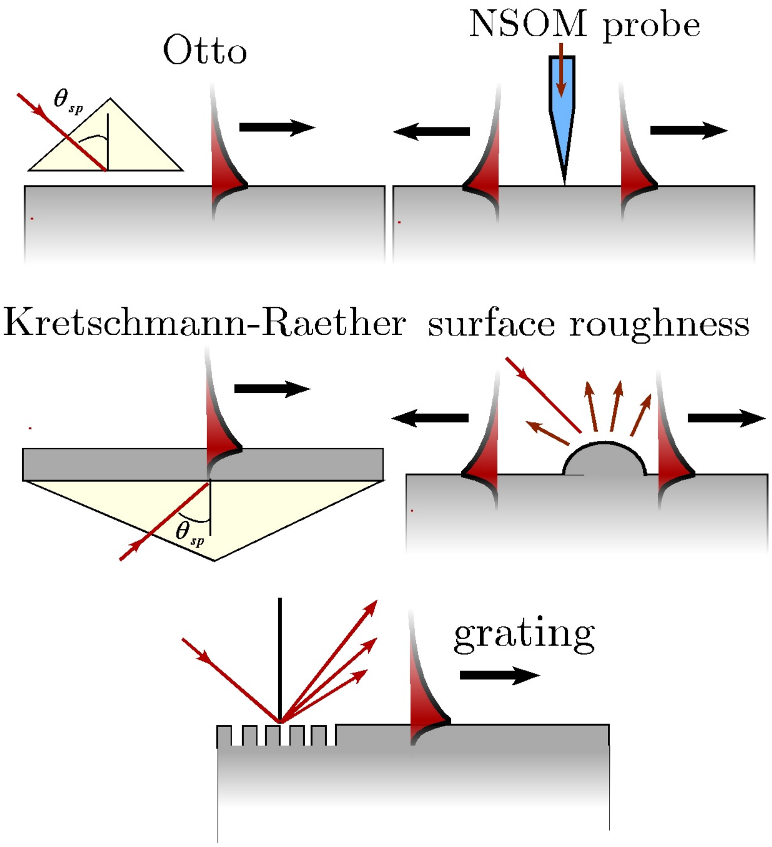

Figure II.6: Most commonly employed methods for coupling to SPP modes.

When light hits a diffraction grating with period Λ, wave vector of the diffracted waves on the surface is described by

$$k_x = k_0 \sin\theta_0 \pm mK^G. \tag{II.23}$$

Integer number of the grating effective wave vectors $K^G = 2\pi/\Lambda$ are added or subtracted from the projection of the incident optical field wave vector $k_0 \sin\theta_0$ on the grating, according to the diffraction order m. Under appropriate conditions the surface wave vector k_x can satisfy the SPP dispersion relation II.7 for the incidence angle θ_0 and convert the incident optical field to SPP

$$\sin\theta_0 = k_0 \left(\frac{\epsilon_1\epsilon_2}{\epsilon_1+\epsilon_2}\right)^{\frac{1}{2}}, \tag{II.24}$$

where λ_0 is the wavelength of the incident light, and in this case we refer only to a single interfacial system with two dielectric constants ϵ_1 and ϵ_2 of the dielectric and metal region, respectively.

In Fig. II.7 we sketch these two basic mechanisms, evanescent coupling as described by Eq. II.22 and Eq. II.24, as well as grating coupling by Eq. II.24.

In the majority of cases, SPPs in optical excitation experiments is observed as attenuation of the optical beam, reflected either from the diffraction grating or the dielectric interface at some incidence angle, satisfying the SPP excitation condition Eq. II.22 or Eq. II.24. The difference between the incident and reflected optical power is associated with the power transferred into the SPP. While this information may be extraordinarily useful, and is precisely the basis of a number of highly successful SPP based sensor devices (discussed a length in Chapter VII), there are a number of limitations. One of these is that the experimenter is typically inferring information about a confined SPP mode from these far-field spectral measurements. We attempt to address this particular limitation of not “seeing” light from the actual mode with the use of the imaging techniques discussed in Chapter V.

The excitation of SPPs on nanohole array gratings is similar to the process described in Eq. II.24, however there are two grating vectors which are available

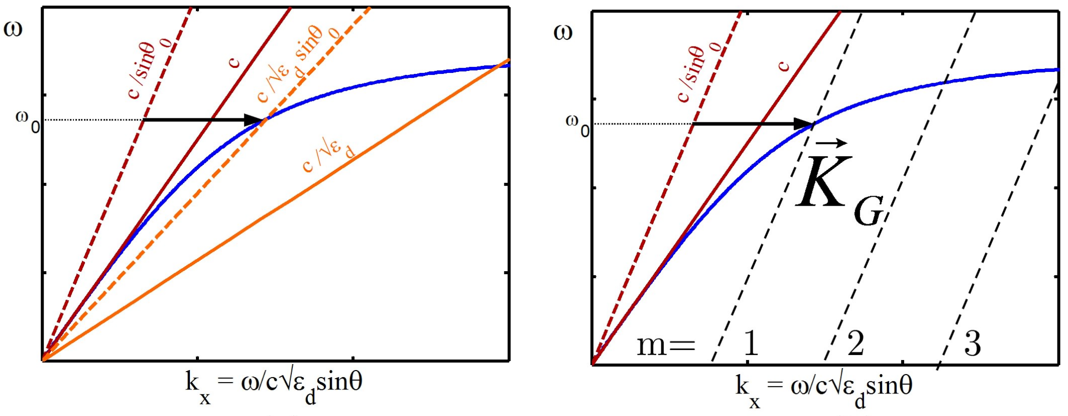

(a) (b)

Figure II.7: Dispersion diagrams for coupling to SPP modes. (a) Evanscent field coupling (Otto, Kretschmann-Raether, NSOM): photons incident from a high refractive index media is used to couple to SPP modes at a lower refractive index dielectric-metal interface. (b) Grating coupling: momentum from a periodic grating (or random roughness) is added to match the incident photon to the SPP mode.

to couple into a particular order. We return to this two-dimensional coupling in Chapter IV after first describing the nanohole array fabrication methods in the next chapter (III).

The text of Chapter Two in part is a reprint of the material as it appears in the following publication:

- M. Nezhad, K. Tetz, and Y. Fainman, “Gain assisted propagation of surface plasmon polaritons on planar metallic waveguides”, *Optics Express* **12**, 4072 (2004).

The dissertation author was the primary researcher and author. The coauthors listed in these publications directed and supervised the research which forms the basis for this chapter.

III

Metallic micro- and nanostructure fabrication

One of the most pressing challenges in developing nanoscale optical devices is the fabrication. One would often like to create some geometric structure much smaller than the wavelength of light in use. However, this becomes complicated when independent feature scales are desired for each dimension and the aspect ratio becomes large. In this work we are interested in making nanoscopic holes in optically thick metal films. This is particularly challenging to do with very small hole diameters in relatively thick metal films with most conventional techniques.

In this chapter we discuss the fabrication of such structures used throughout the rest of this work. Examples of two such systems are shown in Fig. III.8. In Fig. III.8(a) we show show an array of holes a gold film on a glass substrate. This type of structure is made with a holographic lithography technique that facilitates fabrication of such structures on a large scale. In Fig. III.8(b) we show an array of holes in an aluminum film that is patterned with e-beam lithography. While there are certain limitations with the e-beam lithography process, it is well established and flexible for creating a wide variety of nanoscale structures.

While structure fabrication is relatively straight-forward and not the pri-

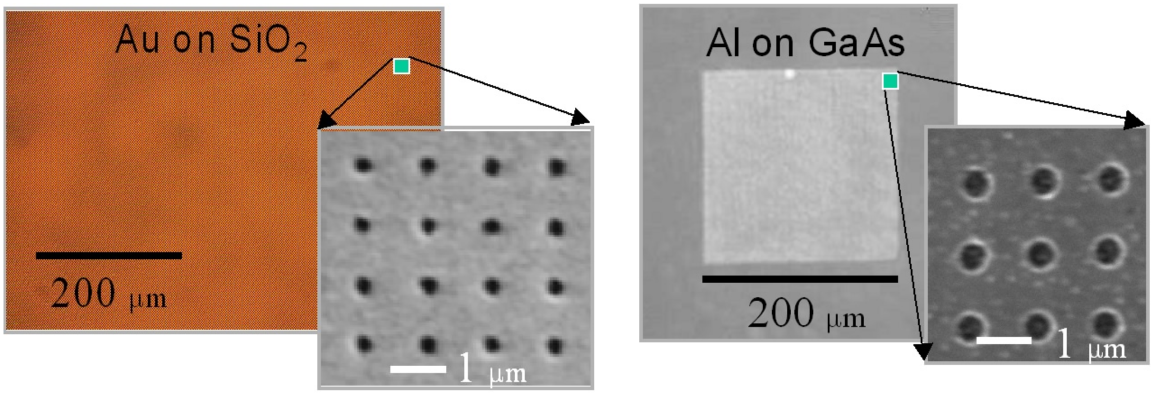

(a) (b)

Figure III.1: Optical images of nanohole arrays fabricated by both holographic lithography (a) and direct e-beam writing (b). Inset to each is a representative SEM image of a typical array.

mary focus of this work, we nonetheless briefly present the basic fabrication procedures here for future reference. We begin by discussing the metal deposition methods[1]. Next we look at the two different lithography methods utilized, with particular emphasis on interferometric lithography as a significant amount of effort was devoted to development instrumentation for facilitating this method during the course of this work. Finally we briefly overview the various etching processes utilized to obtain the desired structures.

We also note that there are a number of authors [38, 39] who have done parametric studies of the various geometric parameters in this same system in recent years (both experimental and numerical), and thus this is not the primary concern for ourselves in this work- though we do note the primary trends that affect our results. In most of this initial experimental work, researches employed a focused ion beam (FIB) to create the nanohole arrays. With this method it is possible to make very high aspect ratio nanoholes in a serial fashion- though the field size is typically limited to only a few tens of microns and optical characterization becomes

---

[1] While it is often common to use liftoff techniques when patterning various metallization layers, we forgo this method primarily because of: (1) the difficulty in attaining a reasonably large aspect ratio, as mentioned, at these feature sizes (2) in the case of e-beam, the relatively large difference in exposure times in writing small spots directly rather than the inverse pattern.

somewhat more challenging.

III.A Substrates and metal deposition

We have used both semiconductor and insulator materials as substrates for nanohole structures fabrication. The semiconductor substrates were nominally undoped (pSilicon (100), double polished (i.e. both the front and back surfaces of the wafers substrates, and nominally undoped GaAs (100). These substrates are simply cleaned with consecutive rinses in acetone, methanol, and running DI water for 2 minutes each prior to loading in a particular evaporator. Fused quartz, double polished, optically flat substrates were also prepared in a similar manner. In initial experiments, conventional microscope slides were used. In this case, a piranha etch of H_2SO_4:H_2O_2, 3:1 at 120° for approximately 10 min was utilized to remove any organic contaminants.

Aluminum was deposited via thermal evaporation (Edwards E306A Thermal Evaporator), while titanium, chromium, and gold layers were both thermally evaporated, as well as sputtered (Denton Discovery 18 Sputtering System). The sputtering system had an advantage of allowing large area samples, and different substrates to be deposited simultaneously because of the large chamber volume and extensive sample mounting area.

When depositing gold, a thin ($\sim$2-10 nm) nickel, chromium, or titanium adhesion layer was first deposited. As illustrated in Fig. II.3, each of these metals has a very poor plasmonic resonance. Inclusion of this adhesion layer affects the SPP modes at this interface (stronger damping, in particular), modifying those that would otherwise exist at the glass-gold interface [40][41]; we will therefore refer, instead, to a glass-metal (GM) interface. With the inclusion of a very thin layer ($\sim$2 nm), as we will see, SPP oscillations are present to a significant degree on this interface. By using a thicker layer ($\sim$ 10 nm or more), the SPP modes are significantly damped and their presence is not readily observable in the measurements we describe in later chapters.

III.B Lithography: electron beam direct write

For the cases where we utilize e-beam direct write paterning, we choose PMMA as the e-beam resist for our samples since it provides a very high resolution and is a common choice for patterning nanostructures. The standard e-beam lithography process is as follows: an e-beam resist is spin-coated on the substrate, followed by pre-bake to remove the solvent within the resist. The sample is then exposed under a scanning electron beam, followed by a standard development process. A post-bake procedure may be applied to enhance the etch resistance of the resist, but in most cases we used this as a mask for a chemical etchant and this step is unnecessary. In our experiments we use 950k PMMA (950 A4 from MicroChem) as our e-beam resist. We use a typical spin speed of 4000 rpm for 40 s to reach a thickness of $\sim$ 200 nm. The pre-bake and post-bake conditions are both normally set to 170 C for 90 min in an oven. For e-beam exposure we use a converted scanning electron microscope (SEM) [6] with Nanometer Pattern Generation System (NPGS, from JC Nabity Lithography Systems). To achieve the best resolution, the maximal electron acceleration voltage (35 kV) is used, and the optimal dosage is found to be between $\sim 200 - 300\ \mu\text{C/cm}^2$.

The converted SEM that we use for e-beam lithography can only provide a limited exposure area. For the resolution of around 100 nm, the maximum field of view (and therefore exposure area) is approximately $200 \times 200\ \mu$m, which is the field size that we typically utilize. Devices that require larger areas with the same linewidth will need to be patterned either with an e-beam writing system with stitching capability or with multiple patterning techniques.

Commercial e-beam writers are designed for large area patterning. This is usually achieved by precisely stitching multiple exposure areas together using positioning translation stages with laser interferometric precision. However, the major drawback is the extensive writing time and therefore poor throughput of this process. Moreover, commercial e-beam writers are very expensive, with a typical cost of around several million dollars. Since high precision stitching capability is unavailable in our facility, alternative approaches need to be exploited.

As we have mentioned earlier, many of our devices require not only small feature sizes, but also deep profiles. E-beam resist usually does not provide enough etch resistance to serve as a dry-etching mask for high-aspect-ratio structures. For the structures patterned in PMMA we used carefully controlled wet chemically etching to achieve reasonable geometric features for characterization.

While the method is extremely flexible, with exquisite control of feature dimensions, the serial nature of the exposure makes it cumbersome for some studies. We next explore the use of holographic techniques for lithography.

III.C Lithography: multi-beam holographic exposures

While many of the salient features of these nanohole arrays may be measured and with arrays produced via e-beam lithography as described above, the ability to produce large, uniform samples greatly simplifies the optical characterization of such structures (the optical transmittance can often be quite low, therefore interrogation over larger areas is preferable). An alternative method that has been investigated in our lab is to use a holographic photolithography system to pattern nanoscale structures.

Optical interference has long been a powerful and proven tool useful in many areas of optics, precision measurement, and information processing/storage. A relatively new holographic technique has proven successful at forming two-dimensional (2-D) surface relief patterns and three-dimensional (3-D) volumetric structures in photosensitive materials, using the superposition of three or more coherent laser beams. Sometimes called optical interference lithography or holographic lithography, it is a particularly compelling experimental route toward photonic crystals and diffractive structures in general since it is possible to fabricate all five 2-D and all fourteen 3-D Bravais lattices and control the shape of the unit cell with relative ease.

The approach is based on the exposure of a photoresist to the interference of two ultra violet (UV) laser beams, creating gratings with a submicron period. This method is very cost effective and time efficient, but produces only periodic structures; therefore, it is limited to specific application areas.

A number of authors are using holographic techniques, but most resists are thin and soft, and therefore limit their applicability to use as a mask for transfer of the pattern to metallic films. Indeed, most structures fabricated with this method, holographic interference lithography and dry etching, have only been but only etching 35 nm of gold film (e.g. Ref. [42]). Also it is rather difficult, if not impossible, to control the fill factor to get very narrow holes with holographic lithography- even when utilizing the nonlinear exposure properties of the resist to their fullest.

In this work we utilize a specific case of interference lithography- fabrication of two-dimensional periodic structures by multi-exposure of two-beam interference technique [43]- that is the most straight forward to implement experimentally, while we add a number of controllable, adjustable parameters to make the setup flexible and easily reconfigurable.

III.C.1 Basic theory

In the most common situation, a the planar substrate is coated with a photosensitive prepolymer and then exposed to the optical interference pattern. As with standard lithographic procedures, a photochemical reaction leads to sharp boundaries between regions of high and low crosslinking corresponding to the regions high and low intensity. Subsequent development of the resist leaves only the highly crosslinked areas, and several process parameters influence the result critically, especially total exposure time/intensity and development time. This 2-D or 3-D polymer lattice layer itself may be used as the optical element, used as the patterned photoresist for wet chemical or reactive ion etching of the substrate, or may alternatively be impregnated with other materials .

As with conventional holography, interference patterns resulting from more than two laser beams depend on both the propagation and polarization parameters of each beam, and must therefore be chosen such that the desired optical lattice is created. We start with the most general expression of the intensity profile $I(\mathbf{r})$ formed by N coherent plane waves, based on arbitrary irradiance, propagation, polarization, and phase of each beam.

The electric field vector of the mth wave with complex amplitude can be written [44]

$$\mathbf{E}_m(\mathbf{r}) = E_m \exp(i\mathbf{K}_m \cdot \mathbf{r} + i\delta_m)\mathbf{e}_m, \tag{III.1}$$

where E_m is the real amplitude, $\mathbf{r} = (x, y, z)^T$ is the position vector, $\mathbf{K}_m$ is the propagation vector, $\mathbf{e}_m$ is the polarization vector, and δ_m is the absolute phase.

For the case of multiple beams, the intensity defined as the vector product of the total electric field $\mathbf{E}_{tot} = \mathbf{E}_1 + \mathbf{E}_2 + \mathbf{E}_N$ with itself. This intensity profile can be expressed in as the sum of vector products:

$$I(\mathbf{r}) = \mathbf{E}^*_{tot} \cdot \mathbf{E}_{tot} = \Re\left(\sum_{l,m=1}^{N} \mathbf{E}^*_l \cdot \mathbf{E}_m \exp[i(\mathbf{K}_l - \mathbf{K}_m) \cdot \mathbf{r} + i(\delta_l - \delta_m)]\right) \tag{III.2}$$

While this general interference pattern facilitates a wide variety of lattice formations (the entire set of 3-D Bravais lattices is accessible with $N = 4$ beams), in this work we have utilized an experimental setup which incorporates only $N = 2$ beams. In this specific case, each exposure yields a 1-D sinusoidal intensity pattern where the period Λ is given by the expression:

$$\Lambda = \frac{\lambda}{2\sin\theta}, \tag{III.3}$$

where λ is the wavelength of the illumination, and θ is half the angle between the two interfering beams, as illustrated in Fig. III.2.

When using such a configuration to create an interference pattern in a recording medium, it is also important to note the effects of the medium index on the interference pattern. One of the consequences of Snell's law ($n_{air} \sin \theta_{air} = n_{film} \sin \theta_{film}$), when coupling from air into a film is that the lattice constants Λ for all of the 2-D lattices are independent of the recording index- and we can therefore consider the freespace wavelength and interference period when considering the system design and setup.

While it is possible to use any photosensitive polymer in the recording process, in this work have used the chemically amplified negative resist SU-8 2000 (Micro Chem). Because it is a negative resist, areas that are exposed to higher intensity illumination are preferentially crosslinked and remain after the development process. While most resists exhibit somewhat of a nonlinear exposure threshold, this one also requires a post exposure baking (PEB) step at $\sim 90 - 125$ C to facilitate crosslinking. During this process, it is possible to adjust the fill factor of the remaining resist and thus achieve small hole diameters. This is in contrast to many other photopolymers where it would be extremely difficult to achieve the relatively small hole diameters because of the sinusoidal intensity distributions of the exposure intensity distributions.

Instead of having a larger number of simultaneously interfering beams, we alternately utilize a sequence of exposures of two interfering beams. Each interference exposure (from a few seconds to approximately a minute in duration) is then added incoherently to give the total dose D given by

$$D = \sum_{i=1}^{N} \Delta t_i I(\mathbf{r}), \tag{III.4}$$

where Δt is the exposure time and N is now the number of exposures (we refer to only two interfering beams from this point forward). The resultant intensity profiles, and the approximate polymer morphology after thresholding the intensity profiles, are shown in Fig. III.2. The first exposure is made at an arbitrary angle ϕ_1 for a fixed time Δt_1, and then the sample is rotated 90°, and a second exposure

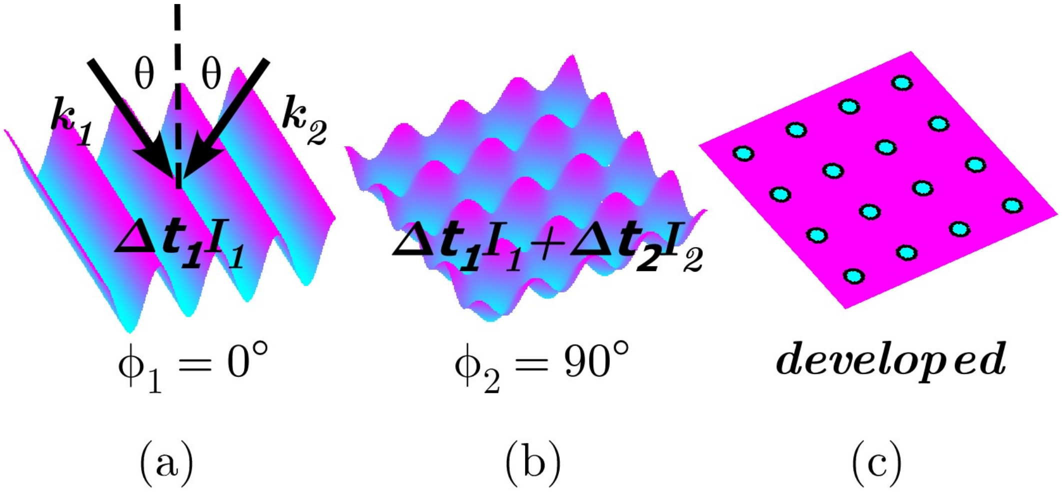

Figure III.2: (a) Sinusoidal interference pattern between two beams (b) 2-D sinusoidal intensity distribution after a second exposure. (c) Approximate polymer morphology after thresholding the intensity profiles.

is made for Δt_2. After developing of the Su-8 resist, the remaining crosslinked polymer has a profile somewhat similar to that illustrated in Fig. III.2(c).

This process of multiple exposures may easily be extended to any number exposures. Intensity distributions for a number of different exposures, N, are shown in Fig. III.3. In this figure we show the intensity distributions and approximate, thresholded resist profile for

III.C.2 Holographic lithography experimental apparatus

To aid in rapid, reconfigurable fabrication of large area gratings and nanohole arrays, we have made a number of contributions in developing a high precision, automated, two-beam interference, multiple exposure holographic lithography setup. While there there are certain limitations as to the type of structures that can be fabricated, there the technique and apparatus are nonetheless quite convenient for research purposes, and facilitates relatively easy fabrication of a number of interesting structures.

The optical setup for the interferometric lithography exposure is shown in Fig. III.4. Light from an argon ion laser (364 nm, $\sim$ 30 mW maximum) is first

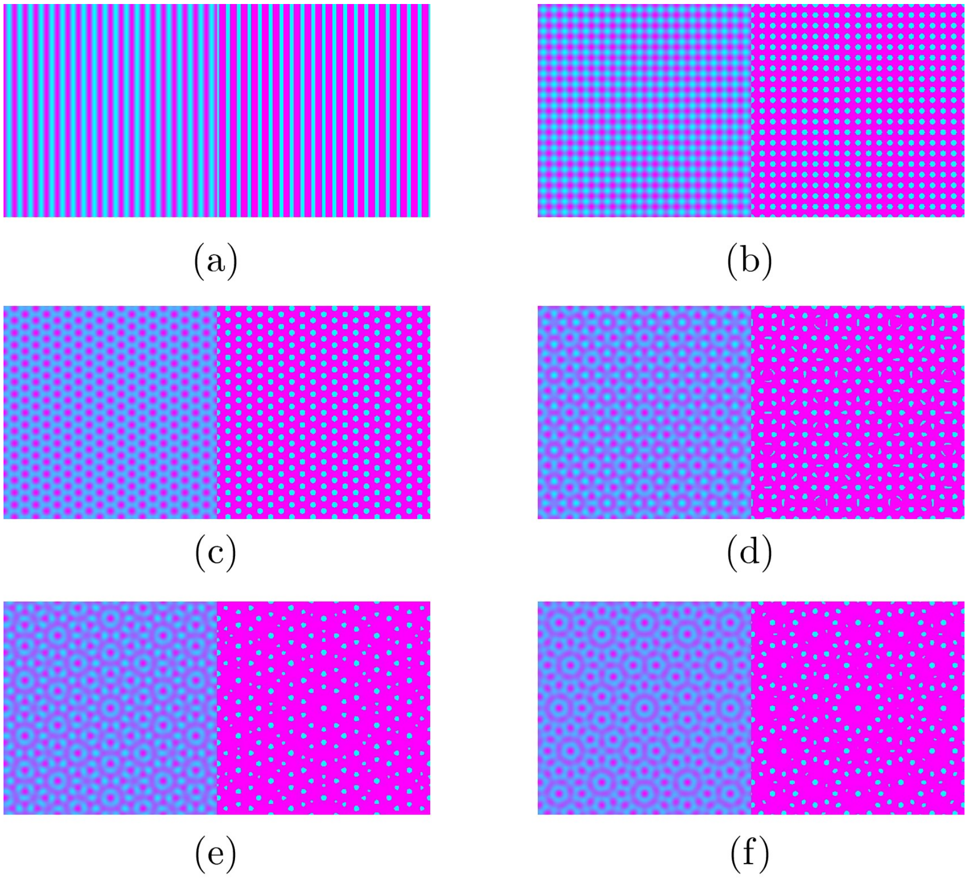

(a) (b) (c) (d) (e) (f)

Figure III.3: Multiple beam holographic lithography intensity distributions. Intensity distribution are shown for N beams equally spaced around the azimuth. $N = 1$ through 6 are shown in (a)-(f), respectively. The nominal intensity distribution is shown on the left in false color, and an example 2-D resist profile is shown on the right assuming a nonlinear threshold of 0.7.

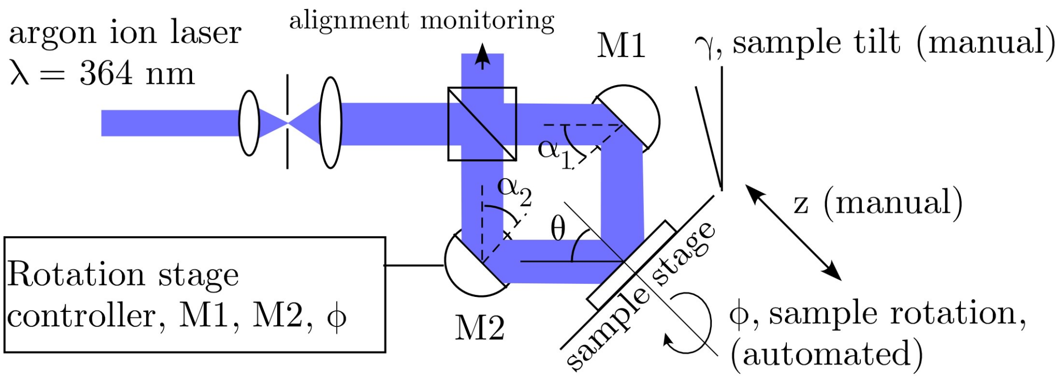

Figure III.4: Multiple exposure dual beam interference lithography setup. An argon laser line is spatially filtered, expanded, split and recombined at the sample plane. The interference angle θ is set by two computer controlled, high precision rotation stages, and a third rotation stage controls the sample azimuthal angle, ϕ.

spatially filtered and expanded. The beam is then split with a nonpolarizing cube beam splitter, and directed towards the sample stage by two mirrors $M1$ and $M2$.

We utilize three high precision, mechanically controlled rotation stages from Physik Instrumente (PI), all controlled with a multi-axis motor controller (model C844). Two of the stages (model M-037.PD) control the mirrors $M1$ and $M2$, and effectively control the period of the interference pattern. The M-037.pd has a design resolution of 8.75 μrad (0.0005°), unidirectional repeatability 30 μrad, and a typical "backlash" error of approximately 200 μrad. The sample stage uses the model M-38.DG rotation stage, design resolution of 0.59 μrad ($3.4 \times 10^{-5\circ}$), unidirectional repeatability 30 μrad, and similar backlash characteristics.

While the quantity of interest is the grating period, given by Eq. III.3, this is controlled through the rotation of the mirrors $M1$ and $M2$. The incidence angle θ, is related to the mirror angle α through the expression

$$\theta = \frac{3\pi}{4} - 2\alpha. \tag{III.5}$$

All three of these rotation stages, as well as a mechanical shutter that blocks the laser beam and opens for the desired duration, are controlled by LABVIEW on a personal computer. For exposures that require more than a single period (if desired), it requires the manual adjustment of the sample stage between exposures.

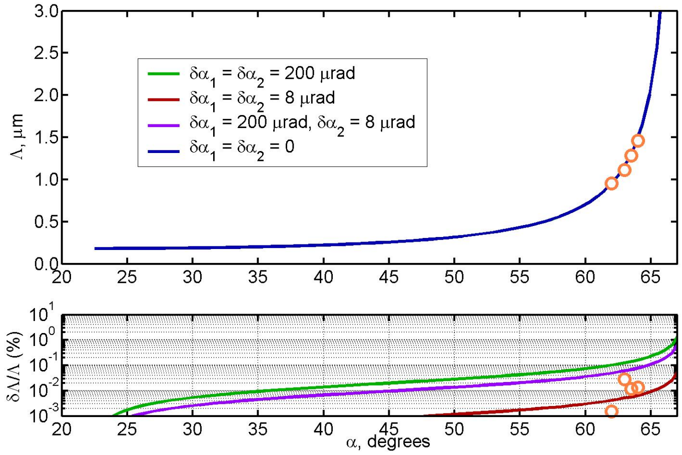

Figure III.5: Holographic lithographic period calibration and error analysis. Four different grating periods, from $1.0 - 1.5 \mu m$ are plotted, along with the measured and expected errors for several different actuator motion positioning errors.

For multiple exposures with different azimuthal angles ϕ, the sample stage is rotated automatically and the sample exposed for the desired duration for each of N exposures.

The initial calibration data is shown in Fig. III.5 (for only a small number of periods that was of initial interest in the current work). The developed photoresist was exposed and the average period measured by SEM. The results are presented along with the expected error due to the mechanical limitations of the rotation stage actuators for the mirrors $M1$ and $M2$- both in the forward direction and what would be expected with a backlash error[2].

It is expected that larger sources of error occur with the manual alignment and collimation of the laser beam. If the beam is not well collimated, the divergence may lead to a chirped grating period across the sample surface. Along with this positioning error, there are a number of other factors involved in the creating of high quality, large area grating structures. Some of these are controlled well, but a number of them lead to deficiencies in the fabricated gratings, these include:

---

[2] If one calibrates the zero position and rotates the actuators in only one direction- as is the standard operating procedure- in principle there is no need to encounter the backlash error for any given exposure position

1. laser drift/stability
2. speckle
3. sample nonuniformity and reflections
4. user error and misalignment
5. spatial intensity distribution

The alignment also critical to minimize larger scale, Moire type interference fringes. When the sample is rotated slightly out of plane due to a tilt in γ, or the sum of angles ϕ does not lead to a rotationally invariant symmetry pattern for higher ($N > 3$) number of exposures, there may exist an extra wavevector mismatch component $\Delta\mathbf{k}$ that is very small leading to larger scale inversions in the intensity distribution. This leads to a complete reversal in the developed resist patterns- making light areas dark and vice versa.

Another constraint in limiting the effective grating area in the system illustrated in Fig. III.4 (which is not an issue with some other configurations). One of the most important is the limitation of the effective aperture of the mirrors M (2 in) and working length z working towards large period interference patterns. While this is not a problem with the grating periods less than $\sim$2 μm, for larger periods one could easily move the sample stage from the position indicated to the alignment monitoring port for very low interference angles θ. In this configuration, both mirrors M reflect their respective beams nearly back at nearly 180°, and large grating periods are easily attainable.

III.C.3 Holographic lithography results

In Fig. III.6 we show SEM images of the results of a typical nanohole array sample (exposed as illustrated in Fig. III.2), and etched into a gold film as described in Sec. III.D. The images in Fig. III.6(a-c) are taken at various places separated by several mm across the grating surface, and illustrates the degree of nonuniformity present on this large scale. Also shown is an approximate calculated resist profile with a nonlinear resist threshold parameter as indicated. The hole diameter varies by more than a factor of two in these representative images, and

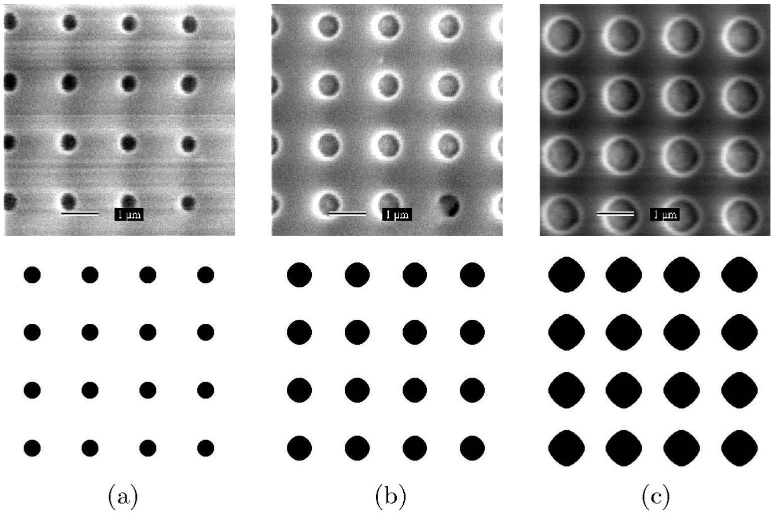

Figure III.6: Variation in fabricated hole diameter across the sample surface. The calculated nonlinear thresholds are (a) 0.1 (b) 0.2 (c)0.35, which are close approximations to the observed hole diameters.

is primarily the result of speckle and the natural gaussian intensity distribution of the illumination beams. This speckle is caused by some imperfections in the spatial filtering element, and was improved significantly at a later date. However, such random intensity distributions made it impossible to quantitatively and systematically study the geometric dependence of the spectral properties of the structures. In all of the work that follows with these holographic gratings, we can only surmise the approximate geometric shapes of the actual area that is measured. In practice, however, it is quite easy to determine the relative hole size over the area of the sample as the optical transmittance varies significantly. By later taking SEM images of the same sample and noting the hole diameter distributions in disparate regions it is possible to relatively accurately estimate the areas that were measured.

The next example, shown in Fig. III.7, is a nanhole array with elliptical holes. Again, we utilize two exposures at at $\phi_1 = 0°$ and $\phi_2 = 90°$ as illustrated in Fig. III.2. This type structure may be easily attained by changing the exposure times between the first and second exposures in the two exposure sequence. In this case we utilized a ratio of $\Delta t_1/\Delta t_2 = 3/2$. The dose is typically calibrated by

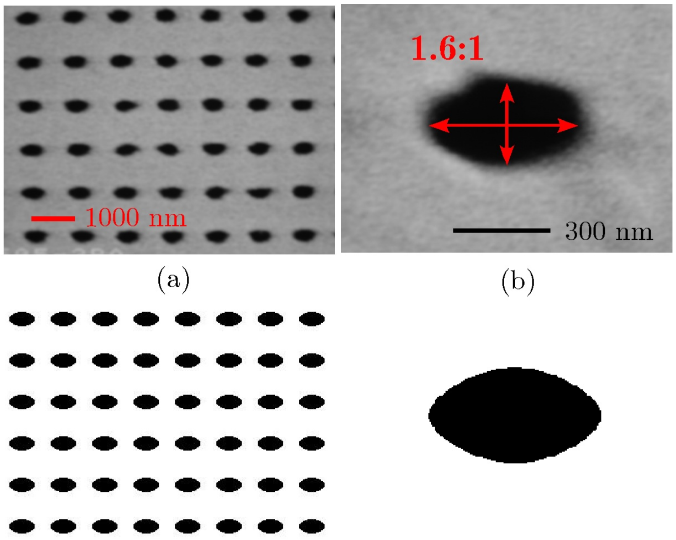

(a) (b)

(c) (d)

Figure III.7: Elliptical nanohole structures. (a) and (b) show SEM images, while (c) and (d) show approximate resist profiles for two unequal exposure times of $\Delta t_1/\Delta t_2 = 3/2$

measuring the power of a single beam, and the exposure time is typically varied for a number of samples from $D \sim 50 - 200 mJ/cm^2$, and the optimal structure selected from the lot.

The resulting structure is then etched into a gold film, and we present the resulting SEM images at two different magnifications in Fig. III.7(a) and Fig. III.7(b). While preliminary characterization, the results are not presented in this work. Several authors have studied similar structures, and, as expected, show that they are anisotropic in the optical response even at normal incidence. This me be of use, for example, in applications such as presented in Chapter VII for an imaging sensor application.

Another very interesting class of structure that may be fabricated with this technique are quasicrystal lattices. This type of crystal structure shows long-range order and has rotational symmetry. However, they lack translational periodicity. Discovered in metal alloys in the early 1980s, such space filling characteristics that have lead to a number of interesting effects in optical devices. In particular,

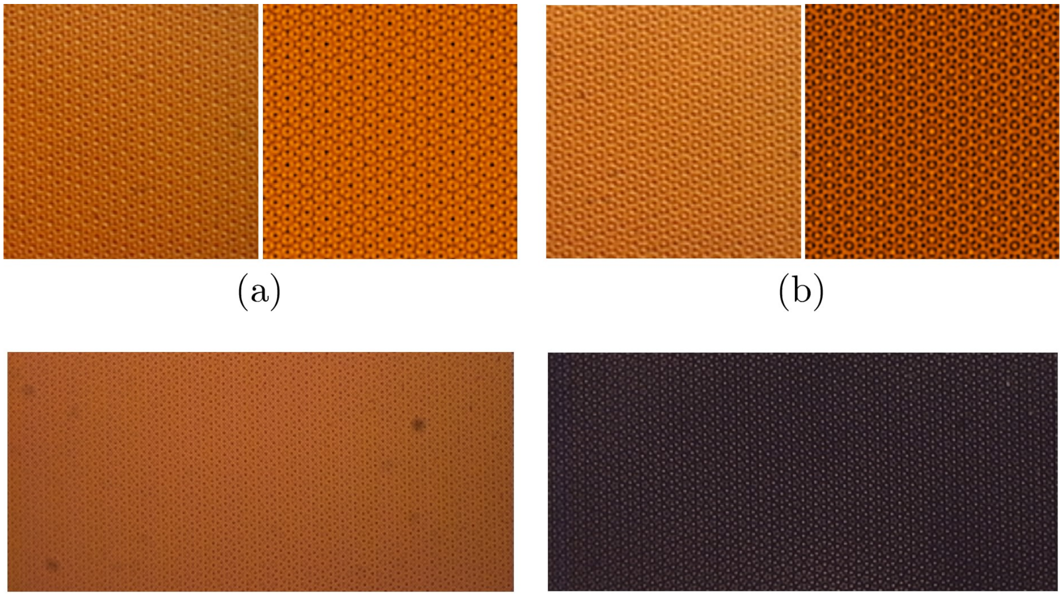

(a) (b)

(c) (d)

Figure III.8: (a) and (b) show optical microscope images (left) and calculated intensity distributions (right) of 2-D quasicrystal lattices. The lattice quasi-period is 1 μm. These images are at two disparate portions of the sample, separated by several hundred microns, that have an inverted intensity profile because of the Moiré type fringing effect as explained in the text. (c) shows another area at a smaller magnification, and (d) is the same sample position under dark field illumination conditions.

in certain configurations they have been shown to exhibit a rather large optical [45, 46, 47, 48, 49, 50, 51], and have also been studied [52]. The penrose structure has been used to create both extended and localized modes in a dielectric quasicrystal lattice [53], and a study of transmission through a similar penrose tiling of subwavelength apertures in a metallic film was also recently reported [54]. The same quasicrystalline structures have also been shown to enhance the light extraction from InGaN/GaN LEDs.

A an example of such a crystal structure is shown in Fig. III.8. This is an optical microscope image of developed SU-8 resist on a gold film. The pattern was created with $N = 5$ exposures as illustrated in Fig. III.3. Because of the misaligment and associated Moiré fringing effect, we clearly see an inversion of the developed resist morphology because of these effects. Fig. III.8(a) and Fig. III.8(b) are from different sample locations. Despite this, there are areas of relatively large scale order as indicated in Fig. III.8(c) (brightfield) and Fig. III.8(d) (darkfield). These results demonstrate the capabilities of the lithography system, and show a promising first step in creating such quasicrystalline structures for use in future studies.

III.D Etching

For initial measurements, and proof of principle experiments with early samples, wet chemical etching techniques were used to etch the various metal films. Aluminum was etched with a concentrated E-3 metal (nitric, sulfuric and hydrochloric acids) solution at room temperature with a rate of ∼30 nm/min. Gold was etched with diluted sodium or potassium iodide solution ∼50 nm/min.

Dry etching of gold film was also utilized to obtain a uniform diameter, minimize hole to hole variations, and to obtain high aspect ratio features that are not obtainable with a wet chemical etchant. While the SU8 was still etched much more readily than the gold film, a relatively thick layer ($h \sim 2$ μm) was a sufficient mask layer to etch up to 200 nm films. Etching proceeded in an ICP-RIE machine at elevated temperature (∼100 C) with Cl/BCl_3 process gases.

III.E Standard Processes

While we have employed nearly all combinations of the previously described deposition, lithography, and etching processes, the vast majority of the results presented in the rest of this manuscript are from one of three processes. The first two consist of e-beam direct write lithography of of the pattern followed by wet etching of either gold or aluminum. The third consists of holographic lithography followed by ICP/RIE etching of gold. While the other parameters of may change (hole size, period, etc.), we will refer to these general processes as:

1. **Sample Type A (STA):** “thin” gold film. 40 nm, e-beam patterned, and wet etched on silica glass
2. **Sample Type B (STB):** “thick” aluminum. ∼100 nm, e-beam patterned, and wet etched on GaAs.
3. **Sample Type C (STC):** “thick” gold. ∼200 nm, e-beam patterned, and wet etched on silica glass.

At this point we begin with the optical interrogation of the transmission spectra of such structures.

IV

Nanohole coupling to SPPs: theory and far-field spectral measurements

In this chapter we investigate the spectral transmission properties of light through nanohole arrays in metallic films. We make use of conventional transmission measurements, where the light that passes through the array is measured in the far zone as a function of numerous variables including the material and structural geometric parameters, illumination angles, and with particular emphasis on the polarization state of both the incident and scattered light with respect to the array periodicity. This is the most common method employed in the investigation of such structures, and as such, it most easily compared to the bulk of the existing literature cited.

Making inferences about these surface modes from far-field spectral measurement, without other evidence, is what caused the initial controversy and confusion in the case of "extraordinary" optical transmission through the nanohole arrays and the role of SPPs. A maxima in transmission would not be expected *a priori* if power should be lost due to the excitation of an SPP wave. While there has been wide agreement as to the essential physics in the past few years (which we discuss at length in Chapter. IV), there were initial objections to these theories (For example, “Negative role of surface plasmons in transmission of metallic gratings with very narrow slits” [16] and similar). At the present time, even, there is still not a single, universally accepted model for this phenomenon as there continues to be objections to various aspects in some circles (see the “coherent diffracted evanescent wave”, or CDEW, model for example [18]).

We demonstrate isolation of surface plasmon polariton mediated resonance transmittance, by means of polarization rotation, through square arrays of cylindrical holes in an optically thick metallic film. Transmittance data for co-polarized and cross-polarized cases are described accurately with a described well with Fano-type and single Lorentzian lineshapes, respectively. This polarization control allows for changing the relative weights of resonant and non-resonant transmission mechanisms, thus controlling the shape and symmetry of the observed Fano-type lineshapes.

In the course of this work we have made a variety of different structures. Not all measurements were made in the same manner for every sample. Due to this limitation, this chapter has been organized in order to present the *ideas* and various dependencies in as clear and consistent manner as possible. To accomplish this, however, we have found it necessary to present data for different samples (primarily using the standard processes described in Sec. III.E with various variations in thickness, hole size, period, etc.) and variations on the basic measurement scheme as presented in Sec. IV.B.1 (illumination sources), interspersed as the various subjects are addressed[1]. Whenever appropriate we will refer to the standard processes described in Sec. III.E.

---

[1] *Caveat lector*

IV.A Analytic model for SPP coupling

IV.A.1 Background of recent literature

Resonant and "enhanced" transmission through subwavelength apertures has been the subject of extensive recent investigations (see Ref. [55] and references therein). Typically, scattering (reflection and transmission) coefficients of any periodic grating supporting a slow wave are characterized by resonant features, e.g. strong resonant peaks in the magnitude of the transmission coefficient through a perforated metal plate, which occur approximately when the wavevector of one of the diffraction orders matches that of a slow wave. These features are manifestations of so-called resonant Wood anomalies [56, 57], occurring at optical frequencies that are typically associated with the excitation of surface plasmon polaritons (SPPs). Mathematically, these anomalies are evident through the presence of complex frequency/angular poles in the scattering coefficient for incident radiation with a given real frequency/angle. When the incident field frequency/angle is scanned through these poles, the scattering coefficient exhibits resonant behavior. In addition to these resonances, a non-resonant field component is always present as well. The superposition of the resonant and non-resonant components results in asymmetry in the shape of the scattering coefficients, resulting is so called Fano profiles [41, 58, 59, 60], which depend on the relation between the magnitude and phase of the resonant and non-resonant components.

The relation between the resonant and non-resonant components depends not only on the structure parameters but also on the measured parameter provided by a specific experimental setup. Indeed, a linearly polarized field upon scattering from a doubly periodic nanohole array generates co- and cross-polarized components. Using an additional polarizer in the scattered field, referred to in the following analysis as an analyzer, allows control of the each of these components of the scattered field and thereby changes the shape of the measured transmitted field. Most of the utilized experimental setups implement measurements of co-polarized incident and scattered field components, thus limiting the observed lineshapes. The objective here is to demonstrate experimentally and analytically the dependence of measured intensity through a periodic array of sub-wavelength holes after analyzing the polarization state of the transmitted optical field for various input polarization states. The presented ideas and results have a wide applicability to the general theory resonant gratings. For example, typically the frequency dependence of the resonant scattering coefficients is associated with red shifted tails [58, 59, 60, 61]. The shape of the scattering coefficient magnitude depends on the relation between both the amplitude and the phase of the resonant and non-resonant components. Within this framework, we show that the entire polarization dependence drops out quite naturally. SPP mediated polarization rotation effects in one-dimensional gratings in conical mounts [62] have recently been extended to investigate far-field scattering from excited SPP waves in two-dimensional nanohole arrays [63, 64, 12, 65].

In this chapter we investigate the polarization properties of the resonant scattering from a two-dimensional nanohole array in a metallic film and show that the shape of the resonant transmission depends on the polarization state of the incident field, the excited SPP mode, and the polarization state of the measuring apparatus- enabling observation of both Fano-type and pure Lorentzian lineshapes. In the following section we will describe the system under investigation, and show typical spectral dispersion measurements to compare them to those existing in the literature. Section 3 is focused on analysis and experimental validation of the polarization dependence in transmission near a single, isolated resonance, followed by developing a phenomenological model which accounts for this polarization dependence. The measured data is analyzed and compared with the developed model, providing insight into the physics of the interference of these scattering processes. Conclusions and a brief summary are given in Section 4.

IV.A.2 Two dimensional grating coupling: phase matching

The geometry for excitation of a SPP wave on a metallic film perforated with an array of cylindrical hole is sketched in Fig. IV.1. A plane wave electromagnetic wave is incident upon a metallic film with dielectric constant ϵ_2, which is deposited upon a substrate material with dielectric constant ϵ_3, from a medium with dielectric constant ϵ_1. The metallic film is perforated with a square array of cylindrical holes, with the film thickness h, hole diameter d, and hole period a. The plane of incidence is defined by wavevectors of the incident, and 0-order transmitted, and reflected beams. This plane of incidence is rotated with respect the to lattice periodicity by some azimuthal angle ϕ, and the plane wave is incident at a polar angle θ, and a reciprocal space definition is illustrated as an inset, and we will often refer to the projection $\mathbf{k}_{//}$ of the incident wavevector $\mathbf{k}$ in one of the high symmetry directions $\Gamma - X$ and $\Gamma - M$. The polarization state of the incident electric field is defined at an angle Ψ with respect to the plane of incidence.[2]

The spectral transmittance of the nanohole arrays has been described recently by a number of authors. An intuitive explanation of the wave phenomena underlying the physics of the transmission through small hole arrays can be given in terms of the SPP excitation [12]. An incident electromagnetic wave excites a SPP when the sum of its in plane component of the wave vector and a combination of reciprocal lattice vectors produce an SPP wave vector- that is, when the following phase matching condition is fulfilled:

$$\mathbf{k}^{spp} = \mathbf{k}_{//} + m\mathbf{K}_x^G + n\mathbf{K}_y^G \tag{IV.1}$$

where $\mathbf{k}^{spp}$ is the surface plasmon polariton wave vector, $\mathbf{K}_x^G$ and $\mathbf{K}_y^G$ are the grating reciprocal lattice vectors in the x- and y-directions, respectively, m and n are integers that describe the various SPP diffraction orders and $k_{//}$ is the in-plane

---

[2] We will primarily refer to a polarization angle Ψ instead of a transverse magnetic (TM or p-polarized) and transverse electric (TE or s-polarized) waves because of the prime importance of mixed modes and polarization states in this work, though these more common polarization terms are occasionally used.

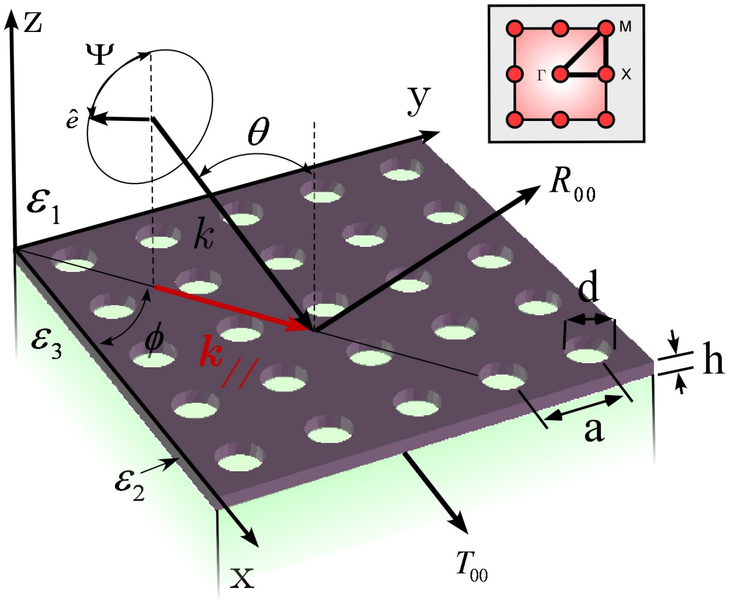

Figure IV.1: Geometry for SPP excitation on a metal nanohole grating. The inset shows the respective directions as defined in reciprocal space.

component of the incident wave vector as defined in Fig. IV.1 and given by:

$$\mathbf{k}_{//} = \mathbf{k}_x + \mathbf{k}_y = k_0 \left(\hat{\mathbf{x}} \sin\theta \cos\phi + \hat{\mathbf{y}} \sin\theta \cos\phi\right) \tag{IV.2}$$

for this square lattice, and reciprocal space grating vectors. where $k_0 = 2\pi/\lambda$ is the free space wave vector, and the polar (θ) and azimuthal (ϕ) angles are as defined in Fig. IV.1. In a first approximation, we assume a small modulation (valid in the limit $d \ll a$) and no coupling between resonances on the adjacent side of the film, such that the magnitude of the SPP wave vector can be approximated by the case of a planar metal surface abutting an adjacent dielectric layer:

$$\left|\mathbf{k}^{spp}_{1-2,2-3}\right| = k_0 \sqrt{\frac{\epsilon_{1,3}\epsilon_2}{\epsilon_{1,3} + \epsilon_2}}, \tag{IV.3}$$

where ϵ_1 (ϵ_3) are the dielectric constants of incident medium (substrate), respectively. Although there are a number of interesting phenomena which involve the coupling between SPP waves excited on opposing sides of the film (double resonances, or "SP molecules"), we limit our present study to the role of SPP in

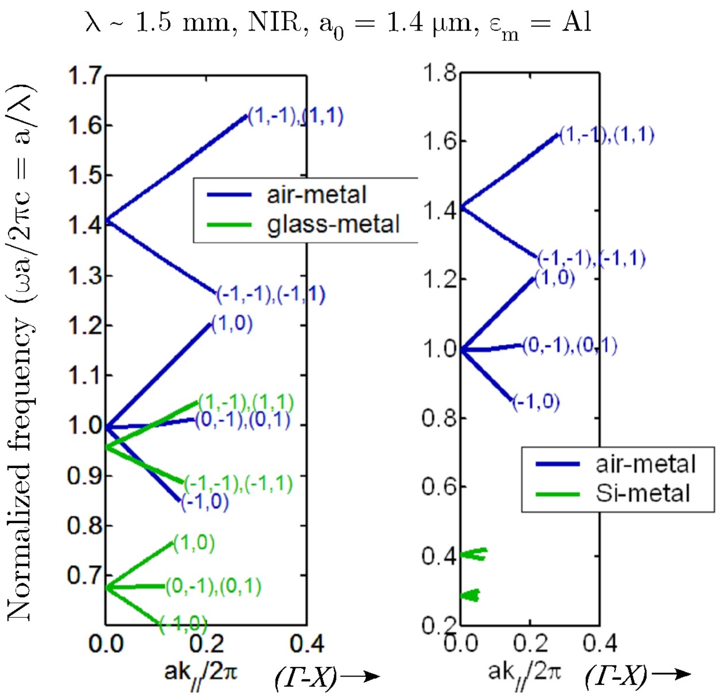
λ ~ 1.5 mm, NIR, a_0 = 1.4 μm, ε_m = Al

(a) (b)

Figure IV.2: SPP phase matching conditions for various metal-dielectric interfaces. (a) show the (b)

enhanced transmittance mediated by its excitation on a single side of the metal film. However, these excitations

In the majority of the recent literature, where excitation occurs at higher frequencies (<1000 nm), many authors [refs] have found this approximation to break down, and typically cite a red shift between the values predicted by Eq. IV.3; we find, however, that in our experimental conditions, these assumptions predict the observed resonance conditions rather well (as will be shown in Sec. IV.B.2).

IV.A.3 Fano mode description of resonant transmission

When the phase matching condition in Eq. IV.1 is satisfied, the incident field interacts strongly with the SPP and this interaction results in strongly enhanced transmission. The phenomena of enhanced transmission can be explained more rigorously as particular manifestations of so called resonant Wood anoma-

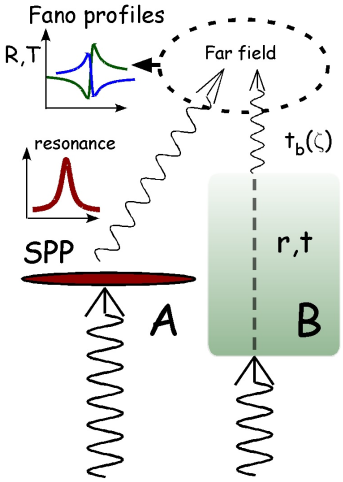

Figure IV.3: Energy space diagram of Fano type interference mechanism between resonant and nonresonant transmission processes. The continuum, either the reflected or partially transmitted field, interferes coherently with the resonant process, the scattered SPP field, in the far-field.

lies [56, 57, 66] that are also associated with Fano profiles. In the framework of the theory of resonant Wood anomalies, the transmission (scattering) coefficients are represented as a sum of resonant and non-resonant components. We show a schematic of the energy space diagram in Fig IV.3.

Considering the transmission coefficient t as a function of either the parallel wave vector $k_{//}$ for fixed frequency ω and the azimuth component of incident angle, or as a function of frequency ω for a fixed angle of incidence, it is written as [56, 57, 66]:

$$t(\zeta) = t_b\left(\zeta\right) + \sum_{n,m} \frac{c_{nm}}{\zeta - \zeta_{nm}}, \tag{IV.4}$$

with $\zeta \in \left\{k_{//}, \omega\right\}$. In Eq. IV.5, the first and second terms in the right hand side are the non-resonant (background) and resonant components in the transmission coefficient. The resonant component is characterized by complex poles $\zeta_{nm} = \zeta_{nm}^{R} + j\zeta_{nm}^{I}$, which satisfy $\zeta_{nm}^{R} \approx \zeta_{nm}^{\text{res}}$ with ζ_{nm}^{res} being frequency/wavevector solutions of Eq. IV.1, and corresponding residues $c_{nm}= \text{Res}_{\zeta_{nm}}\left\{t\right\}$. From Eq. IV.5, the magnitude of the transmission coefficient exhibits strong peaks for $\zeta \approx \zeta_{nm}^{R}$ whose width is determined by ζ_{nm}^{I} which, in turn, is comprised of two components corresponding to the material loss and radiative damping. Physically, the complex frequency poles ω_{nm} characterize resonances, which represent damped exponential fields when the field is excited by a transient source [67]. The complex parallel wavenumber poles $k_{//,nm}$ characterize leaky waves that "radiate" their power out of the perforated plate [66][REFS].

This resonant transmission mechanism, as elucidated by Barnes et. al. [12], involves coupling to an SPP mode, evanescent transmission through the below-cutoff waveguide hole, and scattering of radiation again from the hole array to produce propagating free space modes. The surface wave is excited by a projection of the incident electric field polarization in the propagation direction, and the reradiated field is again projected onto the analyzer. This effect has been explored previously with one-dimensional gratings, and utilized in imaging SPPs excited on two-dimensional SPP grating couplers.

IV.B Experimental setup: far-field spectral measurements

IV.B.1 Measurement apparatus

The basic setup for measuring the spectral transmittance of our nanohole array samples is shown in Fig. IV.4. While the same basic setup is employed, we utilize a number of distinct sources of radiation for different measurements. These sources are:

1. A broadband, tungsten halogen lamp white light (Ocean Optics, multimode, 400 μmfiber coupled)
2. a Thorlabs C-Band (1520-1570 nm, 30 mW integrated PSD) ASE source, single mode fiber and grin lens coupled
3. a C-band tunable telecom test laser (New Focus 6427, ~6 dBm maximum

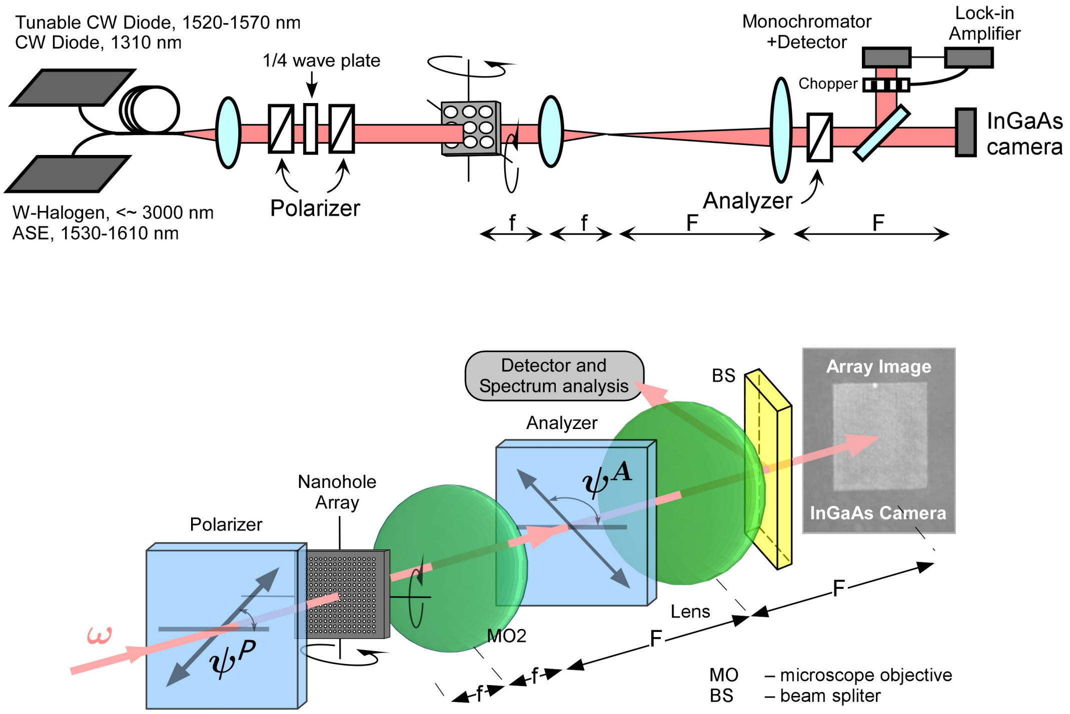

Figure IV.4: Experimental setup for measuring spectral transmittance through metallic nanohole arrays in a conical mount.

power), single mode fiber and grin lens coupled

4. 1310 nm diode laser, OEM manufacturer unknown, ∼1 mW

Illumination from the lamp is collimated, polarized and the central portion of the array is imaged onto the input slit of a monochromator, which scans a fixed spectral range of 1000 nm to 1700 nm.

For alignment and imaging we utilize an InGaAs focal plane array cameras. We describe these cameras in more detail in the section on imaging, chapter V. To prepare the incident field state, we typically use a polarizer/quarter wave plate (not shown) to obtain circular polarization at the input of this system, which can then be linearly polarized with the input polarizer shown.

IV.B.2 Measurement of collinear polarized input and output

In this section we will examine the spectral transmittance through the 2-D nanohole array. We first present data for STA (again, as described in Sec. III.E. For a comparison, we show the measured, zero-order spectral transmission of a “thin” gold film in Fig IV.5, in false color, as a function of frequency and incident wave vector. This data and measurement is similar to that shown in Ghaemi et al. [10], and Barnes et al. [12], though it is important to note that the films measured here are much thinner. The measured transmittance for a number of samples with various periods, has been normalized by the hole area per unit cell and combined to give a full perspective on the SPP excitation conditions for our entire sample and characterization space. The spectra are dominated by transmittance dips at the various SPP excitation conditions, which appear as the set of dark stripes. These major features of the dispersion map are well described by the Eqs. IV.1-IV.3 similar to those shown in Fig. IV.2. Dispersion curves are calculated for the air-metal (AM) and glass-metal (GM) interfaces, shown in Fig. IV.5 (+ direction), and follow the SPP features for all of the data on the normalized frequency scale

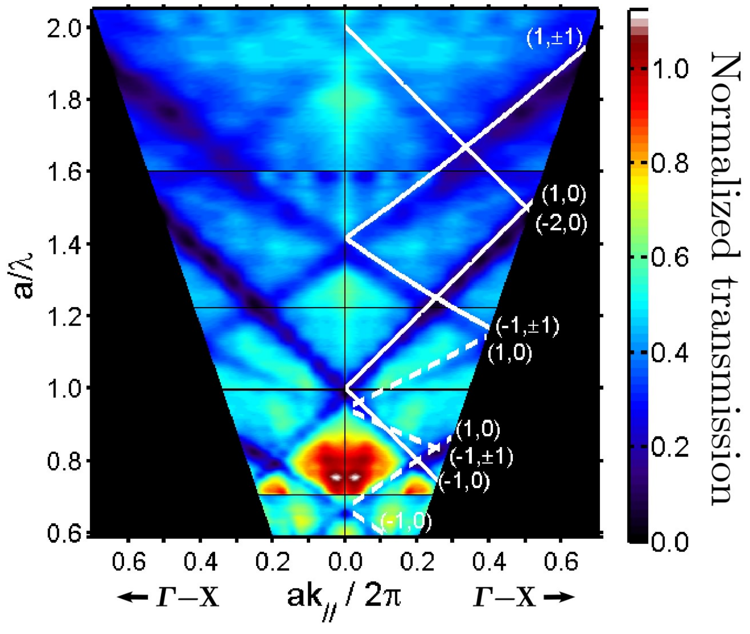

Figure IV.5: Spectral measurements of TM polarized zero-order transmittance (TE data not shown) for square arrays of holes in a thin gold film on a glass substrate. Data from several arrays with different periods a have been combined for these composite intensity images, where the stitching frequencies appear as horizontal black lines [identical data is also replicated for $k_{//} < 0$ for viewing]. The transmittance has been normalized by the hole area per unit cell, and the intensity range is from 0 to 1.1. On the right half (+), the calculated SPP dispersion curves for AM (-) and GM (–) interfaces are seen as white lines.

quite well. Only those modes that are efficiently excited- and therefore appear as spectral features in this data- are shown [i.e. $(m, n) = (0, 1)$ type modes and higher order GM modes have been omitted]. Specifically, we see that the $(1, 0)$ SPP modes of the AM and GM interfaces, as well as the $(1, 1)$ of the AM interface appear under these conditions. The relatively weak coupling to the GM interface (compared to the AM side) is likely due to the damping from the nickel adhesion layer, where the $(1, 0)$ order is observable in the spectrum but the $(1, 1)$ trait appears barely discernible.

We restrict our study to excitation of SPP on one side of the film only, when $|\mathbf{k}^{spp}_{1-2}| \gg |\mathbf{k}^{spp}_{2-3}|$ for any given order (m, n). This assumption means that the frequencies of the lowest order SPP modes excited on the upper and lower interfaces of the metal-dielectric boundaries are well separated in frequency, and therefore there is no coupling between the SPP modes on the opposite sides of the metal film (i.e. under assumption that the coupling to higher order modes is weak). The experimental samples consist of $h \sim 100$ nm aluminum film on a GaAs substrate perforated by a 2-D array of holes with diameters $d \sim 350$ nm and with periods a of 1.2, 1.4 and 1.6 μm. The total perforated area of 200×200 μmwas used for measurements that followed closely the techniques discussed in Ref. [64]. The sample was first aligned normal to the beam axis and the azimuthal angle ϕ was set to a value of either 0 or $\pi/4$ corresponding to the $\Gamma - X$ or $\Gamma - M$ directions in the reciprocal lattice space. At each azimuthal angle, the polar angle θ (i.e. angle of incidence) was varied from 0 to $7\pi/36$ rad (corresponding to about 35°). Measured dispersion for the three samples with various periods, a, is shown in Fig. IV.6(a), displaying the unpolarized (i.e. polarizer/analyzer pair removed), zero-order transmittance for normalized frequency versus normalized in-plane wavevector in both the $\Gamma - X$ and $\Gamma - M$ directions. Data has been normalized by the hole area per unit cell and combined to give a full perspective on the SPP excitation conditions for a large characterization space. The maximum transmission of ($\sim 9\%$ for $a = 1.4$ μm, $\sim 13\%$ for $a = 1.2$ μm) occurs at normal incidence for a slightly red shifted wavelength from that corresponding to $a/\lambda = 1.0$.

The data is dominated by the asymmetric, Fano-type lineshape features, which correlate with resonant transmission by excitation of various SPP wave modes. at the various orders (m, n). The essential feature to notice is that the SPP fields are excited at neither the maxima nor the minima of this curve; rather, the interference between the resonant and nonresonant components leads to the dispersive lineshape. For these samples, as noted above, only SPP modes on the air-metal (AM) interface are efficiently excited; the first order modes for the semiconductor-air interface occur at much lower frequencies, and the higher order modes that occur at these frequencies are clearly not discernable in these measurements.

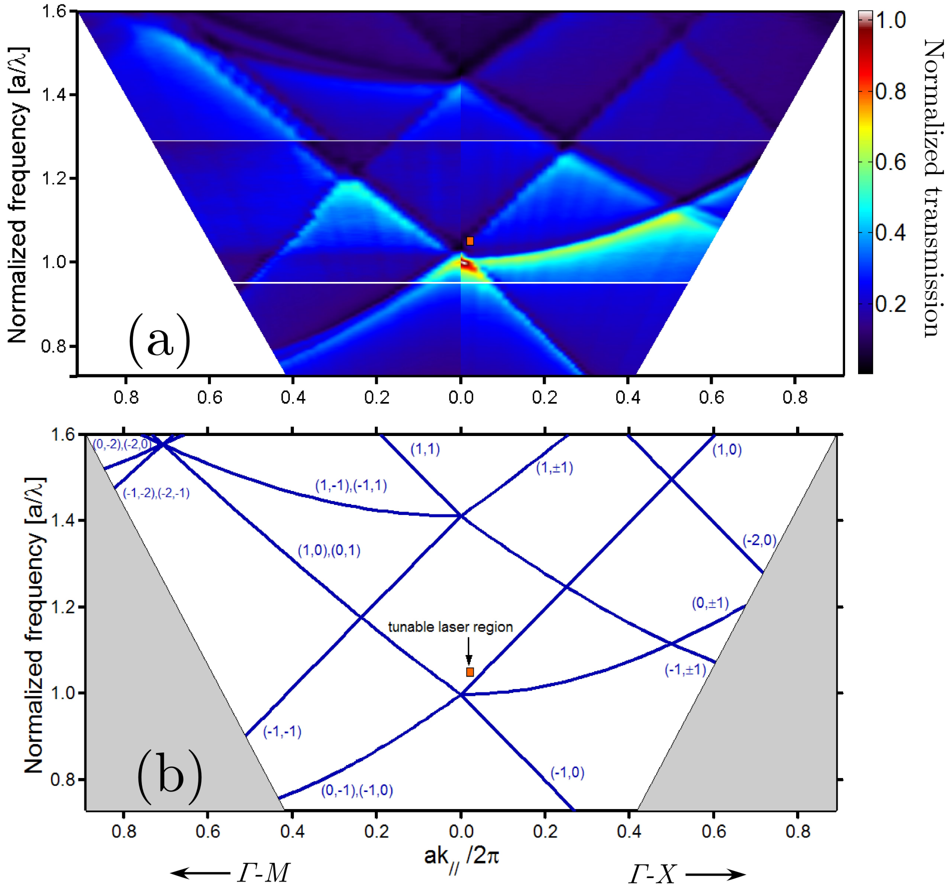

Figure IV.6: (a) Unpolarized spectral measurements of unpolarized zero-order for square arrays of holes in an thin aluminum film on a GaAs substrate. Data from several arrays with different periods a have been combined for these composite intensity images, where the stitching frequencies appear as horizontal white lines. The transmittance has been normalized by the hole area per unit cell. (b) Calculated SPP phase matching conditions for the same parameter space. Also shown in both (a) and (b) is a small box indicating the frequency/wavevector region studied with high resolution in the following sections.

Film thickness: waveguide below cutoff which, and all of our effects are due to SPP field enhancement and scattering through these channels Each of the resonances is characterized by a transmission minima close to a maxima with a red tail. We investigate closer next.

Dispersion curves shown in Fig. IV.6(b) are calculated for SPP excitation at the AM interface for a single period ($a = 1.4$ μm) according to Eqs. IV.1-IV.3 and including the frequency dependence of the dielectric constant of aluminum. These curves predict well the frequency of the SPP features for all of the data on the normalized frequency scale. More rigorous methods are required to theoretically determine the relative strength of the coupling as well as the absolute spectral shape of the various bound and propagating modes (i.e. diffraction orders). Qualitatively, however, there have been a number of studies that have succeeded in explaining the effects of the various geometric parameters on the spectral transmittance. The resonant transmission mechanism, as elucidated in Ref. [12], consists of coupling to an SPP mode, evanescent transmission through the below-cutoff waveguide hole, and scattering of radiation again from the hole array to produce propagating modes. The hole size, in the long wavelength limit, determines the scattering rate of and hence the lifetime of the mode, and increasing size will tend to increase the linewidth of the transmitted radiation.

As a final note, we add that a number of authors have (see for example Refs. [61, 39]) have fit a Lorentzian type dependence to unpolarized transmittance data such as Fig. IV.6(a). This is a As we shall see in the next section, but should properly by applied on to data such as th

IV.B.3 Measurements with orthogonal polarizer-analyzer pair

By suppressing the nonresonant background contribution, the resonant mechanism may be isolated and investigated independently. To do this, we measure the grating array with crossed polarizers. In this case, the resonantly excited SPP waves act effectively as polarization rotators, or, rather, in polarization decomposers . The surface wave is excited by a projection of the incident polarization, and the reradiated field is again projected onto the analyzer. This effect has been explored previously with one-dimensional [62] gratings, and utilized in the study of two-dimensional SPP [altweisher] grating couplers; here, however, we explicitly extend these observations to three dimensions with two dimensional gratings, mapping the resonant transition only while suppressing the background, clearly emphasizing the resonant nature of this transmission mechanism. When the background radiation is suppressed we have a purely Lorentzian type transition [TD, Ebbesen].

We show the transmission for various polarization states in Fig. IV.7. In this measurement, Fig. IV.7(a) is for unpolarized illumination, and shows nearly the same data as in Fig. IV.6, though on a reduced frequency scale. In Fig. IV.7(b), the input polarization state is $\psi^P = +\pi/4$, while the output analyzer is set to $\psi^A = -\pi/4$, and in Fig. IV.7(c) the input polarization state is $\psi^P = 0$, while the output analyzer is set to $\psi^A = +\pi/2$. The excitation of the SPP waves is $\propto \mathbf{E}\cdot\mathbf{k}_{spp}$ [68], while the re-emission is a reverse of this process. At higher incidence angles, the $\mathbf{E}_z$ component of the field becomes more pronounced in the excitation.

In Fig. IV.8 we show the measured transmission, for a single fixed polar angle $\theta = 20°$ as a function of the azimuthal angle ϕ and normalized freqency, for both PP and OP cases. The input polarization angle is labeled above each plot (a-d).

A cross section of this data, for a single incidence angle is shown in Fig. IV.9(a).

We observe a characteristic Fano shape for PP (dotted lines) and a pure Lorentzian shape for OP (solid); with OP the background contribution is suppressed leaving only the resonance component of the transmission. The absolute transmittance is low, -23 dB (0.50%) for PP, due to the small size of the di-

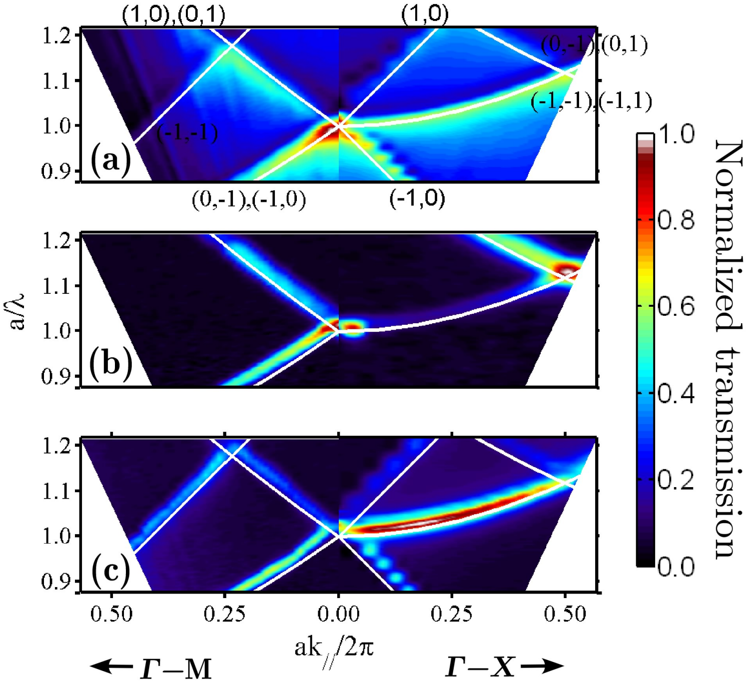

Figure IV.7: (a) unpolarized (b) $\psi^P = +\pi/4,\ \psi^A = -\pi/4$ (c) $\psi^P = 0,\ \psi^A = \pi/2$

ameter of the holes (thus yielding relatively narrow lines), and drops to about -29 dB (0.13%) for OP due to additional polarization projection onto the analyzer. The extinction ratio of $\sim 15 - 20$ dB, limited by the linewidth as well as depolarization due to surface roughness in the etched holes, is shown in the inset of Fig. 2b. Under wavelength interrogation the background level does not drop to the same deep minimum levels within the tuning range of our laser. The measured full-width at half-maximum (FWHM) for wavelength interrogation (Fig. 2a) are 1.28 meV (2.47 nm) and -2.86 meV (5.53 nm) for OP and PP, respectively, and the PP transmission peak is red-shifted from that in OP by 0.40 meV(0.77 nm). Similarly, the measured FWHM for angular interrogation (Fig. 2b) are 0.0012 $ak///2p$ (0.092) and 0.011 (0.87) for OP and PP, respectively, and the corresponding peak shift is 0.0005 (0.04).

We investigate the polarization dependence of the spectral transmittance of this resonant transmission mechanism more carefully in the next section.

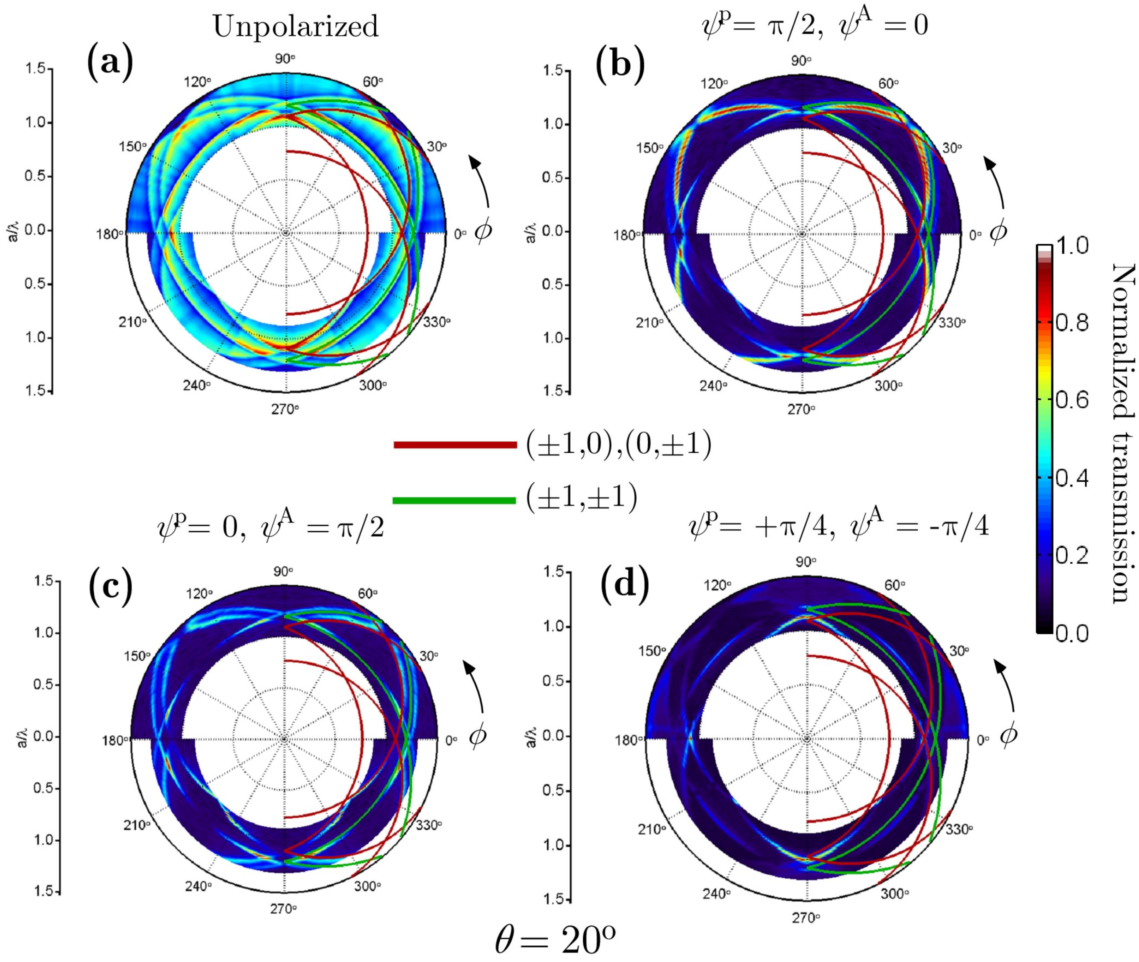

Figure IV.8: Transmittance as function of frequency and azimuthal angle at fixed polar angle of $\theta = 20°$. (a) Unpolarized spectra (b-d) are different orthogonal polarizer-analyzer pair combinations. Measurements for two different samples are shown in the upper and lower half of each plot. Also shown are calculated resonance modes for (1,0) and (1,1) type SPP modes on the right half of each plot.

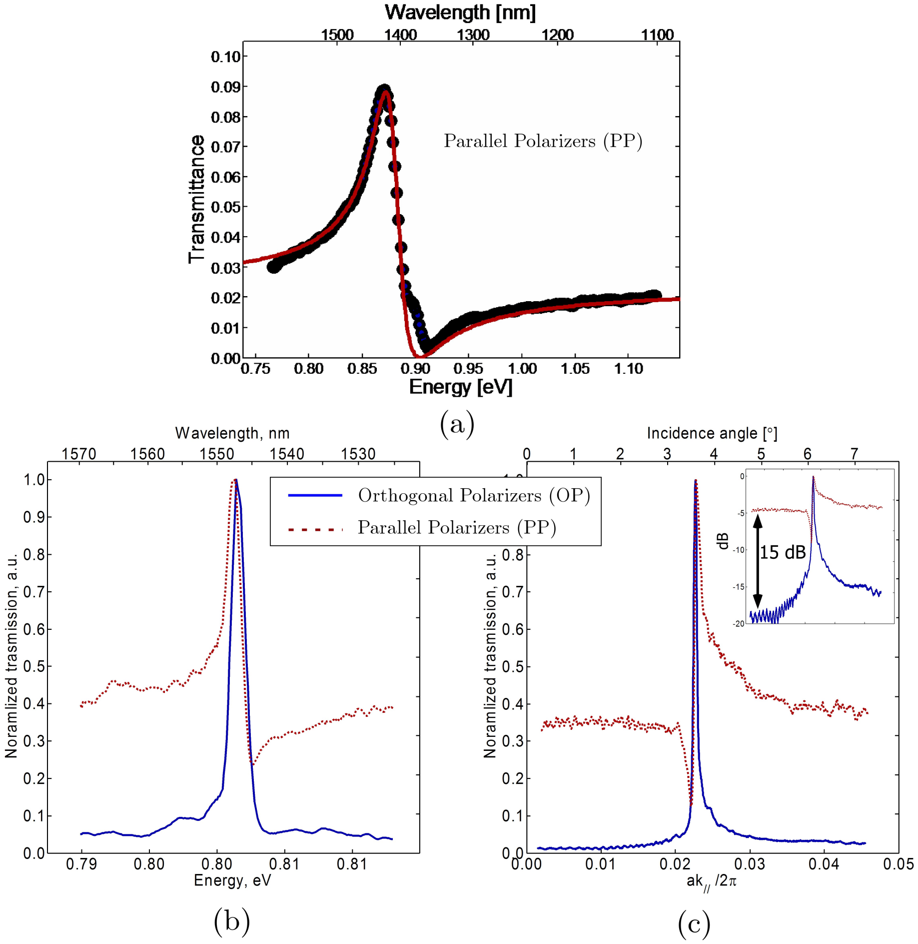

(a)

(b)

(c)

Figure IV.9: Normalized transmission as a function of (a,b) energy (wavelength) and (c) parallel wave vector (angle). Data in (a) and (b,c) are with two different samples as described in the text. In (b,c) the dotted lines correspond to the PP and the solid lines the OP polarization states (as illustrated in Fig. IV.4, also described in the text). The transmission in each case has been normalized to the maximum to clearly illustrate the respective lineshape functions. Also inset in (c) is the same data plotted in logarithmic scale to show the 15-20 dB background level reduction for the Lorentzian vs Fano-type profiles.

IV.C Fano modes: polarization weighting

IV.C.1 Continuous analyzer

We make use of a different sample that facilitates more careful study of the resonant transmission mechanism. The sample consists of an array of holes in gold film on a silica glass substrate with the geometric parameters $h \sim 200$ nm, $d \sim 200$ nm, and $a \sim 1.63\mu$m. The Ti adhesion layer of ~ 10 nm is also used to effectively suppress SPP fields on the gold-substrate interface. At this point, we will focus on examining the polarization dependence of a single resonant mode, (+1, 0). We use a tunable laser with a spectral linewidth much narrower that the SPP resonant transmission linewidth that is tunable in the spectral range of $\lambda = 1520 - 1570$ nm, and will also restrict our SPP measurements to the $\Gamma - X$ direction for a much smaller range of incidence angles θ. This parameter space is indicated by the very small, shaded regions in Fig. 2(a and b). For this sample, the film thickness is larger, the hole diameters are smaller, and the divergence of the beam is smaller, all of which leads to much narrower measured linewidths than shown in illustrated in Fig. IV.6.

The polarization dependent spectral transmission for a fixed value of $\theta = \pi/90$ is shown in Fig. IV.10. The incident field polarizer angle is set to an angle $\psi^P = \pi/4$, and the output field polarization analyzer angle, ψ^A is varied from 0 to π in increments of $\pi/36$. Fig. IV.10(a) shows the measured transmittance, showing a Malus' law-type $\cos^2 \psi^A$ dependence across the entire spectral range. This data has been smoothed (moving average filter) to remove the effects of reflections from the substrate (which had no anti-reflection coating). To see the underlying structure, we normalize the data along the radial (i.e. normalized frequency a/λ) direction for each value of ψ^A to the maximum of each scan in the radial direction, which is shown in Fig. IV.10.

The transmission maximum is clearly seen to vary with ψ^A- most notably, the white, maximum value, is not circular. This is most clearly evident at

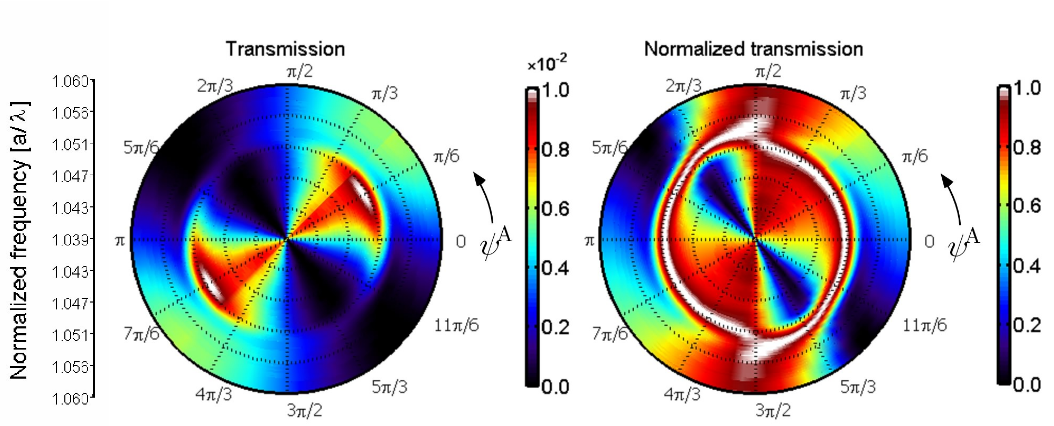

(a) (b)

Figure IV.10: Measured transmittance as a function of frequency (radial direction) and analyzer angle (azimuthal angle). Data in (b) is the same as (a), however, it has been normalized along each ψ^A in the radial direction (normalized frequency, a/λ) to the maximum of each scan for viewing the salient properties of the transmittance.

$\pi/2(3\pi/2)$, where there is a discontinuity in this transmission maximum. Qualitatively, this is a result of a shift due the interaction of the discrete state resonance with the continuum [60]. Moreover, the transmission is never extinguished because of effective polarization rotation by the resonance transmission mechanism. The surface wave is excited by a projection of the incident polarization, and the reradiated field is again projected onto the analyzer. The nonresonant background contribution is effectively suppressed in this case, the resonance isolated and investigated independently. We address this interesting polarization dependence analytically and quantitatively in the next section.

IV.C.2 Analytic theory of polarization weighting

At this point, we will focus on examining the case of a single resonance in the (1,0) (i.e. $\Gamma - X$) direction. For such a single resonantly excited mode Eq. IV.5 can be re-written yielding

$$t(\zeta) = t_b(\zeta) + \frac{c_n}{\zeta - \zeta_n}. \tag{IV.5}$$

As shown in Refs. [57] and [56]], when the background t_b is assumed to be a constant, t_{b0}, Eq. IV.3 may be written in terms of intensity in the form

$$|t(\zeta)|^2 = \frac{\left(\zeta - \zeta_z^R\right)^2 + \left(\zeta_z^I\right)^2}{\left(\zeta - \zeta_n^R\right)^2 + \left(\zeta_n^I\right)^2} |t_{b0}|^2 , \tag{IV.6}$$

where $\zeta_{z,n} = \zeta_{z,n}^R + i\zeta_{z,n}^I$, $\zeta_z = \zeta_n - \nu$ and the coefficient ν relates the ratio of the complex amplitudes of the resonance to background transmission coefficients:

$$\nu = \frac{c_n}{t_{b0}}. \tag{IV.7}$$

Next we investigate the variations in the measured lineshapes as a function of the various polarization states of the input optical field and the output field resulting from interaction with the sample and projected onto the output field analyzer. This process can be effectively described using the Jones calculus formalism. The incident linear polarization state is separated into two components consisting of the resonant and the background field contributions to the transmission through the sample, which are recombined at the output producing a field accounting for the relative amplitude and phase of each component. In general, the output field is given by

$$\mathbf{E}_{out} = \mathbf{R}^{-1}\left(\psi^A\right)\mathbf{A}\mathbf{R}\left(\psi^A\right)\mathbf{M}^s\mathbf{E}_{in}, \left(\psi^P\right), \tag{IV.8}$$

where $\mathbf{M}^s$ is the sample transfer matrix that needs to be determined,$textbfA = \begin{pmatrix} 1 & 0 \\ 0 & 0 \end{pmatrix}$ is the output analyzer and $\mathbf{R}$ is the rotation matrix for the coordinate system shown schematically in Fig. IV.1. The incident, linearly polarized field is given by $\mathbf{E}_{in}\left(z = 0^+\right) = E_0\left(\hat{\mathbf{x}}\cos\psi^P + \hat{\mathbf{y}}\sin\psi^P\right)$. The sample transfer matrix $\mathbf{M}$ then takes the form

$$\mathbf{M}_b^s = t_{b0}' \begin{pmatrix} 1 & 0 \\ 0 & 1 \end{pmatrix}, \mathbf{M}_{res}^s = \begin{pmatrix} c_n' & 0 \\ 0 & 0 \end{pmatrix}, \tag{IV.9}$$

where the subscripts b and res refer to the background and resonant contributions, respectively. Note that the resonantly scattered component results from the excitation and re-radiation of the (1,0) type mode as indicated by a non zero element

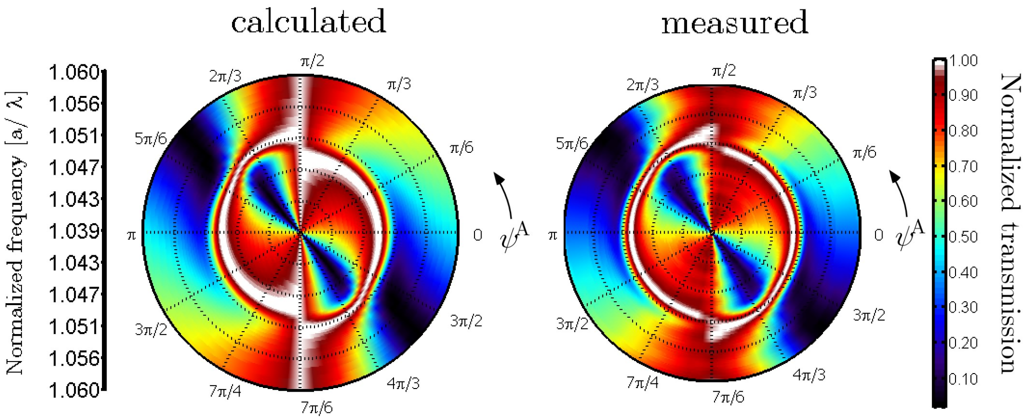

(a) (b)

Figure IV.11: Measured and fitted transmittance as a function of frequency and analyzer angle for fixed $\psi^P = \pi/4$ incident polarization.

c'_n in the matrix $\mathbf{M^s_{res}}$. This leads to the two field components behind the film

$$\begin{aligned} \mathbf{E}_b\left(z=0^+\right) &= t'_{b0}E_0\left(\hat{\mathbf{x}}\cos\psi^P + \hat{\mathbf{y}}\sin\psi^P\right) \\ \mathbf{E}_{res}\left(z=0^+\right) &= \hat{\mathbf{x}}c'_nE_0\cos\psi^P \end{aligned} \tag{IV.10}$$

where $\mathbf{E_b}\left(\mathbf{z}=\mathbf{0}^+\right)$ and $\mathbf{E_{res}}\left(\mathbf{z}=\mathbf{0}^+\right)$ are the background and the resonant field components behind the sample. Upon projection of each of these fields onto the output field analyzer and after some simplification we find that the ratio between the two field components as defined by Eq. IV.7, yields

$$\nu\left(\psi^P,\psi^A\right) = \frac{\hat{\mathbf{e}}^A\cdot\mathbf{E}_{res}}{\hat{\mathbf{e}}^A\cdot\mathbf{E}_b} = \frac{c'_n}{t'_{b0}}\frac{1}{\left(1+\tan\psi^P\tan\psi^A\right)} \tag{IV.11}$$

The intensity transmission, then, can be found with Eqs. IV.6 and IV.11 with the additional substitution $t_{b0} = t'_{b0}\cos\left(\psi^A-\psi^P\right)$ in Eq. IV.6. This substitution introduces the Malus' law dependence, and compensates the poles at angles described in Eq. IV.11.

IV.C.3 Fano measurement results

Fig. IV.11 show both the measured (same as in Fig. IV.10(b)) and fitted spectra according to the model presented in Sec. IV.C.2. Fig. IV.12 shows

Table IV.1: Fitting parameters for both frequency and angular interrogation of polarization dependent transmission.

	t'_{b0}	c'_n	ζ_n
ω	8.15×10^{-2} $-i4.19 \times 10^{-4}$	8.15×10^{-2} $-i4.19 \times 10^{-4}$	8.15×10^{-2} $-i4.19 \times 10^{-4}$
$k_{//}$	8.15×10^{-2} $-i4.19 \times 10^{-4}$	8.15×10^{-2} $-i4.19 \times 10^{-4}$	8.15×10^{-2} $-i4.19 \times 10^{-4}$

both measured (a,b), and calculated (c,d) transmission as a function of normalized normalized in-plane wavevector and analyzer angle for a fixed wavelength of $\lambda = 1545$ nm. Fig. IV.12(a,c) are for $\psi^P = 0$, while for (b,d) $\psi^P = \pi/4$. For the data with $\psi^P = 0$, Fig. IV.12(a), the measured transmission, when normalized as above, is rotationally invariant in the analyzer angle (except at $\psi^A = \pi/2(3\pi/2)$, where the measured transmission is below the noise level for our detection system). For $\psi^P = \pi/4$, the data is similar to that shown in Fig. IV.11, though the sense of the transmission pattern is mirrored with respect to the $\pi/2 - 3\pi/2$ axis. This is the case for the (+1,0) order, but frequency and wavevector maintain the same symmetry for, for example, the (-1,0) order.

For the case of $\psi^P = \pi/2$ (data not shown), the normalized transmission is again invariant to analyzer angle and very nearly constant over this measurement region (the resonance is not excited, and thus only the background contribution is present. The resulting fitting parameters for both frequency and wavevector are given in Table IV.1. Cross-sections of data are shown in Fig. 6(a). Each scan has been normalized to accentuate the lineshape, and the

Fig. IV.13 shows single scans of the normalized transmission as a function of parallel wavevector (a) and normalized frequency (b) for three analyzer angles. These cross-sections have each been normalized to its maximum of each accentuate and compared the lineshapes. For $\psi^A = 3\pi/4$ (middle curve), the pure Lorentzian type lineshape is clearly observable. $\psi^{A1} = \pm\pi/9$ for 1 and 3 and

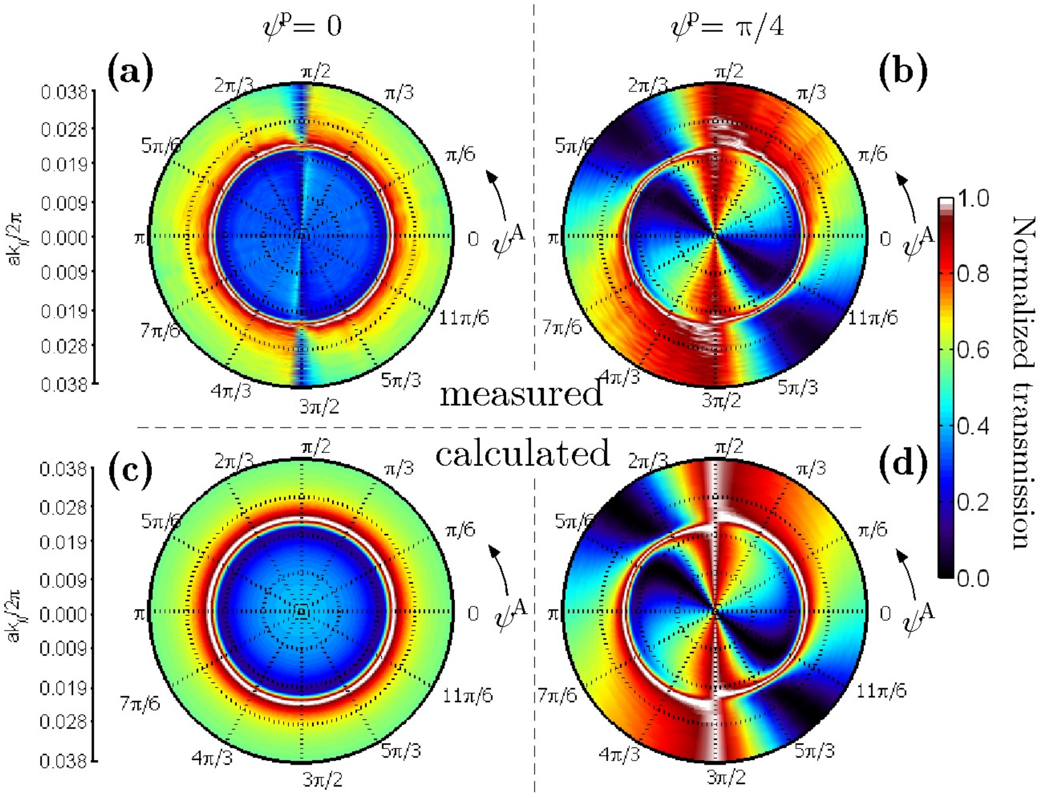

Figure IV.12: Measured and calculated normalized transmission as function of wavevector and ψ^A at fixed frequency for two input polarization states-(a) and (c) are $\psi^P = 0$, whereas (b) and (d) are with $\psi^P = \pi/4$. Data has been normalized along the radial direction ($ak_{//}/2\pi$) in the fashion described in Fig.IV.10. (a) and (b) are the measured data, and (c) and (d) are the calculated values as fit using the model described in the Sec. IV.C.2.

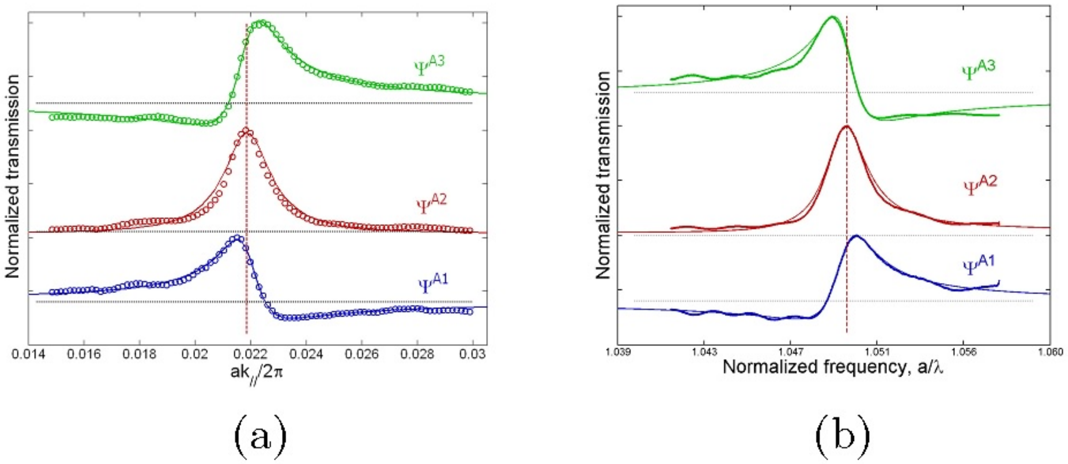

(a) (b)

Figure IV.13: Transmission data for various polarization states demonstrating various Fano type lineshapes. Data has been normalized along the radial direction $(ak_{//}/2\pi$ and offset vertically for clarity. Dotted lines merely serve as guides to eye. $\psi^{A2} = 3\pi/4$, and $\psi^{A3}(\psi^{A1})$ is $+\pi/9(-\pi/9)$ from this value.

the two normalized curves display nearly mirror symmetry about the resonance frequency (sketched as dashed red, vertical line).

This behavior may be understood simply by looking at the relative phase of the two contributions, as diagramed in Fig. IV.14. As the analyzer is rotated about $\psi^A = \pi/4(7\pi/4)$, the sign of the projected background component is inverted with respect to the resonant field component. The same situation occurs at $\psi^A = \pi/2(3\pi/2)$, only in this case there the role of the resonant and background contributions is reversed and there is the energy splitting as noted above.

Next we comment on the difference in the shape of the frequency and angular dependence of the transmission coefficient magnitude. For the frequency dependence, the relative position of ω_n^R and $\omega_{z,n}^R$ is independent of n, the order of the SPP mode. For instance, it is known that when the polarizer and analyzer are co-polarized $\omega_{z,n}^R > \omega_n^R$. On the other hand, for the angular dependence, the relative position of $k_{//,n}^R$ and $k_{//,z,n}^R$ for mode $n = -1$ is opposite as compared to that for the mode $n = 1$. For instance, it is known that for collinear polarizer and analyzer, $k_{//,z,n}^R > k_{//,n}^R$ for $n = -1$ and $k_{//,z,n}^R < k_{//,n}^R$ for $n = 1$ [2,20]. An interpretation

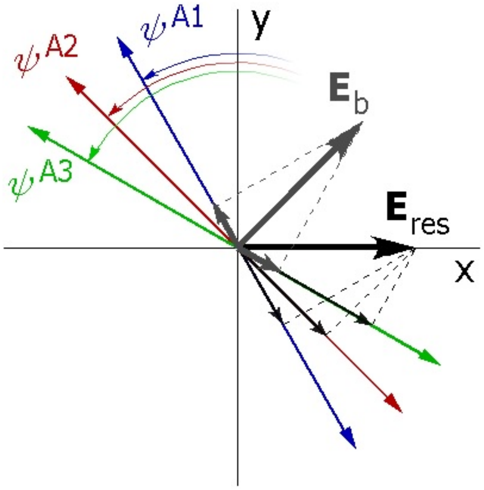

Figure IV.14: Graphic schematic of polarization weighting and resonant and non-resonant component decomposition onto the analyzer.

of this behavior can be given based on the physical meaning of the complex poles ω_n and $k_{//,n}$. The complex frequency poles ω_n always reside above the real axis of the complex ω plane [16]. Therefore, when the resonances are excited by a physical (causal) source, they correspond to a causal time domain signals whose excitation coefficients, viz. the corresponding residues, are taken with the identical sign independently of n . On the other hand the complex poles $k_{//,-1}$ and $k_{//,1}$ correspond to improper (decaying out of plate) and proper (growing out of plate) leaky waves, respectively, since they reside above and below the real axis of the complex plane [2,17-20]. Moreover, these leaky waves are backward and forward waves, viz. waves that have opposite and identical sign of the phase and group velocities [2,17-20]. Therefore, the leaky waves associated with $n = -1$ and $n = 1$, when excited by a physical (e.g. point/dipole) source, exist only in the regions $\Re\{k_{//}\} < k_{//,-1}$ and $\Re\{k_{//}\} > k_{//,1}$, respectively, and their excitation coefficients, i.e. corresponding residues, are taken into account with opposite sign (as follows from the asymptotic analysis [20,22]). This interpretation is valid not only in the case of collinear but also in the case of cross-polarized analyzer. The latter allows modifying the non-resonant contribution thus modifying the parameter ν, which, in turn, results in modified symmetry of the shape of the transmission coefficient

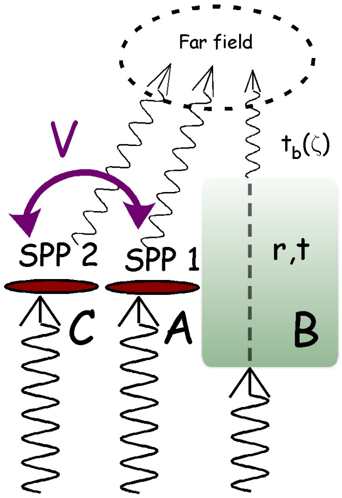

Figure IV.15: Energy space diagram for degenerate SPPs and nonresonant transmission. An additional coupling term V is present between SPP modes.

magnitude in Fig. IV.13.

IV.C.4 Degenerate resonant modes

There are number of instances where a more complicated situation arises where there may be more than one SPP mode simultaneously at the same frequency. These degenerate modes may occur either on the same side of the film or on opposite sides depending upon the specific situation.[3] The energy space diagram for such a situation is shown in Fig. IV.15, where there is an extra coupling term V between the two resonant modes.

To date, we have not done extensive studies into this coupling, and this is a subject for future studies in this area. There have been several recent theoretical [65] and experimental [61] investigations into this type of system.

One specific case we have measured, where two modes, $(+1, \pm 1), (-1, \pm 1)$, are crossing is shown in Fig. IV.16. In this case, there is a fluidic overlayer that is used to tune the resonance frequency to the narrow band of the laser illumination source. This procedure is explained in detail in Chapter VII. The PP illumination

---

[3] As noted before, when the resonant modes reside on opposite sides of the film, authors have referred to this as a “plasmon molecule”.

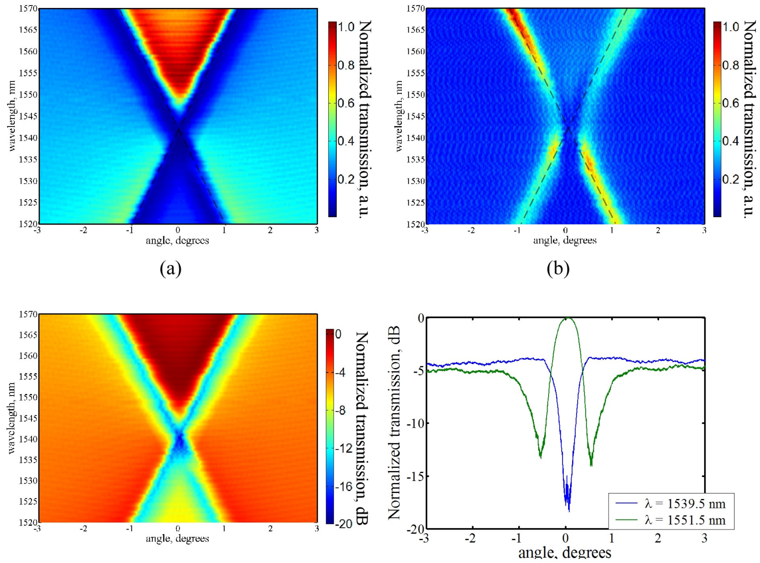

(a) (b)

(c) (d)

Figure IV.16: High resolution transmission in the vicinity of $(+1, \pm 1), (-1, \pm 1)$ mode crossing. (a) PP illumination. (b) OP illumination. (c) Same data as in (a) but on a logarithmic scale. (d) Single cross sections as function of angle for two different wavelengths (1539.5 and 1551.5 nm).

is shown on a linear scale (a) and on a log scale (b). OP illumination is displayed in (b). In (a) and (b) the two lines are shown as guides to the eye to compare the two measurements directly. A weak coupling and splitting can be seen in (b), while in (c) a deep minimum is observed ($>$ 10 dB less then than the background). In particular, this coupling strength should be larger at higher frequencies (closer to the plasma frequency). Some of these preliminary results are to be detailed more thoroughly in ongoing and future experimental and theoretical studies.

At this point, we will introduce a method for directly observing propagating SPPs- not just inferring their existence from circumstantial evidence.

The text of Chapter Four in part is a reprint of the material as it appears in the following publication:

- K.A. Tetz, L.Pang, M. Nezhad, and Y. Fainman, “Polarization weighting of Fano-type transmission through metallic nanohole arrays”, (*submitted, Optics Express.*

- K. Tetz, L. Pang, and Y. Fainman, “High-resolution surface plasmon resonance sensor based on linewidth-optimized nanohole array transmittance”,Opt. Lett. 31, 1528-1530 (2006).

The dissertation author was the primary researcher and author. The co-authors listed in these publications directed and supervised the research which forms the basis for this chapter.

V

SPP excitation and direct imaging

In this chapter we focus on direct observations of light scattered from SPPs propagatng on and between metallic nanohole arrays. One of the motivations for this work was the report that there was no observable spreading of optical fields in the lateral directions when a nanohole array was illuminated with light with a finite spatial extent. In one of the earliest investigations of the phenomena by Thio *et. al.*[1] [69], the authors state:

> The surface plasmons excited by the incident light were expected to propagate along the surface and to cause reradiation from holes located within a radius given by the mean free path of the surface plasmons ($[\delta_{SPP}]$ ≈100 μmon a smooth Cr surface). In fact, to within the dynamic range of the experiment, no light was observed emerging from the back of the perforated film other than at the location of excitation. It is possible $[\delta_{SPP}]$ is reduced sharply by the presence of the holes, but a reduction by two orders of magnitude seems excessive. It is more likely that the decay length remains large, $[\delta_{SPP}] \gg a_0$, but the surface plasmons are confined to the immediate environment of the excitation, scattering from only the nearest neighbors (and perhaps the next-nearest ones) to generate standing waves with high amplitude in the vicinity of the excitation.

Until recently, there had been no follow up to these observations- however, a number of authors have initiated studies of nanohole arrays with near field imaging

---

[1] This is the same group as the seminal work of Ebbesen et. al. [9].

techniques, with a number of interesting results [70, 71], and there will likely be many more in the near future. It is not clear why no lateral spreading of the SPP field was seen in this quoted experiment, however. There are probably, in fact, several reasons including: choice of illumination conditions (the authors employed a tapered fiber, but do not indicate the wavelength used), as well as a possible significant overestimate of the material damping of Cr (again, depending on the wavelength utilized in the experiment).

In this chapter we describe the simultaneous excitation and direct far field imaging of the scattering from SPP modes in a two-dimensional metallic hole array grating. Conditions for the coupling and imaging are discussed, where the coupling is shown to be consistent with both measured and calculated dispersion relations. Excitation is accomplished at several different wavelengths [from 1.31 to 1.57 μm], incidence angles, and grating periods, enabling the observation of a number of distinct modes with various in-plane wave vectors.

We first demonstrated the technique described here in Ref. [72], and it has since been replicated at higher frequencies by Altewischer *et. al.* [73]. Interestingly, these author observe other features that would be expected after the discussion of coherent interference in the discussion of Sec. IV.C; however, we use a slightly different experimental and structural parameters in our measurements, and typically do not see these same spatial interference effects in the results reported here.

V.A SPP imaging principles

Due to the surface nature of the SPP wave, it is not typically possible to observe them directly in the far-field. Imaging has been accomplished in a variety of ways including near-field probing [74][61][70], fluorescence imaging[75], light scattering from surface roughness [76][77] and, more recently, Fourier domain observations of scattering in a grating array [63]. While it is well known that a grating can overcome momentum mismatch for the excitation of SPPs (as described

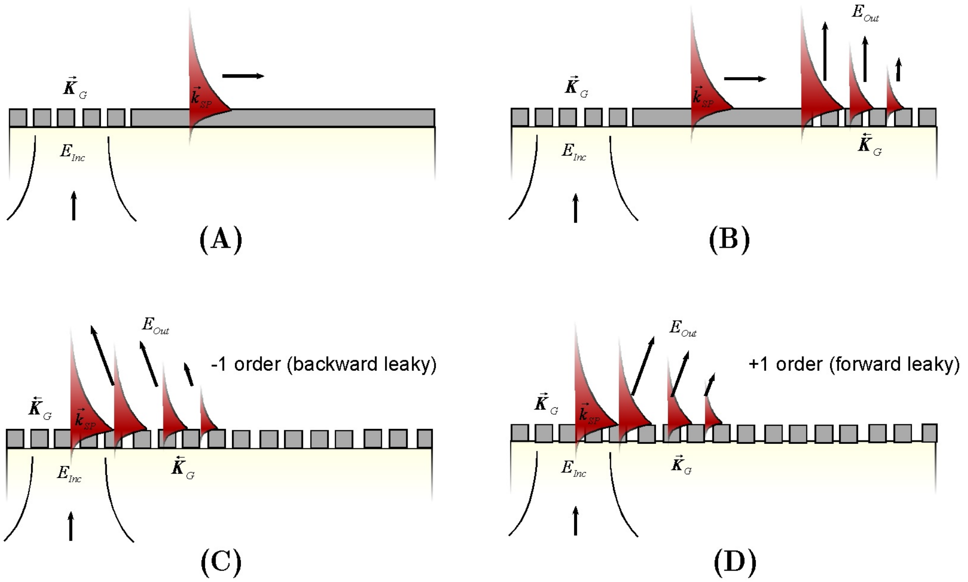

Figure V.1: Schematic diagram for various coupling configurations. (a) SPP propagating on interface (b) Propagating SPP coupled out by second grating (c) Continuous scattering of propagating SPP into a -order or “backward leaky wave”. (d) Same as (c) with a +order “forward leaky wave”.

in Sec. II.C, they had previously not been utilized to enable imaging in the far-field from partially scattered SPPs with an appreciable propagation length. One plausible explanation is that much of the work described thus far has been done at visible wavelengths (or $\lambda < \ 1\mu m$). The damping of propagating SPP waves decreases dramatically from the visible portion of the spectrum into the near-infrared [1][2][78], leading to several advantageous properties of SPPs at these wavelengths.

V.A.1 Basic principles

The basic principles for excitation of SPP modes via a grating coupler, and specifically a nanohole array grating coupler, are shown in Fig. V.1. This is in the same vein as that described in Chapter II, Sec. II.C, but with a few modifications. First, we assume an excitation field with a finite spatial extent, and for this work we will always be a converging Gaussian beam. The beam is incident from

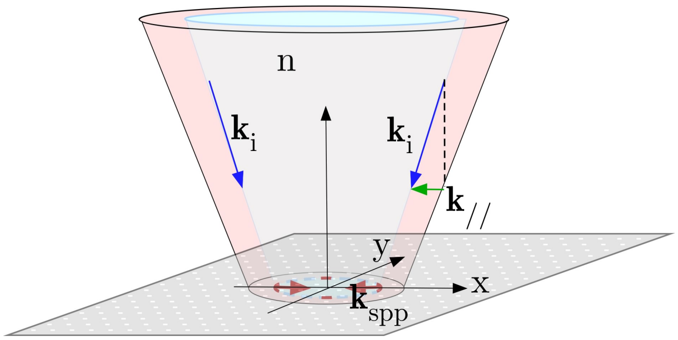

Figure V.2: Illustration of focused incident illumination on a metal nanohole array, with a ray optics approximation of the SPP excitation conditions. Illustrated propagating SPPs are the propagation direction for positive SPP orders.

below, and excites an SPP mode which propagates along the top surface. This is the bound mode, and to get an idea of the propagation characteristics, one may incorporate another grating at some other point in space along the propagation direction as illustrated in Fig V.1(b). The SPP mode is then scattered by this surface modulation, decays more quickly than simply propagating on the planar interface, and this light may be collected and the resulting image magnified at some distant plane. Because of the finite spatial extent of the illumination function, we may also choose to look at a structure where the grating (holes) are continuous across the surface as illustrated in Fig. V.1(c,d). The light scattered from the SPP may still be separated from the illumination spot (and that amount of incident power not coupled into the surface mode), but this may be more difficult depending on the coupling efficiency/scattering rates. We also note that same basic configuration may be applied in a reflection geometry (SPP mode may be on either side of the metal film layer).

Focused illumination is illustrated in Fig. V.2. In contrast to a single plane wave, when using a Gaussian beam illumination, we necessarily have a superposition of a large number of incident wavevectors upon the nanohole array. The spatial frequency content is limited by the numerical aperture (NA) of the focusing lens used, and there is cylindrical symmetry. These spatial frequencies are then weighted in amplitude by the Gaussian intensity distribution of the incident beam, and specific wavevectors are selectively coupled to propagating SPP modes. Only those portions of the incident, focused illumination that satisfy the phase matching conditions (Eqs. IV.1-IV.3) are coupled into propagating SPP modes as illustrated in Fig. V.2.

In Fig. V.3 we show the phase matching conditions, solutions to Eqs. IV.1-IV.3, as a function of both the polar angle θ and the azimuthal angle ϕ for various period to wavelength ratios $a/\lambda = 0.90$. The contours are also shaded by an approximate Gaussian illumination function for illumination with an MO of NA = 0.5. This view also gives a crude estimation as to the point in space where the various SPP modes will be excited.

V.B Experimental configuration

The experimental apparatus is illustrated in Fig. V.4, which is basically the same as that illustrated in Fig. IV.4, with the addition of a focusing microscope objective (MO) before the sample. The focused laser beam of varying frequency was used to excite and image the grating scattered leakage from propagating SPPs. An InGaAs focal plane array was used for imaging and alignment. For the laser illumination, a MO with relatively low NA = 0.25 is used to focus the beam to a spot of $\approx 10\mu$mon the sample, and another MO ($NA = 0.25$) and lens ($f = 125\ \mu$m) pair is used to image the array under observation. In addition, a polarizer-analyzer pair is used to control the polarization state of the excitation field and the field in the image plane, as described in detail shortly. This apparatus is similar to that illustrated in Altewischer et al. [63], except the CCD is at an image plane rather than a Fourier Transform plane, and is sketched in Fig. 2.

We use one of two cameras, both from Indigo Systems (now part of FLIR systems). Boths utilize the same detector array chip: a 320(H) x 256(V), pixel size $30 \times 30\ \mu$m, and linear dynamic range 69 dB. The Alpha uses only 12-bit digital sensor output and must be computer controlled, while the Merlin provides both

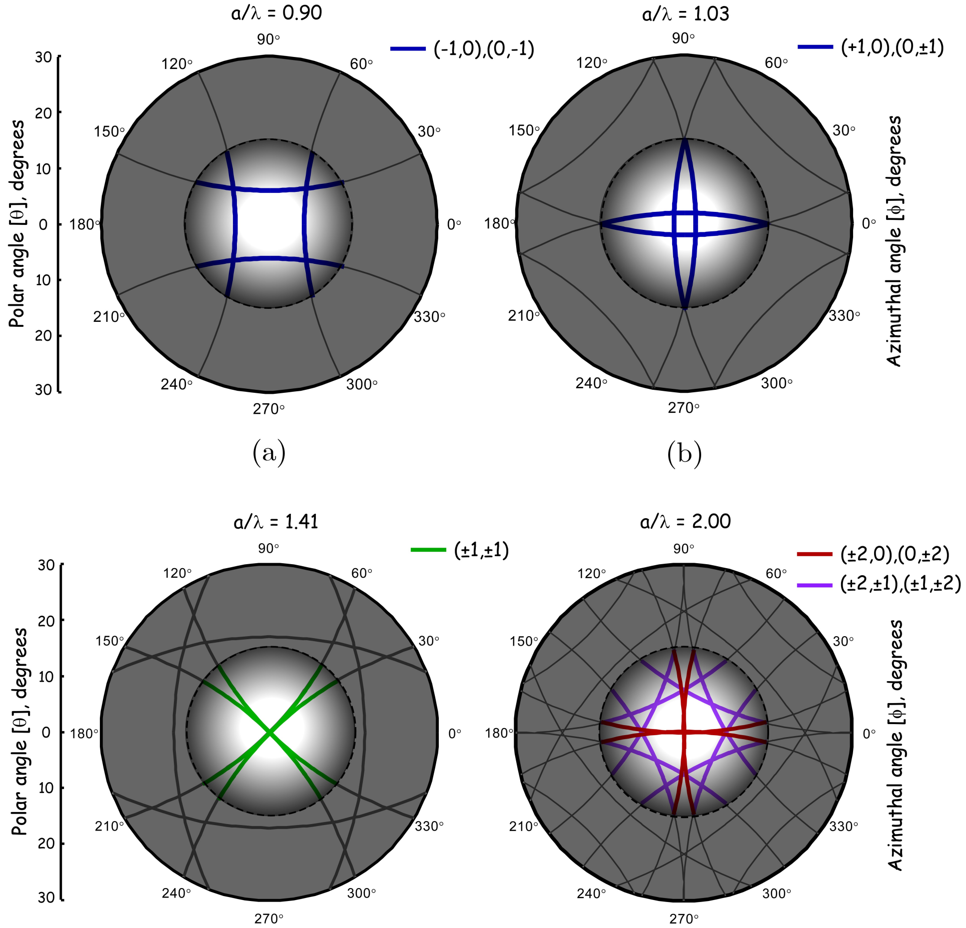

(a) (b)

(c) (d)

Figure V.3: Phase matching conditions as continuous function of the incident polar angle, azimuthal angle, and Gaussian illumination function for various period to wavelength ratios: (a) $a/\lambda = 0.90$ (b) $a/\lambda = 1.03$ (a) $a/\lambda = 1.41$ (a) $a/\lambda = 2.00$

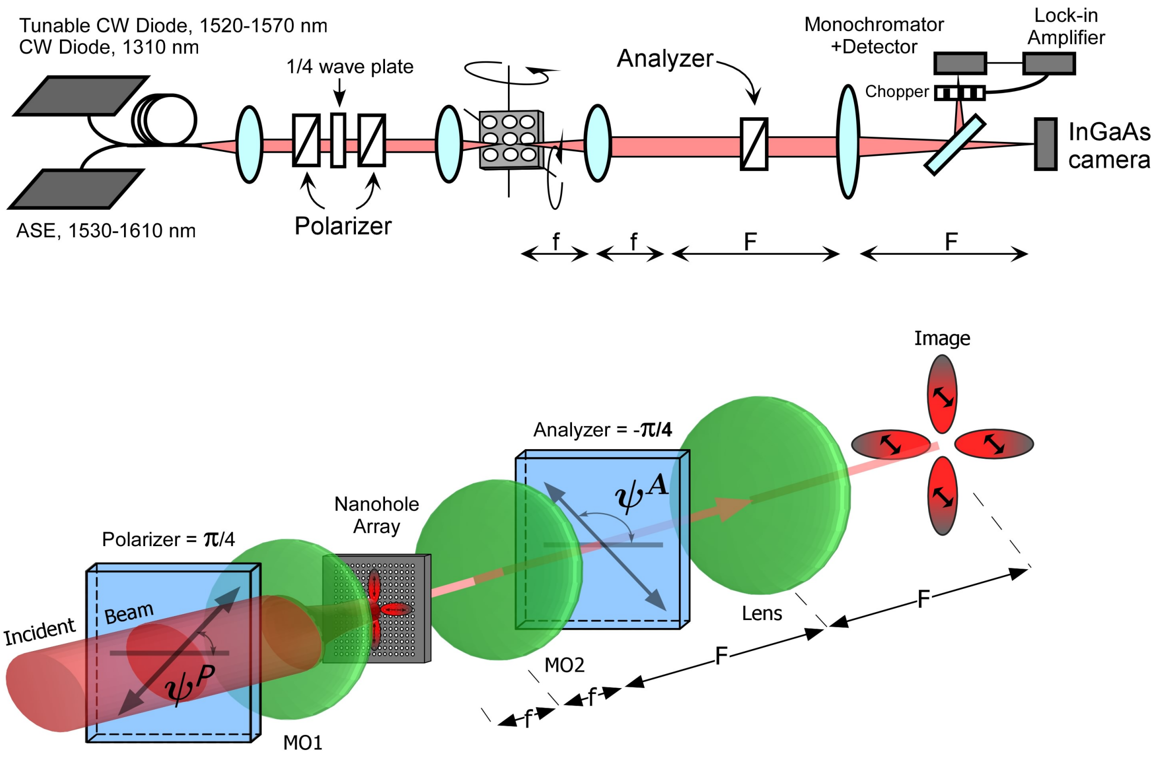

Figure V.4: Experimental configuration for imaging SPP modes in nanohole transmission.

the sensor output as well as a processed 8-bit analog NTSC output that may be viewed on a standard CRT monitor, and also has a on board acquisition controls.

While we have not used the technique, one may improve the imaging capabilities of the imaging by using high-dynamic range whereby the integrating time of the sensor array is varied to acquire signals of different orders of magnitude, and later stitched together digitally in postprocessing. [2]

The final component of the imaging technique is illustrated in Fig. V.5. The incident field is linearly polarized and focused to a spot on the sample. SPP modes are excited, and propagate outwards according to the particular phase matching condition for the given mode- in this case a ±1 type order. The analyzer position may then be set orthogonal to the position of the incident field. In this case, the uncoupled, background transmitted light is extinguished because of this analyzer. The SPPs are also coupled into the various orders. In the center portion of the beam, where the SPPs overlap in space, the effective polarization state remains the same as that of the incident field. Outside of this overlap region, because the SPP modes are polarized along there direction of propagation, the field scattered out the backside of the sample by these SPPs is not extinguished by the anaylzer (only reduced by an an additional factor of 2 in this example). The SPPs have therefore effectively changed the state of polarization of the light that is imaged through the analyzer and onto the detector plane; or in other words, there is a space-variant polarization state. In Fig. V.5(a,b) shows illumination on of STB with both a parallel polarizer/analyzer pair (a) and an orthogonal polarizer/analyzer pair (b) equal camera integration times. In Fig. V.5(c,d) sample STA for a (+2,0) type mode is shown, also for equal integration times. The background is very strong and saturates the camera in (c); however, in (d) the orthogonal polarizers effectively suppresses all this background, and the image of the SPP modes is clearly seen.

---

[2] Calibrating and guaranteeing linearity over a large range of integration times to achieve a higher dynamic range, while quite possible, is somewhat more complicated in practice for an InGaAs focal plane array of detectors than the equivalent silicon CCD camera sensor array.

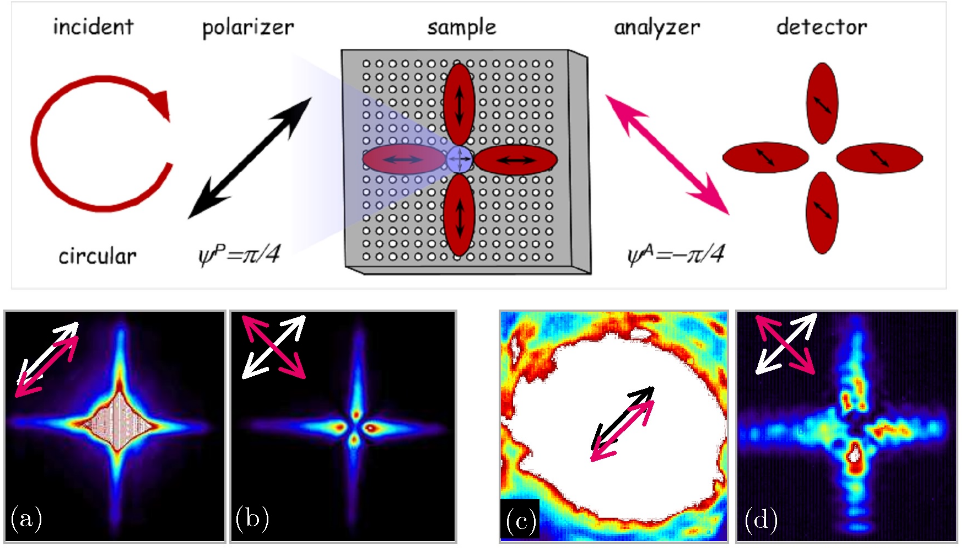

Figure V.5: Polarization separation of surface modes and transmitted light in SPP imaging. Top: incident linear polarization excites four SPP modes, and the central portion is nulled by the orthogonal analyzer. Bottom: different polarizer/analyzer configurations (a) PP (b) OP for (+1,0) modes on STB or a “thick” aluminum film. (c) PP (d) OP for (+2,0) modes on STA or a “thin” gold film.

V.C Experimental results

We continue by showing the imaging in the thin (40 nm) gold film (STA). Inclusion of the Ni adhesion layer adhesion layer affects the SPP modes at this interface (stronger damping, in particular), modifying those that would otherwise exist at the glass-gold interface [40][41]; we will therefore refer, instead, to a glass-metal (GM) interface.

Also sketched in Fig. V.6 is the angular spectrum for the excitation with the single frequency sources, defined by the Gaussian spectrum of the incident laser beam, and the angular bandwidth of the MO.

V.C.1 Imaging SPPs on thin gold films

Light scattering from SPPs observed under various conditions is shown in Fig. V.7 (with each period to wavelength ratio labeled as an arrow at the corresponding frequency in Fig. V.6). At these frequencies, when the phase matching

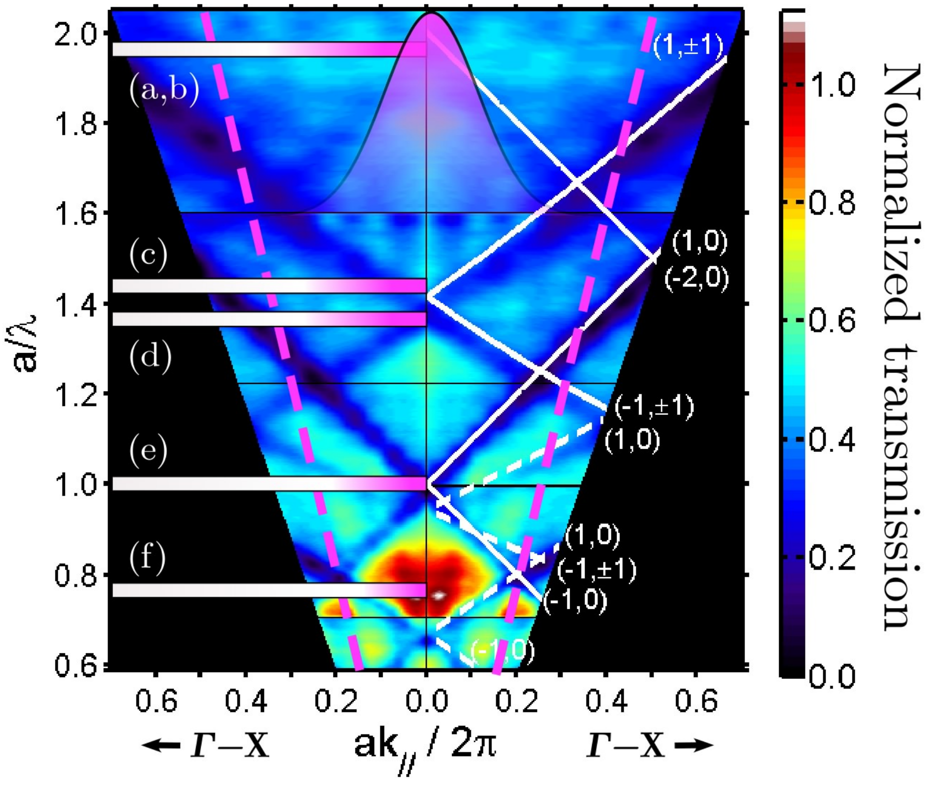

Figure V.6: . Spectral measurements of TM polarized zero-order transmittance (TE data not shown) for cubic arrays of holes in a thin gold film on a glass substrate. Data from several arrays with different periods a have been combined for these composite intensity images, where the stitching frequencies appear as horizontal black lines [identical data is also replicated for ¡ 0 for viewing]. The transmittance has been normalized by the hole area per unit cell, and the intensity range is from 0 (dark) to 1.1 (light). On the right half ($+ak_{//}/2\pi$), the calculated SPP dispersion curves for AM (-) and GM (–) interfaces are seen as white lines. Arrows on left indicate position on normalized frequency axis where single frequency laser measurements (shown in Fig. 3) occur. Also sketched (dotted white lines) is the angular spectrum and relative intensity for the incident beam of Fig. 3, with an NA of 0.25.

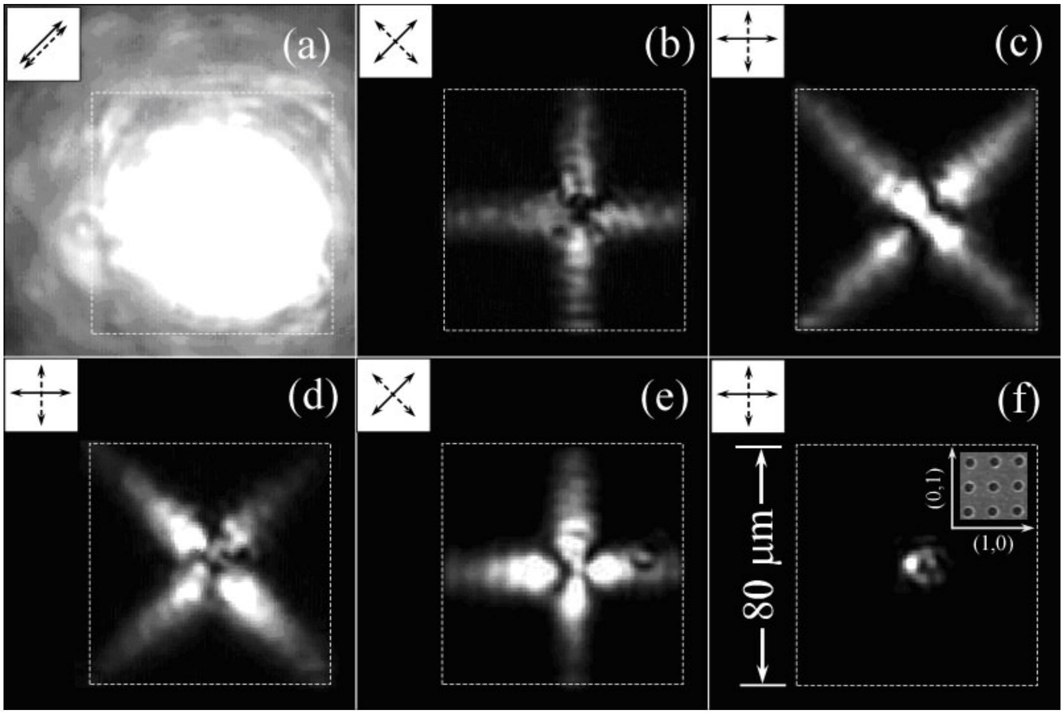

Figure V.7: SPPs observed in various hole arrays. Inset is the relative polarizer (solid) and analyzer (dashed) orientation for each image. Intensity scales for (a) and (b) are identical, while (c) - (f) have been adjusted to observe the full SPP extent. Also inset in (f) is a distance bar valid for all optical images, and an SEM image that shows a representative array and the hole orientation relative to the optical images. The respective hole period a and free-space laser wavelength λ are (in μm): (a)-(b) $a = 2.60, \lambda = 1.31$ (c) $a = 2.20, \lambda = 1.52$ (d) $a = 1.80, \lambda = 1.31$ (e) $a = 1.60, \lambda = 1.57$ (f) $a = 1.20, \lambda = 1.52$.

conditions are satisfied, an exponentially decaying SPP mode is excited in a direction dictated by the resultant SPP k-vector. This is seen as crossed lobes extending out from the center of the illumination spot. In Fig. V.6(a) and Fig. V.6(b), the excitation and imaging conditions are identical; however, in V.7(a), the polarizer and analyzer are parallel at 45 [the (1,1) direction)]. In V.7(b), the analyzer is instead rotated to -45, which effectively nulls the uncoupled, zero-order transmitted beam. Note that (a) and (b) correspond to excitation of (2,0), (0,2) modes, and, although weak, are readily observable. This is in contrast to the spectral data, where the excitation of these modes is below the SNR for our setup (Fig. V.6). Fig. V.7(c)-(f) each show images for other experimental conditions: V.7(c) and V.7(d) correspond to excitation of (1,1) type modes at different frequencies (in different hole arrays); (e) shows (1,0),(0,1) excitation; V.7(f) shows an image when there is no excitation- the intersection of the angular intensity profile and the period to wavelength ratio do not lead to excitation of any mode with appreciable efficiency. Note also that (f) is at a position of maximum transmittance at zero polar angle, and we clearly see that excitation of propagating SPPs do not enhance that transmittance for our thin films. The SPPs in all cases can only be observed to propagate to the end of the grating, although they assuredly continue on the unmodulated surface.[61, 70] Of particular interest is the SPP propagation length, which, for this case of a grating modulated surface, is dependent upon both the radiative decay as well as the material damping. The radiative decay of the SPPs must be small enough to observe the spreading of the field over these relatively large distances [several 10s of μm's], which we discuss analyze more thoroughly in Sec. V.D.

Fig. V.8 demonstrates excitation of both (+1,0) and (1,-1) at the same nominal polar angle of 11° (though the illumination still has the same convergence with the NA of 0.25 as described above). By rotating the polarizer-analyzer pair, we can excite and observe the different modes separately or simultaneously. Fig. V.8(a) shows the (polarizer,analyzer) at $(0°, 90°)$, where only the (1,-1) mode

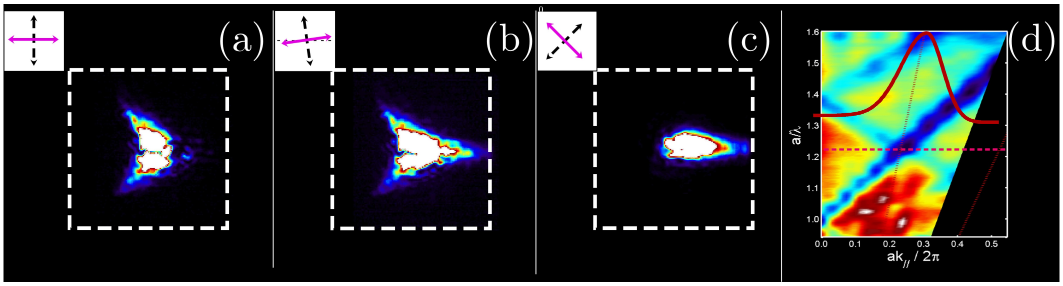

Figure V.8: Images from (+1,0) and (0,-1) SPP modes excited in an array with $a = 1.60\mu m$, $\lambda = 1.31\mu m$ at a nominal polar angle of 11. In each image, the relative orientation of the (polarizer, analyzer) pair has been changed. (a) (0,90) (b) (8,98) (c) (45,135) Intensity is the same for (a) and (b), scaled to show the interesting features; (c) has been scaled independently for its own features.

is observed. In (b), the angles are $(8°, 98°)$, and both (+1,0) and (1,-1) modes appear with roughly equal strengths. In (c), the angles are $(45°, 135°)$, and only the (+1,0) mode is observed. Note that at non-zero polar angles, the degeneracy between the +1 and -1 orders is broken, and, therefore, are not concurrently excited within our excitation angular bandwidth. In these images, consequently, lobes from SPPs extend in only one direction as opposed to the two in Fig. 2. The relative strength of the coupling is obviously quite different, in agreement with what is inferred from the spectral data. Simultaneous excitation of (+1,0) GM and (-1,0) AM modes has also been observed (data not shown) at $ak_{//}/2\pi = 0.8$ and $ak_{//}/2\pi = 0.2$. This appears as a single horizontal stripe with different relative amplitudes in the left and right directions in the corresponding optical image. For reference, the dispersion diagram is again displayed, with the approximate overlapping illumination function, in Fig. V.8.

V.C.2 Imaging SPPs on thick aluminum films

Imaging of modes on the sample STB (“thick” aluminum films) is shown in Fig. V.9. These images were acquired with broadband ASE source ($\lambda = 1520 - 1570nm$), which reduces some of the imaging artifacts as compared to a highly coherent source. This Fig. will be described more completely in the next draft.

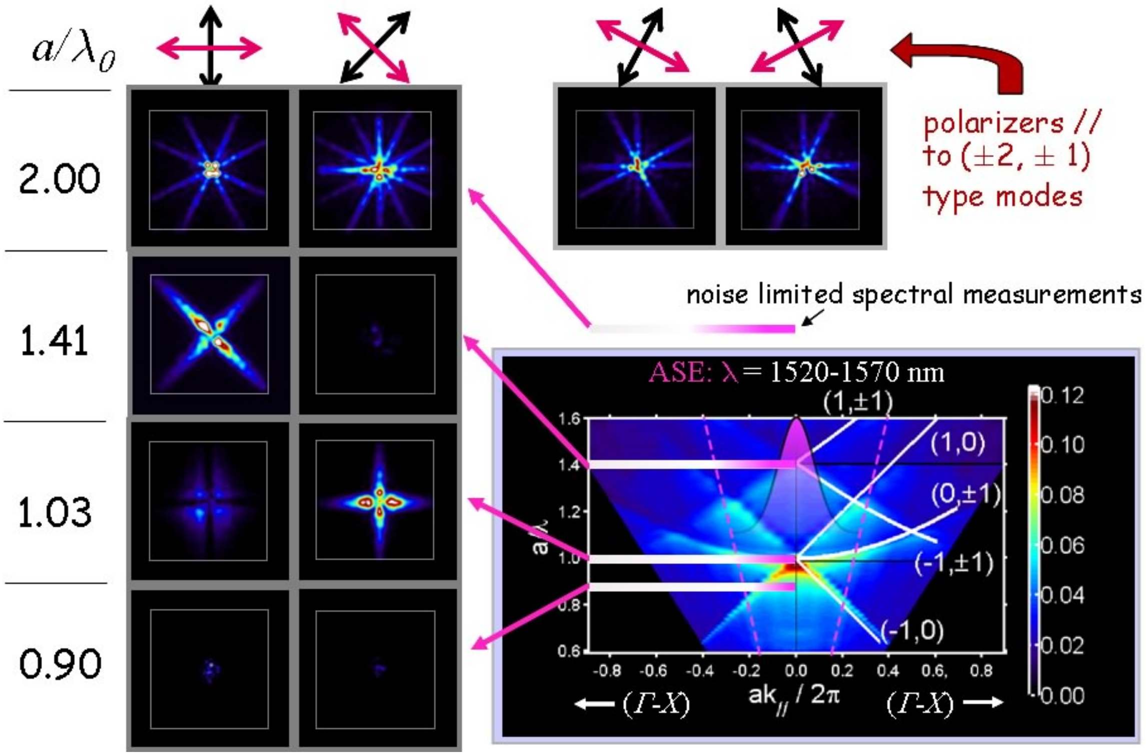

Figure V.9: SPP modes on an aluminium metallic hole array.

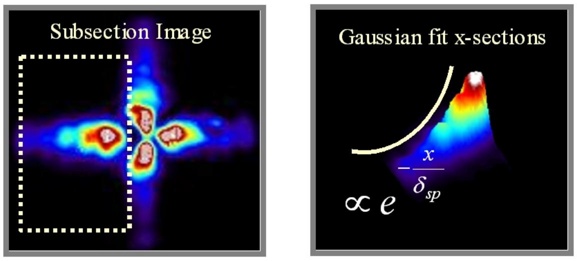

(a) (b)

Figure V.10: SPP decay fitting procedure. (a) Typical SPP image is subsectioned appropriately for a particular propagating mode. (b) Subsection is averaged and fit with exponential decaying function

V.D SPP propagation lengths

V.D.1 SPP propagation length fitting procedure

We implement some simple image processing procedures in order to determine decay lengths for various SPP propagating modes. The typical implementation is illustrated in Fig. V.10. A basic image with four propagating (1,0) type modes is shown in Fig. V.10(a). Each of these frames are sub-sectioned over each one of the four modes in turn, fitting an exponential curve to a Gaussian fit of the image cross-sections and averaging over each of the directions.

V.D.2 STA grating propagation lengths

For a wavelength of 1.31 μm, we measure a 1/e decay length of 22 3 and 15 2 μm for the (+2,0) and (1, 1) modes, respectively. Similarly, the (1, 1) mode at 1.52 μm decays in 26 3 μm, while the (1,0) mode at 1.57 μm propagates 14 3 μm. This data may be compared to the estimated decay value for an unperforated, infinite AM interface of 140 μm (at 1.31 μm) or 200 μm (at 1.55 μm)- or, perhaps more appropriately, with the antisymmetric SPP mode of a finite thickness gold film which predicts 23 and 32 μm, respectively, for the same wavelengths. These results are summarized in Fig. V.11, and are only marginally less than the 40 μmseen for a planar gold surface[77] at a 0.8μm wavelength despite the relatively strong

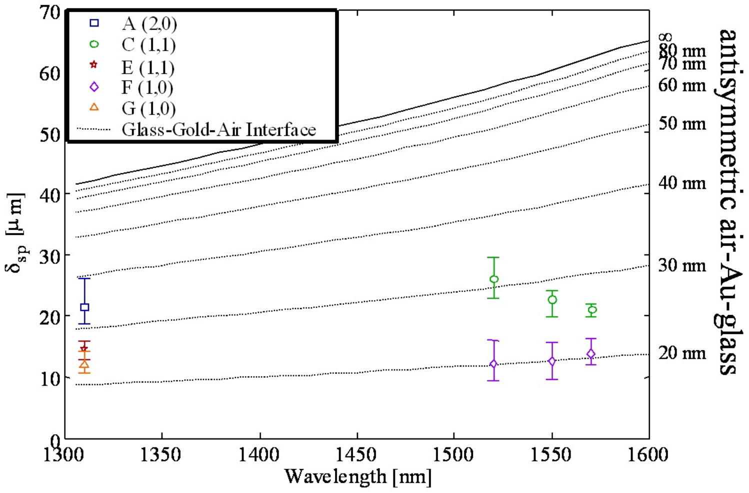

Figure V.11: Decay lengths for SPP on a gold film on glass.

radiative damping.

V.D.3 STB propagation lengths: currogated and planar surface

By utilizing (at least) two directions of our propagating modes, it is possible to excite SPP waves that encounter different surface structures. One example of this is shown in Fig V.12(a). In the horizontal direction near the bottom of the image, there is a continuous hole array as per usual. In the vertical direction, however, the metallic film is mostly continuous, interrupted at different spacing by two rows of holes. These “speedbumps” couple out a small amount of the SPP wave in this direction, and thus sample the propagation characteristics of the mode propagating along this planar interface. In this manner, we are able to determine both the radiative decay (coupling strength) from the grating array, as well as separate the material damping component of the propagation by measuring these two fields simultaneously in one image acquisition.

The total propagation length in the nanohole array is given by:

$$\frac{1}{\delta_{spp}^{tot}} = \frac{1}{\delta_{spp}^{mat}} + \frac{1}{\delta_{spp}^{rad}} \tag{V.1}$$

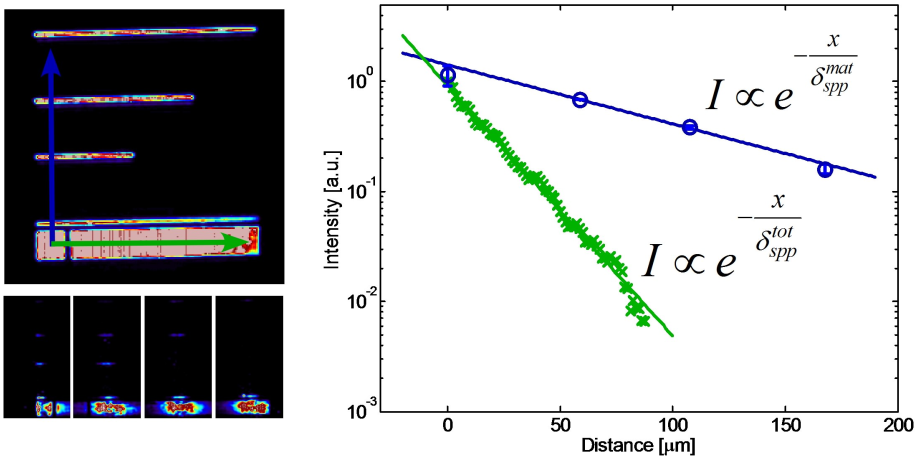

(a) (b)

Figure V.12: Decay lengths aluminum-air interface, with grating coupling and pure material absorption

where the total SPP propagation length $\delta_{spp}^{tot} = 20 \pm 5\ \mu m$, the material damping length $\delta_{spp}^{mat} = 80 \pm 5\ \mu m$; from these values we calculate a radiative damping rate of $\delta_{spp}^{tot} \approx 27\ \mu m$. This is the most direct measurement of this parameter to date. It allows simultaneous measurement of both the planar and corrugated surface propagation lengths.

At this point we will further extend the imaging techniques advanced in this chapter and utilize ultrafast optical pulses for the excitation field. By also including a reference pulse in an interferometric arrangement, we are able to study both the amplitude and spatial phase of propagating SPPs on femtosecond time scales.

The text of Chapter Five in part is a reprint of the material as it appears in the following publication:

- Tetz K., Rokitski R., Nezhad M. and Fainman Y. "Excitation and Direct Imaging of Surface Plasmon Polariton Modes in a Two-dimensional Grating". *Applied Physics Letters*, vol. 86, no.11 2005.

The dissertation author was the primary researcher and author. The co-authors listed in these publications directed and supervised the research which forms the basis for this chapter.

VI

Spatiotemporal studies

Most of the time-resolved studies of SPPs [79, 80, 81] have focused on space-averaged characteristics of light reflected from or transmitted through corrugated metallic surfaces, while a few efforts [82, 83] have investigated propagation of femtosecond pulses along the metal surface. Comprehensive investigation of SPP evolution along the propagation direction was beyond experimental capability. Many potential applications of SPPs for information transmission, processing and detection, however, would require complete understanding of the in-plane SPP pulse propagation. This requires experimental characterization of SPP amplitude and phase evolution upon propagation, which presents an unexplored challenge on the way to building practical plasmonic devices for future information technologies.

VI..4 Excitation of surface plasmon modes in nano-structured metallic films

In this chapter we investigate the excitation and propagation of femtosecond SPP pulses using a time-resolved spatial heterodyne imaging (TRSHI) technique to obtain spatial distributions of the electromagnetic field amplitude and phase versus time. This type of dynamic 3-dimensional characterization of the surface electromagnetic field can provide invaluable insight on SPP excita-

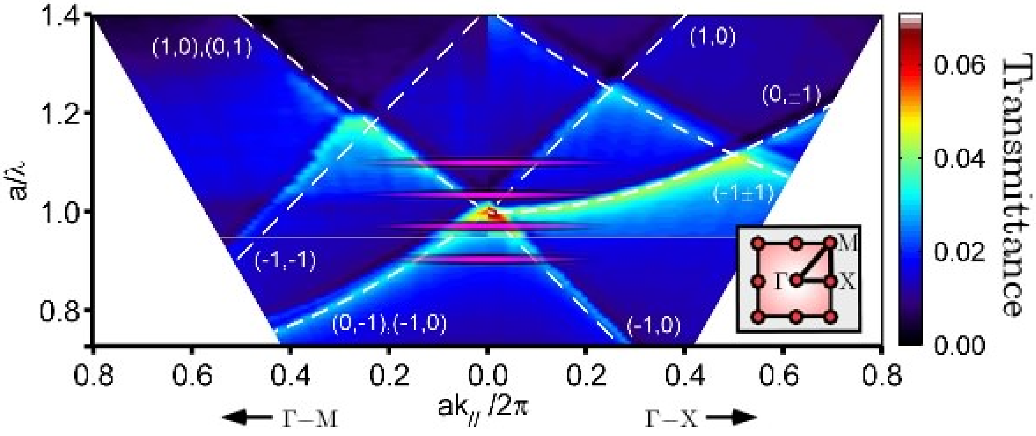

Figure VI.1: Measured transmittance of nanohole arrays, superimposed with calculated dispersion map of SPP modes. The pink ellipses represent illumination from femtosecond source with an N.A. of 0.25 (10x MO). Four different period to center wavelength ratios, 0.91, 0.97 1.04 and 1.10 are investigated here by using arrays with different periods and fixing the laser frequency.

tion and propagation along the surface of the film. The method has successfully been applied in various research areas ranging from fiber optics to plasma physics [84, 85].

In our experiment the optical field is coupled into and out of the metallic film using a single array of nanoholes etched in the metallic film in the manner described in Chapter V. We observe excitation and scattering of femtosecond SPP pulses in a 100 nm-thick aluminum films, deposited on a GaAs substrate and perforated with an array of circular nanoholes. The holes with diameter 350 nm are distributed uniformly on the square grid with total array size 200 × 200 μm. Results are presented for arrays with hole periods $a = 1.4$, 1.5, 1.6 and 1.7 μm.

We display the SPP dispersion for the four different arrays in Fig. VI.1 with the stitching between two spectral data sets occurring at the horizontal, solid white line. Phase matching conditions are displayed for a SPP on an air/aluminum interface with dashed white lines. Pink ellipses represent incident femtosecond pulse for the two arrays under study: in frequency limited by the pulse spectral bandwidth and in wave-vector by the angular intensity distribution of the illumination beam. The interplay between the spectral and angular bandwidth of the incident optical pulse is similar to the phase matching effects observed in volume holography and nonlinear optics. For our samples, only SPP modes on the metal/air interface are efficiently excited; the first order modes for the semiconductor/air interface occur at much lower frequencies, and the higher order modes that occur at these frequencies are not discernable in our measurements.

VI.A Imaging of propagating ultrashort surface plasmon polariton pulses

VI.A.1 Experimental setup and data acquisition

Time-resolved imaging of SPP modes is performed using a modified Mach-Zehnder interferometer shown in Fig. VI.2a. Optical pulses with central wavelength 1540 nm and temporal width FWHM $\simeq$ 200 fs are derived from a mode-locked laser (Coherent's Mira-900F with an OPO) and focused in the center of the nanohole array with microscope objective of 5,10, or 20x power (0.12 0.25 or 0.40 N.A.) through the substrate at normal incidence angle (Fig. VI.2b). The sample is placed between two crossed polarizers- blocking light transmitted directly through the film at the excitation point. The polarizer/analyzer pair is oriented at 45 degrees with respect to the array axes providing polarization projection of the incident optical field in the direction of the SPP polarization [86].

VI.A.2 General principle

Characterization of spatial amplitude and phase distribution in TRSHI is performed similar to the direct spatial reconstruction of optical phase approach [87]. An unknown optical wave $E_s(\mathbf{r}, t)$ is mixed with a reference optical wave $E_r(\mathbf{r}, t)$ having known spatial and temporal characteristics and their interference is detected and analyzed. This approach, derived from off-axis holography has been

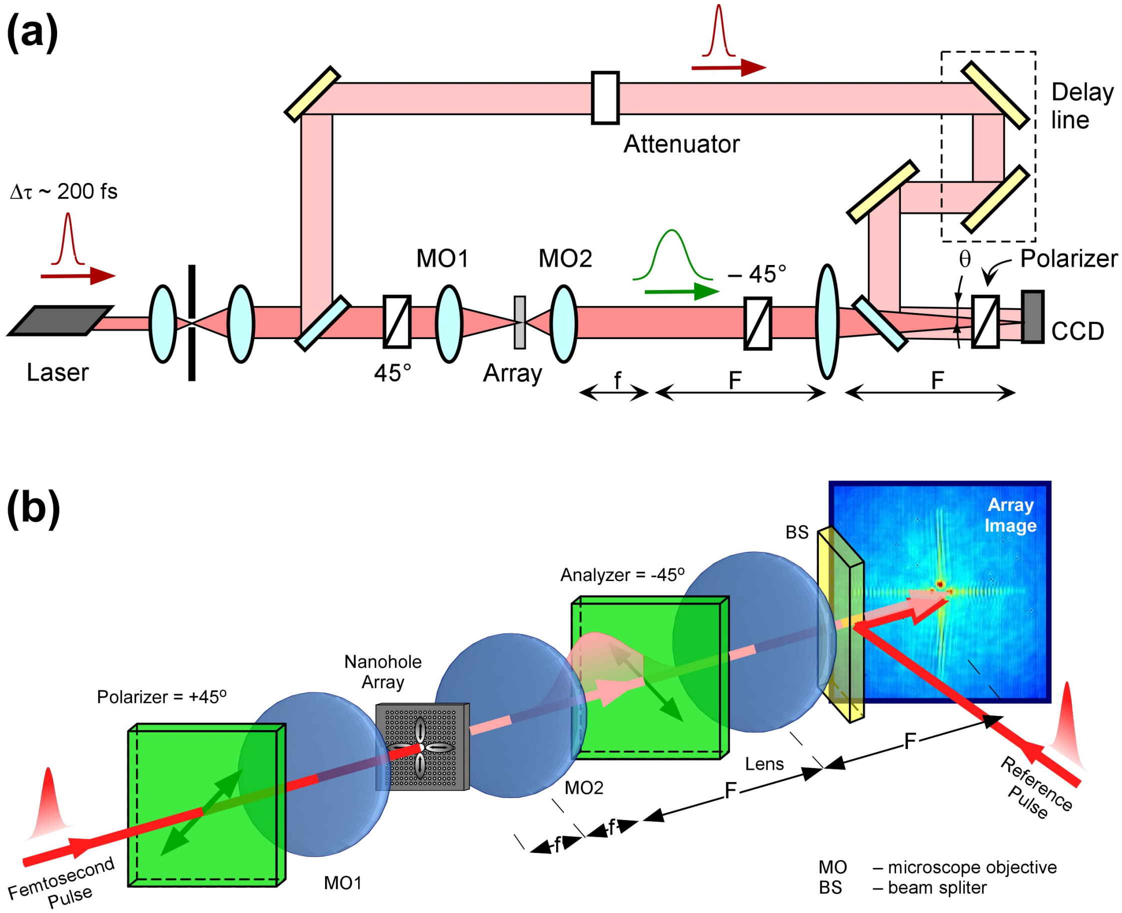

Figure VI.2: (a) Experimental setup for excitation and time-resolved imaging of femtosecond surface plasmon polariton pulses. (b) Sample illumination and imaging of scattered SPP pulses.

successfully used for precise profilometry [88]. Analysis of such interferograms with spatial carrier frequency was extensively analysed in the spatial frequency domain [89, 90, 91, 92] for coherent and stationary optical fields. Originally proposed by Takeda [93] the method is usually called Fourier Transform Method of fringe pattern analysis. Later modifications [94] of the method utilized slow temporal modulation of the optical field, introducing into the fringe pattern temporal carrier carrier in addition to spatial carrier.

TRSHI introduces reduced temporal coherence into the signal and the reference optical fields. Spatial coherence is assumed to be infinite, which is valid only in the case of "photon-like" polaritons. Temporal resolution is achieved by varying the delay between the interfering waves. We assume that the real electric field of both waves can be expressed in general case as

$$\begin{aligned} E_s(\mathbf{r},t) &= Re\left\{\frac{1}{2}\mathcal{E}_1(\mathbf{r},t)e^{j\phi_1(\mathbf{r},t)}e^{-j[\omega_l t-\mathbf{k}_1\cdot\mathbf{r}]}\right\}, \\ E_r(\mathbf{r},t) &= Re\left\{\frac{1}{2}\mathcal{E}_2(\mathbf{r},t)e^{j\phi_2(\mathbf{r},t)}e^{-j[\omega_l t-\mathbf{k}_2\cdot\mathbf{r}]}\right\}, \end{aligned} \tag{VI.1}$$

where we assume that both waves propagate in free space with wave vectors $\mathbf{k}_1$ and $\mathbf{k}_2$ and the same linear polarization.

In our notation $\mathcal{E}_1(\mathbf{r},t)$ and $\mathcal{E}_2(\mathbf{r},t)$ represent time and space varying real amplitudes of the signal and the reference optical waveforms and $\phi_1(\mathbf{r},t), \phi_2(\mathbf{r},t)$ – their phases, containing quadratic and higher order terms. This notation implies that the electromagnetic fields are expanded into a Taylor series around their temporal central frequency ω_l and spatial central frequencies $\mathbf{k}_1$ and $\mathbf{k}_2$.

The validity of such expansion becomes questionable when the temporal or the spatial bandwidth of the electromagnetic waves approaches their corresponding central frequency. Here we assume sufficiently narrowband electromagnetic waves (both in space and time) to justify the Taylor expansion. Additionally we assume, that the temporal and spatial characteristics of the reference field are known and its phase is constant: $\phi_2(\mathbf{r},t) = \phi_0$, corresponding to plane wave in space (collimated beam) and transform-limited pulse in time. The signal field has unknown, but slowly varying temporal and spatial distributions of amplitude $\mathcal{E}_1(\mathbf{r}, t)$ and phase $\phi_1(\mathbf{r}, t)$. The instantaneous intensity of the optical field incident on the CCD surface is written as a sum of the fields $E_s(\mathbf{r}, t)$ and $E_r(\mathbf{r}, t)$:

$$\begin{aligned} I(x, y, t) &= |E_s(x, y, t) + E_r(x, y, t)|^2 = && \text{(VI.2)} \\ & \mathcal{E}_1^2(x, y, t) + \mathcal{E}_2^2(x, y, t) + && \\ & 2\mathcal{E}_1(x, y, t)\mathcal{E}_2(x, y, t)\cos[\Delta\mathbf{k}\cdot\mathbf{r} + \phi_1(\mathbf{r}, t)], && \text{(VI.3)} \end{aligned}$$

where we omitted constant phase factor ϕ_0 and $\Delta\mathbf{k} = \mathbf{k}_2 - \mathbf{k}_1$ represents spatial carrier frequency. This optical intensity is transformed into spatial distribution of electrical charge by the detector array. During this conversion process intensity is averaged in time by slow photodetector response, sampled in space by the array and averaged in space over the pixel area.

The end result of the photoelectric conversion procedure is spatially sampled distribution of electric charge, proportional (at the sampling grid locations) to temporally and spatially averaged incident optical intensity. At first we will describe temporal gating of the signal field by the reference pulse ignoring spatial sampling and averaging effects.

For a signal wave nominally at normal incidence, and the reference pulse propagating in the XZ plane at the angle θ with respect to the CCD normal, the spatial distribution of electric charge in the CCD plane at time t can be described as:

$$\begin{aligned} q(x, y, t, \tau) \sim & \int_{t-T}^{t} \left\{\mathcal{E}_1^2(x, y, t') + \mathcal{E}_2^2(x, y, t' + \tau)\right\} dt' + \qquad \text{(VI.4)} \\ & 2\int_{t-T}^{t} \mathcal{E}_1(x, y, t')\mathcal{E}_2(x, y, t' + \tau)\cos[\omega_l\tau + k_l x\sin\theta + \phi_1(x, y, t')]dt', \end{aligned}$$

where $k_l = 2\pi c/\lambda_l$, T is the detector integration time and τ represents temporal delay of the reference pulse $E_r(x, y, t)$ with respect to the common reference time.

The first integral in the expression VI.4 represents spatial background, equal to the sum of intensities of the reference and the signal fields alone. The second integral describes a cross-interference term, containing the amplitude and phase of the unknown field. This term vanishes when two interfering fields do not overlap in time (product of the amplitudes is equal to 0) or temporal variation of phase $\phi_1(x, y, t')$ averages out the integral. In the case of interference between two short pulses the interference is created by the portion of the signal wave enclosed by the dashed lines, because the reference pulse travels as some angle and sweeps the CCD surface with time.

Similar to spatial heterodyne holography approach, amplitude and phase is obtained by isolation of the interference term and spatial demodulation – bringing it from the spatial heterodyne frequency to baseband. This procedure can be performed either in space by linear phase multiplication and lowpass filtering or in the spatial frequency domain by bandpass filtering and spectral shift. With infinite dynamic range (when the procedure is performed in a computer with high numerical precision) the two approaches are equivalent. We will illustrate it and analyze in the Fourier domain, where representation of the spatial bandwidth and resolution is more intuitive.

The spatial spectrum of the single sidelobe of the cross interference term is described by

$$\tilde{q}_{12}(f_x, t, \tau) \sim \mathcal{F}\left\{\int_{t-T}^{t} \mathcal{E}_1(x, t')\mathcal{E}_2(x, t' + \tau)e^{j\omega_l\tau + jxf_{0x} + j\phi_1(x,t')}dt'\right\}, \qquad \text{(VI.5)}$$

where $\mathcal{F}$ represents spatial Fourier transform and we introduced $f_{0x} = k_l \sin\theta$ to represent spatial carrier frequency in f_x direction. After simple regrouping this expression can be written as

$$\tilde{q}_{12}(f_x, t, \tau) \sim e^{j\omega_l\tau}\mathcal{F}\left\{\int_{t-T}^{t} \mathcal{E}_1(x, t')e^{j\phi_1(x,t')}\mathcal{E}_2(x, t' + \tau)e^{jf_{0x}x}dt'\right\}. \qquad \text{(VI.6)}$$

The spectral shift of the spatial spectrum $\tilde{q}_{12}(f_x, t, \tau)$ by $-f_{x0}$ cancels out the linear phase term in the space domain and leads to the final expression for the isolated cross-interference term in the space domain:

$$q_{12}(x, t, \tau) \sim e^{j\omega_l\tau} \int_{t-T}^{t} \mathcal{E}_1(x, t')e^{j\phi_1(x,t')}\mathcal{E}_2(x, t' + \tau)dt'. \qquad \text{(VI.7)}$$

For CCD integration times much longer than the temporal duration of the reference and signal waveforms this expression represents a temporal *field* cross-correlation with a fixed linear phase term $e^{j\omega_l\tau}$. When the reference waveform is much shorter in time than the signal and is constant in space (plane wave approximation), the spatial amplitude and phase distribution of $q_{12}(x,\tau)$ can be used as an estimate of $\mathcal{E}_1(x,\tau)e^{j\phi_1(x,\tau)}$.

VI.B Experimental Results

The SPP field, scattered from the other side of the nanohole array, is collected with a 20x microscope objective and imaged with a $4f$ optical arrangement onto the surface of InGaAs digital camera. The nanohole array is imaged with 40 times magnification on on CCD surface, where the optical field, radiated by propagating SPP pulse forms interference with a superimposed femtosecond reference pulse.

Temporal gating of the collected optical field is performed using a time-resolved spatial heterodyne imaging technique. The reference optical pulse, derived from the same laser, is combined with the scattered femtosecond SPP pulse on the surface of the CCD in holographic recording configuration and the resulting interference pattern is measured as a function of relative delay between the scattered SPP and reference fields. We process each measured interference pattern to obtain spatial amplitude and phase distributions for each position of the delay.

In the presence of a short time-gating optical pulse the camera detects interference between the scattered femtosecond SPP pulse and the reference pulse when they overlap in time and space. A typical interference pattern observed for ∼0.5 ps delay between the signal and the reference is shown in Fig. VI.3(a) in the array image plane. Vertical interference fringes demonstrate that the spatial heterodyne frequency is oriented horizontally, along the k_x direction. Spatial spectrum of the interference pattern, shown in Fig. VI.3(b) features only single spatial

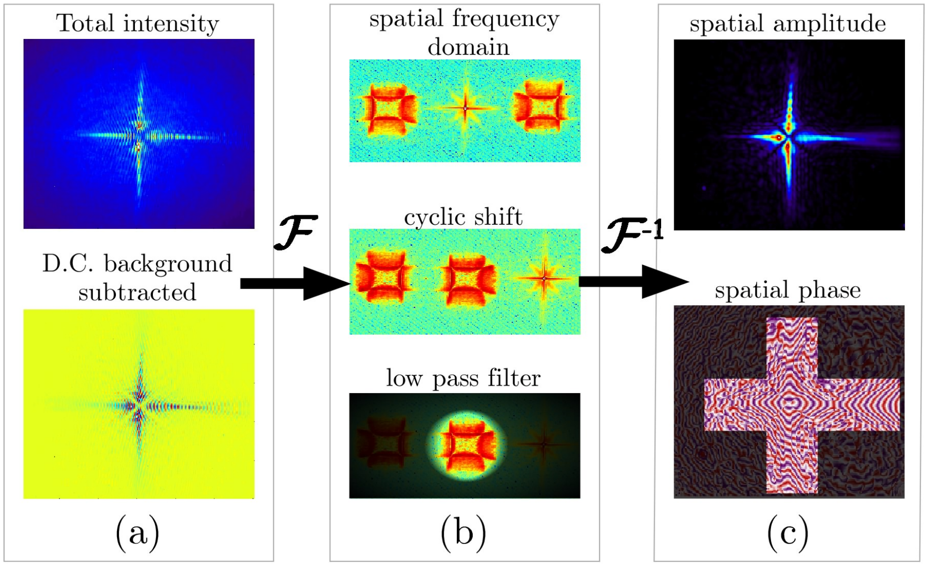

Figure VI.3: (a) Spatial domain: total intensity and subtracted D.C background at some delay τ (b) FFT to spatial frequency domain: shift signal to baseband and filter (shown in logarithmic color scale). (c) Inverse FFT to obtain spatial amplitude and phase of the reconstructed SPP field.

harmonic signal since the interference pattern is obtained with a single photon absorption process.

Horizontal orientation of the spatial heterodyne frequency provides suboptimal spatial resolution; however, this configuration greatly simplifies time-space unshearing of the measured data. Since the interference is observed only when the signal and the reference fields overlap in time, scanning of the delay between the scattered SPP and the reference field allows tracking the evolution of the SPP field with time. Processing the measured interference pattern yields an estimated scattered SPP pulse field, shown in Fig. VI.3(c). The measured signal corresponds to a temporal optical field cross-correlation of the SPP waveform with the reference short pulse waveform. The reconstructed field amplitude in Fig. VI.3(c) is clearly asymmetric in the horizontal direction, since the time-resolved spatial heterodyne data is intrinsically sheared in the direction of the spatial carrier frequency.

Space-time shearing of the interference pattern originates from the tilt between the interfering fields. The interference is observed only when the signal

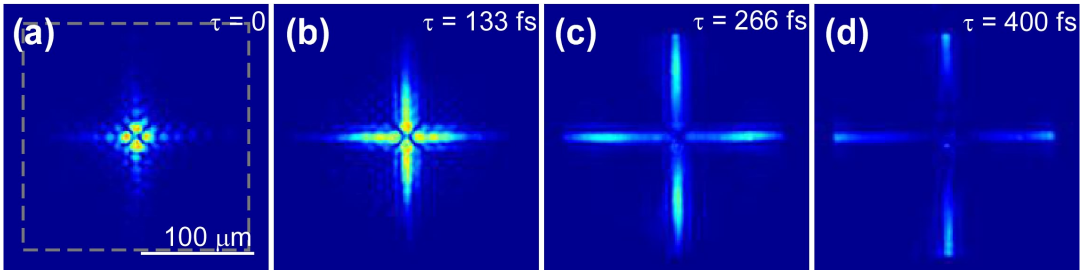

Figure VI.4: Spatial amplitude distributions of scattered SPP field excited and imaged by the nanohole array with hole period $a = 1.6$ μm at different relative delays. SPP excitation is performed by the optical beam focused by 5x MO lens.

and the reference fields overlap in space and time on the camera's surface, and the reference pulse has a finite envelope that is scanned across the detector surface at a rate that depends on spatial heterodyne angle. For a known spatial heterodyne angle the shear can be inverted using a 2D affine transform along the direction of the shear.

While shearing inversion is a linear operation and can be easily executed for the field amplitude, spatial phase information can not be easily unsheared due to $n2\pi$ ambiguity in the reconstructed phase magnitude. Correct implementation of the shear inversion in the spatial phase data includes 3D unwrapping of the phase in the space-delay coordinates with the subsequent affine transform. In this dissertation we present sheared spatial phase information without such processing. As a result our spatial phase data has additional linear phase slope in the horizontal direction.

VI.B.1 Spatial amplitude and phase distributions

The images shown in Fig. VI.4(a-d) represent spatial amplitude distributions and phase at 4 different delays between the interfering fields: = 0, 133, 266 and 400 fs for the sample with array period 1.6 μm and 5x illumination objective. All the measured data frames are combined into a movie with 1 ps total duration and 3 fs frame separation. In the movie we observe in real time how four SPP short pulses are first excited in the center and then propagate towards the edges of

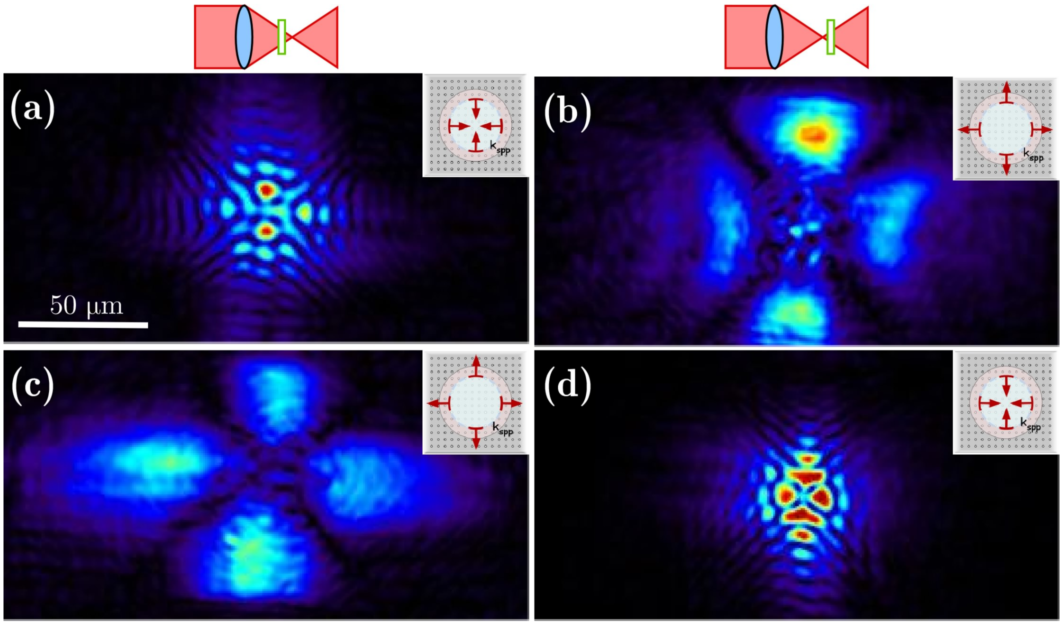

Figure VI.5: Modal interference in time-resolved SPP imaging. (a) converging illumination, $a/\lambda = 1.10$. (a) diverging illumination, $a/\lambda = 1.10$. (a) converging illumination, $a/\lambda = 0.91$. (a) diverging illumination, $a/\lambda = 0.91$. Modal interference is observed in (a) and (d) where distinct, spatially overlapping modes exist.

the array. Since the SPP pulses experience attenuation, their intensity significantly reduces upon propagation.

A close look at the spatial amplitude distributions at short time delays (Fig. VI.4a,b) reveals significant spatial amplitude modulation of the field, which is absent at longer time delays (Fig. VI.4c,d). We attribute this amplitude modulation to spatial interference of four femtosecond SPP pulses, propagating towards the center of the SPP excitation region. At the short time delays four excited SPP pulses overlap spatially and temporally in the center of the array. Their fields sum up coherently with appropriate phases to form the observed SPP modal interference pattern. At longer delays the pulses pass through the center, separate spatially, and no interference is observed.

A more complete picture of the modal interference is illustrated in Fig. VI.5 at equivalent fixed delay positions. Four images are shown for, for two different array periods and two different illumination conditions. (a) and (b) are with an array

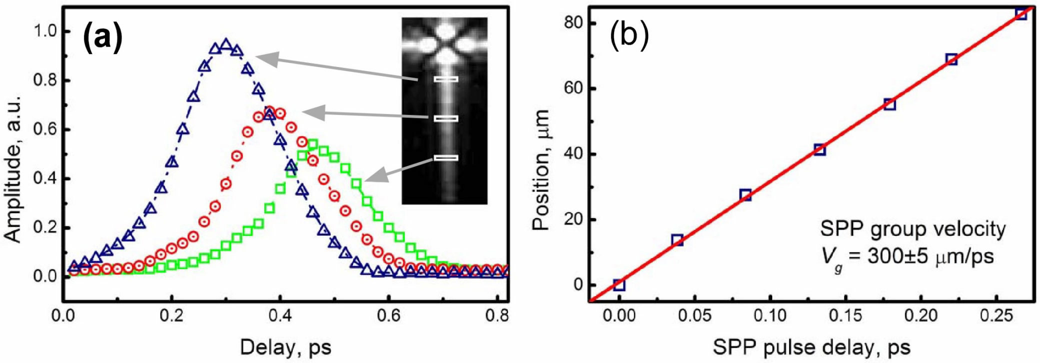

Figure VI.6: (a) Normalized temporal cross-correlation of scattered SPP and reference pulses, measured at three spatial locations along SPP propagation path. (b) delay of the SPP pulse peak measured at different positions along the propagation path gives SPP pulse group velocity $\sim 300 \pm 5$ μm/ps.

that gives $a/\lambda = 1.10$, which excites "+" or forward order SPP waves, while (c) and (d) are with $a/\lambda = 0.91$ which excites "-" or backward order SPPs. The sample is fixed and the illumination MO (20x) is adjusted to position the beam waist approximately 16μmeither in front of (left side (a) and (c)) or behind (right side (b) and (d)) the sample position. For the "+" order, when the beam is converging (a), the four SPP modes are excited at different points in space, but continue to converge in the sample plane. As they do, they pass through each other and create the modal interference pattern observed. For diverging illumination (b), the SPPs continue to propagate outward and do not overlap in space, and therefore no interference pattern is observed. These situations are sketched in the insets to each of these images. For the "-" orders, the opposite situation occurs. For converging illumination (c), the modes do not overlap in space after excitation; for diverging illumination (d), they propagate back towards each other and similar modal interference is observed.

VI.B.2 Group velocity and dampening factor measurements

The temporal evolution is characterized by measuring the cross-correlation of the scattered SPP and reference optical fields at different spatial locations along the propagation path. The results of this measurement are shown in Fig. VI.6a for three spatial locations separated by 25 μm. The peak amplitude of the SPP pulse decays exponentially while the waveform maintains nearly the same shape.

From the decay of the waveform peak amplitude we estimate the decay coefficient for the scattered field amplitude $\kappa \sim 45\ \mu\mathrm{m}^{-1}$, which agrees well with $\delta_{spp} \sim 20\ \mu\mathrm{m}^{-1}$ obtained for the optical intensity from the time-average intensity distributions and the data obtained with CW illumination [95, 96]. This attenuation coefficient has the contribution of both radiative loss due to SPP scattering off the grating and material absorption as detailed in Chapter V.

The ratio of the spatial location over the waveform delay gives an estimate of SPP pulse group velocity ~300 μm/ps- which is equal to speed of light in vacuum within the accuracy of our experiment and agrees with the fact that the observed SPP mode propagates along metal/air interface with the evanescent electromagnetic field concentrated in the air.

While in Fig. VI.6(b) we present the data only for the scattered field, propagating upwards from the excitation point, we performed the same measurements with the SPP pulse propagating down from the excitation point. We found that vertical tilt of the nanohole array with respect to the optical axis of the setup results in the difference of the measured propagation velocity for the SPP pulses propagating in the opposite directions. The results, presented in Fig. VI.6 correspond to the array alignment with minimal vertical tilt, inferred from the group velocity difference between the up and down propagating pulses.

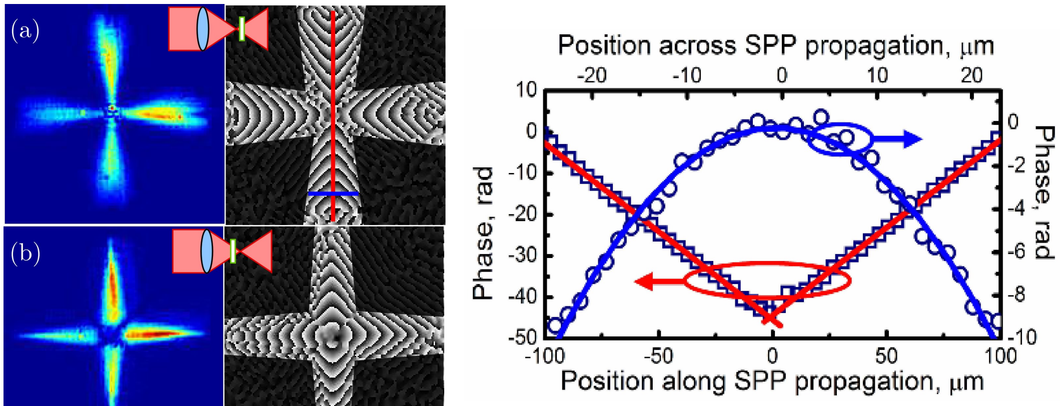

(c)

Figure VI.7: Spatial amplitude and phase distributions of the scattered SPP field obtained with diverging (a), and converging (b) beam illumination for $a/\lambda = 1.4$. (c) Unwrapped phase cross-sections of the data in (a) both along (linear phase) and across (quadratic phase) the SPP propagation direction.

VI.B.3 Spatial phase of the scattered SPP pulses

Spatial phase information of the propagating femtosecond SPP field was also investigated, and results for one array with hole period $a = 1.4$ μm, supporting (-1,0), (0,-1) and (1,0), (0,1) SPP modes with our illumination conditions, as indicated in the phase matching diagram in Fig. VI.1. Nanohole arrays were illuminated with converging and diverging Gaussian beams using a 10x microscope objective. The incident optical beam was centered at the array center.

Measured spatial amplitude and phase distributions are presented in Fig. VI.7 for a fixed delay between the scattered SPP field and the reference femtosecond pulse. The spatial amplitude distributions of the scattered SPP field show that when the nanohole arrays are illuminated with a converging Gaussian beam, the excited surface field continues converging and focuses - as seen in Fig. VI.7(b). The focusing of the SPP beam achieved in this configuration is much tighter than shown in Fig. VI.4 due to larger spatial bandwidth of the incident beam, achieved by 10x MO lens.

The opposite effect is observed when the arrays are illuminated with diverging Gaussian beams – the surface field diverges within the metal surface from

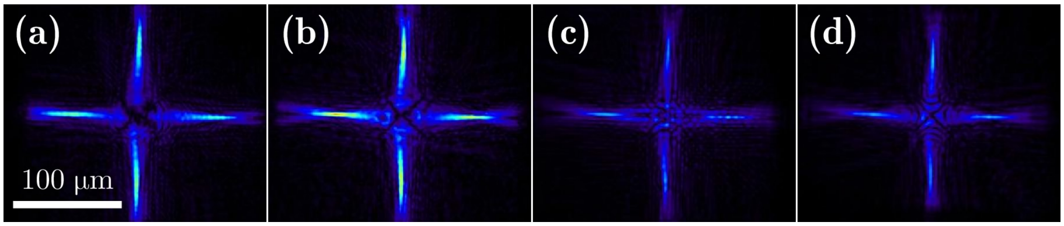

Figure VI.8: Focusing of various SPP orders, measured with converging beam excitation. Period to wavelength ratios a/λ are (a) 0.91 (b) 0.97 (c) 1.04 (d) 1.10

the illumination point, as shown in VI.7(a), and the amplitude decays accordingly.

Spatial phase distributions in Fig. VI.7 show several characteristic features of the scattered SPP fields. For all nanohole arrays vertical cross-section of the spatial phase profile shows linear phase variation along SPP propagation path up and down from the excitation point (see Fig. VI.7c). The amount of this linear phase directly corresponds to the incidence angle of the free space optical wave most efficiently coupled with SPP.

As expected, the magnitude of the linear phase is the same for both converging and diverging beam illumination and corresponds to the radiation angles of ∼6.4 and ∼1.2 degrees for arrays with 1.4 and 1.6 μm nanohole periods, respectively. These measured values are consistent with the expected phase matching angles 6.0 and 1.9 degrees, observed in the Fig. VI.1 at the overlap regions of pink ellipses, corresponding to the spatio-temporal bandwidth of the focused short pulse, and dashed white lines, indicating phase matching angles for SPP excitation.

Transversal phase distributions for both arrays demonstrate close to quadratic profiles (see Fig. VI.7c), implying converging and diverging propagation of the surface field, however the signs of the quadratic phase are opposite for the two illumination conditions.

VI.B.4 SPP focusing

Focusing of SPPs excited with different orders are shown in Fig. VI.8 for equal, fixed time delays. In all cases, the SPPs propagate out from the excitation point and converge towards a waist. The different coupling orders lead to different modal distributions, however, and the +orders have well defined interference patterns as noted previously.

To visualize propagation of the femtosecond pulse through the waist of the focused surface field we excite an SPP field on the edge of the array and measure its propagation for a distance of 200 μm is shown in Fig. VI.9. The time-average amplitude of the observed field was rescaled in Fig. VI.9(b) at each position along the propagation path (in the horizontal direction) to compensate for longitudinal attenuation and clearly show transversal spatial transformation of the surface field. The spatial phase distributions for three different focusing SPPs is shown in Fig. VI.9(c-e). While scattered +order SPP modes have positive wavefront curvature (see Fig. VI.9e), normal for Gaussian beams in free space, the field of scattered -order SPP modes demonstrates in Fig. VI.9c negative curvature of the spatial phase front with respect to the waist of the focused SPP.

The counterintuitive phase behavior for the -order SPP modes can be understood by looking at the phase matching conditions for SPP excitation. The negative sign in the notation of these SPP modes indicates the projection of the incident wave vector opposite to the SPP wave vector yielding a backward leaky wave. The wavefront of the SPP is reversed with respect to the incident wave and the propagation direction of the excited SPP field is opposite to the direction of the incident optical wave.

The measured width of the SPP waist of $2w_0 \sim 4\mu$m is limited by the diffraction limit of our imaging system. At higher frequencies, where the SPP wavevector is significantly larger that that of the free-space photon, it is then possible to obtain spot sizes that are sub-diffraction limit, which may be of interest in high-resolution surface microscopy applications.

The text of Chapter Six in part is a reprint of the material as it appears in the following publication:

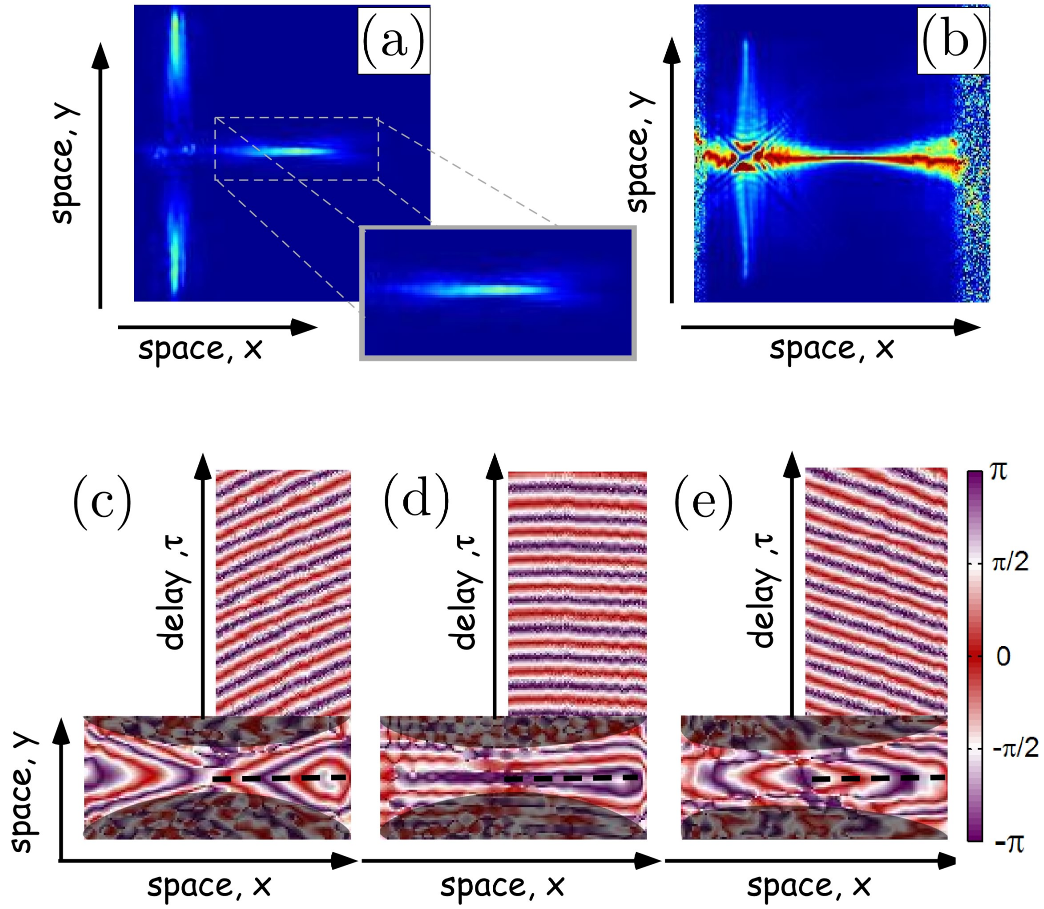

Figure VI.9: (a) Representative spatial amplitude for a fixed time delay, with zoomed view of beam waist. (b) Renormalized (along y- at each x- position), time averaged view of showing SPP focusing. (c-e) (lower) Spatial phase near the beam waist at fixed time delays for a/λ of (c) 0.97 (b) 1.04 (c) 1.10. Also shown in (c-e) (upper) are phase distributions for the scattered field in the $x\tau$ plane, clearly showing the leaky backward, normal, and forward scattered plane wave distributions.

- Rokitski R.†, Tetz K.† and Fainman Y. “Propagation of Femtosecond Surface Plasmon Polariton Pulses on the Surface of a Nanostructured Metallic Film: Space-Time Complex Amplitude Characterization”, Physical Review Letters, 95, 177401, 2005.

The dissertation author was the primary researcher and author. The co-authors listed in these publications directed and supervised the research which forms the basis for this chapter.

VII

SPR Sensor

In this chapter we investigate the use of metallic nanohole transmission in sensing applications. We demonstrate a surface plasmon resonance (SPR) sensor based on the nanohole array presented in previous chapters, and specifically show polarization properties that facilitate narrowing the transmission linewidth (and hence maximize resolution) while operating in a regime that facilitates high SBP imaging.

A high spectral resolution, 2-D nanohole array based surface plasmon resonance sensor that operates at normal or near normal incidence- facilitating high spatial resolution imaging- is presented. As we described in Chapter IV, particularly Sec. IV.C.3, the angular and spectral transmittance of the structure is modified from a Fano-type to a pure Lorentzian lineshape with a parallel and orthogonal polarizer-analyzer pair. This change leads to a linewidth narrowing that maximizes the sensor resolution, which we show to be of $O(10^{-5})$ RIU. We estimate the potential of this system of $O(10^{-6})$ RIU under optimal conditions.

VII.A Traditional SPR configurations and limitations

One of the most successful, important, and demonstrated applications of surface plasmon resonance has been for sensing applications. The first commercialized version of an SPR sensor appeared in the early 1990's, and the number of instruments in use in both commercial and academic research labs worldwide, from the leading supplier Biacore, is greater than 2500[1]. However, there are a number of limitations which may be addressed as a consequence of this work.

A schematic of a generic affinity binding type reaction is shown in Fig. VII.1(a). In general, the experimenter would like to know when two (or sometimes more) molecules of interest have become attached. However, as indicated, the molecule size is typically on the order of nm, while the wavelengths of light on the order of 100's or 1000's of nm for the lasers most commonly employed.

The most common method of optical readout of affinity binding reactions is with the use of fluorescent labels. In this method, a separate, fluorescent molecule that is attached to the molecule of interest. This method, employed in a number of techniques, has a number of drawbacks including:

- No Kinetics
- Difficulty in determining label binding chemistry
- Environment sensitive
- Shelf life is limited
- Bleaching

SPR sensors are advantageous for a number of reasons. As described in Chapter II, the SPP mode has a field that is localized at the interface between two media, and the effective wavelength is reduced. This makes this mode ideal

---

[1] see www.biacore.com

for detecting small perturbations in the effective index at the metal dielectric interface. In addition, since because of the field localization, the SPR sensor is most sensitive to the binding interaction and less to the background concentration in the channel. This is not the case in fluorescent readout techniques. Indeed, the background signal from any unbound fluorophores is overwhelming. This makes is necessary to wash the unbound molecules from the interrogation region with a buffer solution before any measurements may be made. This, of course, inhibits kinetic measurements as the observer only has access to the equilibrium binding concentration after the wash cycles. As a quick overview, we summarize the traditional advantages any SPR sensor:

1. **Real-time:** the kinetics of an interaction, i.e. the rates of complex formation (k_a) and dissociation (k_d), can be determined
2. **Label-free:** fluorescent label molecules are not needed- greatly simplifying
3. **Small volumes:** less analyte needed- a great advantage if
4. **Versatile:** applicable to a variety of interactions
5. **Multiple interactions:** complex formation can be monitored as each component is incorporated into a multimolecular complex.

These properties make SPR sensors advantageous in a number of applications. However, until very recently, they have been limited to only one or a few parallel channels. We discuss the nature of these limitations further in VII.A.1.

The main disadvantages are in sensitivity and specificity. Fluorescent methods may be quite sensitive in that one can simply integrate for a longer period of time and count photons. The specificity- that is the extent to which different molecules interact with a single partner immobilized on a sensor surface- is necessarily predicated on the choice of appropriate immobilization target, and the SPR signal cannot differentiate between different molecules. With fluorescent molecules one can analyze the signal of different species by multiplexing different color tags.

As mentioned, we are describing a sensor platform that may be used for any number of biochemical species, including but not limited to: peptides, antibodies, oligonucleotides, receptors, polypeptide/DNA arrays, receptor ligand assays, enzyme assays. Immobilization of oligos to a gold surface is used primarily in surface plasmon resonance technology where a gold-sulfur bond chemistry is dominant in this category. A commonly used coupling agent is 11-mercaptoundecanoic acid, where the thiol group on one end binds to gold and the carboxylic group on the other end is versatile for further attachment to derivatized oligonucleotides.

Another important parameter is biochemical sensing is the throughput. For just a very rough idea at some of the magnitudes involved, and why high throughput and parallelism is important, we take just a quick look at some of the numbers involved proteomics, where SPR technology has been useful, and will likely be important in the future of protein array technologies. The human proteome has $O(10^5)$ proteins. This translates to $O(10^{10})$ potentially interacting protein pairs (let alone multiple interacting proteins). Add in protein-DNA, and protein-non-protein molecules (e.g. small, synthetic drug molecules), and the complexity is truly staggering. For these reasons, there is a need for high quality interaction data on a large number of interactions simultaneously.

VII.A.1 Conventional SPR sensor configurations

A wide variety of SPR sensors have been demonstrated. The most common configurations employ the Kretschmann geometry or a shallow grating coupler and monitor the resonance shift (reflection minima) as a function of angle, wavelength, or simply as differential intensity [97]. The most common version, the Kretschmann geometry, is illustrated in Fig. VII.1b, which is identical to that shown in Fig. II.6, and discussed in Sec. II.C, where the phasematching conditions are further illustrated in Fig. II.7. The surface is treated with a specific biomolecu-

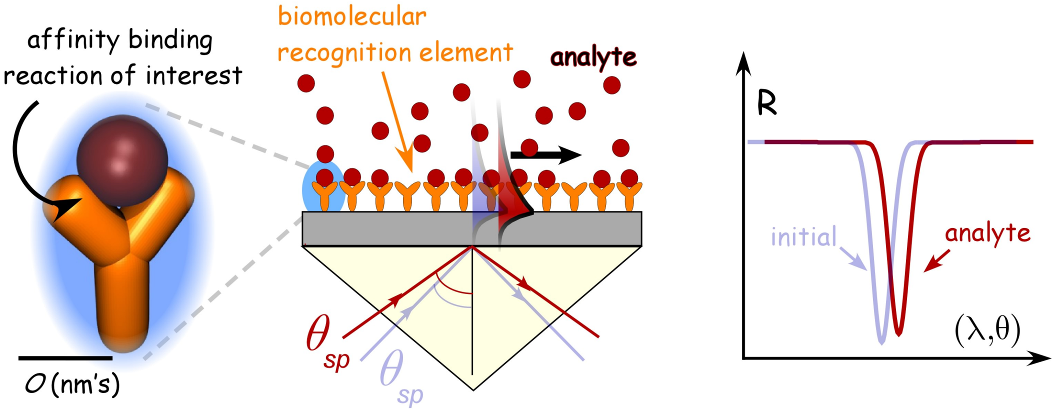

(a) (b) (c)

Figure VII.1: Conventional SPR sensor based on the Kretchsmann-Raether geometry. (a) Cartoon depiction of typical affinity binding reaction of interest. (b) Kretchsmann-Raether geometry with biochemically coated metal film directly on high index of refraction media (prism). (c) Readout spectra for monitoring SPR signal based upon change in reflection parameters.

lar recognition element, and an analyte species is flowed across the surface. While this is occurring, the light reflected from surface metal surface is monitored as a function of either wavelength, angle, or intensity, as show in Fig. VII.1(c). These methods are also applicable when been used for detection of a surface perturbation when flowing fluid along the surface, as we will do in this work. This is effectively a concentration sensor.

More recent approaches have included phase sensitive variations, demonstrated in both interferometric [98] as well as ellipsometric [99] configurations. One major drawback with the conventional coupling methods, as shown in Fig. VII.1(b), is the difficulty in incorporating the sensor elements in high NA aperture imaging systems to increase spatial resolution and the corresponding number of resolvable spots. Operating on a prism or with a first or higher order diffraction mode places severe constraints on the depth of focus in the imaging system needed for large arrays of assays. Massive parallelism, and hence high throughput, is of primary importance in many potential SPR sensor applications but they are severely limited

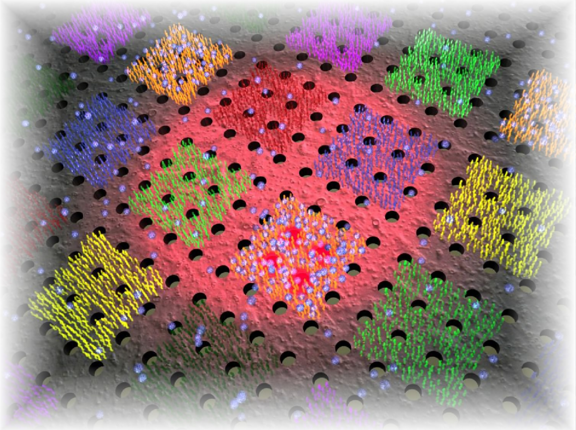

Figure VII.2: Conceptual diagram of SPR nanohole array sensor. Various biochemicals may be heterogeneously spotted or synthesized on metallic hole array surface. The entire area is imaged, and a change in the SPR resonance is detected where an affinity binding reaction occurs.

by most of the current design configurations [100, 101].

In addition the SPP propagation length is also a hindrance to creating high density, two-dimensional arrays. In order to separate the measurements of various regions on the surface, the different interrogation regions must be separated by an adequate distance, which is some appropriate number of SPP decay lengths δ_{SPP} as described by Eq. II.10.

VII.A.2 SPR nanohole sensor

Alternatively, we employ the subwavelength hole structures studied in the previous chapters. Such structures may be exploited for sensor applications due to their potential for decreasing significantly the interrogation volumes while operating at normal or near normal illumination. This leads to high packing density, minimal analyte volumes, and large number of parallel channels while facilitating high-resolution imaging and wide field of view, supporting a large space bandwidth product (SBP).

These advantages may make such devices preferable in a number of applications despite the fact that the ultimate spectral resolution is lower than the prism based equivalent due to SPR broadening due to both radiative and material damping. Several authors have suggested and demonstrated the use of subwavelength hole arrays for sensing applications [102, 103], and there are numerous numerical and experimental studies on their spectral properties.

In the rest of this chapter we demonstrate an SPR sensor based on a metal film, perforated by a nanohole array, and specifically show polarization properties that facilitate narrowing the transmission linewidth (and hence maximize resolution) while operating in a regime that facilitates high SBP imaging.

VII.B Sensor chip fabrication

The chips constructed by combination of a nanohole array on a substrate in combination with a flow channel.

VII.B.1 Microchannel fabrication

Samples for our experiments are fabricated by depositing gold films of $h \sim 200$ nm on glass substrate followed by spin coating and patterning by holographic lithography to achieve large usable areas (~ 1 cm^2). Multiple exposures of a chemically amplified negative resist (SU-8) yields a 2-D array of nanoholes, and the exposure time and post-exposure baking step allow fine control of the hole diameter ($d \sim 200$ nm). To facilitate large SBP imaging, we choose the period a of the array to be close to the wavelength l of the excitation field ($a/\lambda \sim 1$) with the fabricated value of $a = 1.4$ μm. We then make a Polydimethylsiloxane (PDMS) channel and bond to the chip, which we describe next.

With the advent of soft lithography and rapid prototyping the silicon elastomer PDMS has become a material of choice for many microfluidic R&D and lab-on-a-chip applications. The devices made of PDMS are inexpensive and their fabrication does not require high-level facilities. PDMS has quite low Youngs modulus that allows thin flexible membranes. The flexible elastomer membranes

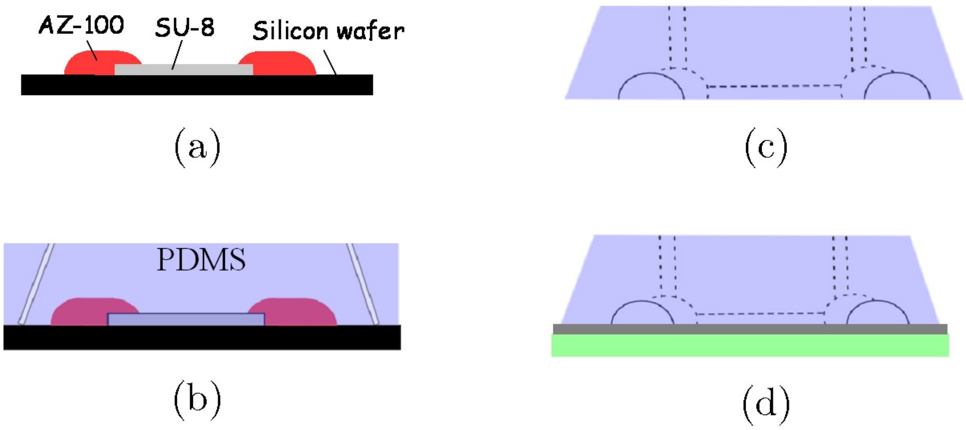

(a) (c)

(b) (d)

Figure VII.3: (a) First mask to make SU-8 mirror mold, Second mask to make AZ-100 flow mold (b) PDMS casting (c) PDMS punch for inlets and outlets (d) bonding to nanostructured metallic chip

are also a key element in pressure-actuated micro-valves that can be integrated in the microfluidic devices.

The molds were fabricated by regular near-UV contact photolithography using 8000 dpi resolution masks designed to implement the desired geometry of the molds. To make the master mold for the flow layer, a 4 in. silicon wafer was first spin coated with 75 μmlayer of a negative photoresist (SU8-2050 by MicroChem) and patterned through a photomask. That produced flat parallel relief to cast the mirror channels. Next, the wafer was coated with about 100 μmlayer of a positive resist, AZ100 XT by Clariant. It was patterned through another photomask (aligned with respect to the 75 mm SU8 layer), and baked on a 140 hot plate for 30 min after development to round the AZ 100XT relief [see Fig. VII.3(a)]. Holes were then punched in the chips with a gauge 16 luer stub to make ports for the flow layer.

There are a number of other fluidic chip design that provide functionality but were not utilized to this point in this work. A second inlet port could provide. The other inlet ports, numbered 1-5, act as pressure controlled, fluidic switches to control the flow of the inlet and outlet ports. In addition, one could easily utilize the same process to incorporate a larger number of sensor channels for measuring

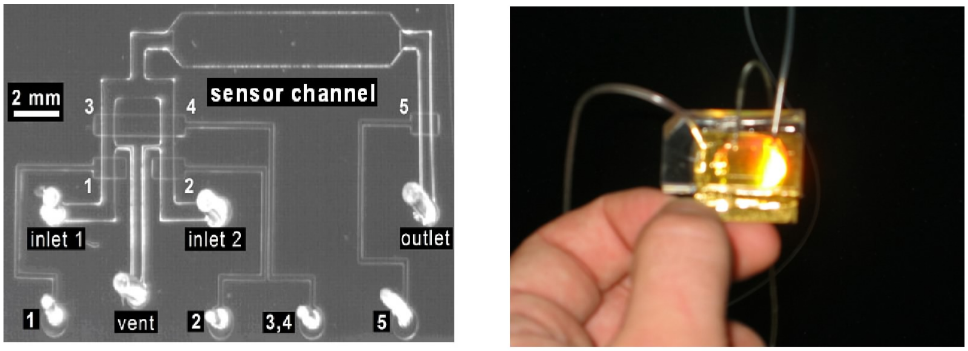

(a) (b)

Figure VII.4: (a) Photograph of the microfluidic channel structure. The sensor channel has dimensions: width: 2 mm, length: 10 mm, depth: 75 μm. (b) Photograph of the final chip with PDMS microfluidic channels bonded to the metal/glass substrate

a number of analytes in the same measurement, or to employ a buffer or wash solution to apply between the addition of various analytes and to measure the kinetics or dissociation.

A photograph of the PDMS microchannel structure is shown in Fig. VII.4(a). The sensor channel has dimensions width: 2 μm, length: 10 μm, depth: 75 μm

The PDMS channel is treated with oxygen plasma and pressed to the substrate layer for bonding. When pressed directly to a continuous gold layer, the resulting structure is mechanically unstable, and the PDMS channel layer is easily pealed away from the substrate, and only very low fluidic pressures may be used. For improved boding, the gold from the substrate outside of the sensor region may be removed to apply the oxygen plasma treatment to both surfaces and increase the bond strength. In this case, and there is no resulting leakage from the device during any of the subsequent measurements. A photograph of the final bonded chip structure is shown in Fig. VII.4(b).

The liquids were held in 60 cm^3 plastic syringes, mounted vertically and connected to the elastomer chip by flexible tygon tubing with an inner diameter of 1 mm. Both the inlet and outlet and syringes were open to the atmosphere, and

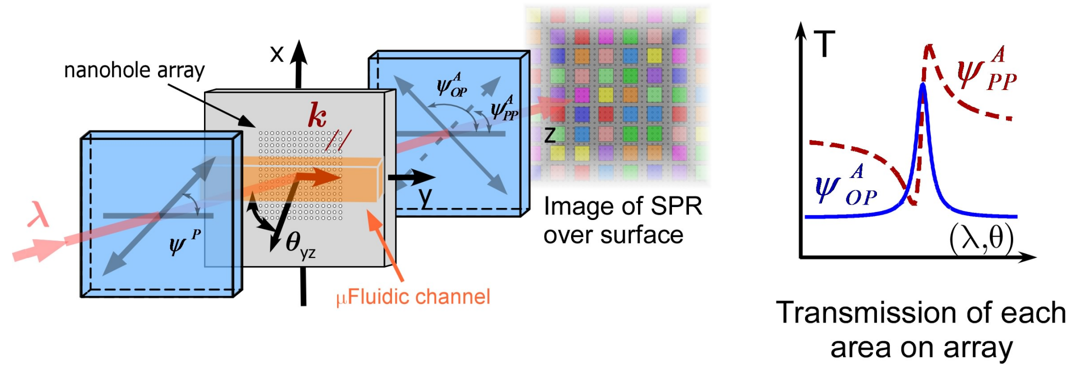

(a) (b)

Figure VII.5: (a) Schematic diagram of the 2D nanohole array based SPR sensor. The input and output polarization states of a tunable laser are controlled A microfludic channel is used to transports the analyte fluid to the surface of the sensing area and can be used to control the refractive index on the metal-dielectric interface to tune the SPP resonance frequency. (b) The polarization states change of the input and output field change the spectral or angular Fano-type profiles of the measured transmission profiles

relative heights were used to control the flow rate.

VII.C Device characterization

VII.C.1 Measurement setup

Measurements are carried out using the simple setup shown in Fig. VII.5 where the collimated, tunable laser source (see Sec. IV.B.1 of $\sim$ 1 cm in diameter is used to excite the SPP field in the 2-D nanohole array. This measurement is the same as that shown in Sec. IV.B.3, Fig. IV.4, only through the microfluidic channel.

The sample is inserted between a polarizer-analyzer pair and the transmitted light is used to simultaneously image an area of $\sim 200 \times 200$ μmof the sample onto an InGaAs camera for alignment as well as a photodiode for transmission measurements. Angular interrogation is achieved using a mechanical rotation

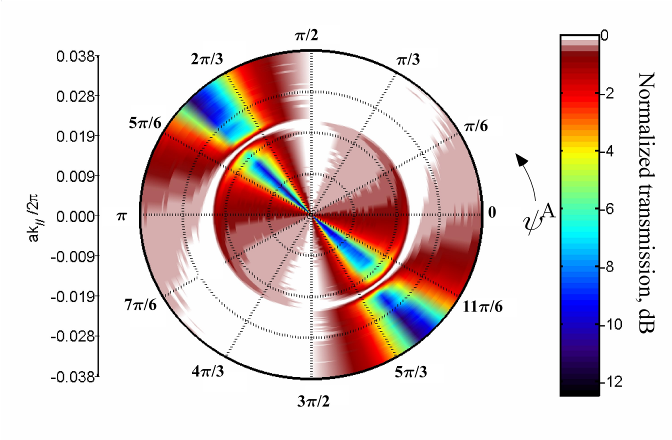

Figure VII.6: Normalized nanohole transmission, plotted on a log scale, shows the resolution enhancement for the OP measurement conditions.

stage rotating the sample in the y-z plane. We refer to two polarization states in our measurements: 1) parallel polarizer-analyzer (PP): polarizer and analyzer axes are parallel and oriented at $+\pi/4$ with respect to the (1,0) direction of the nanohole array (see Fig. 1) yielding equal electric field amplitudes in the $x-$ and $y-$ directions, and 2) orthogonal polarizer-analyzer (OP): polarizer (analyzer) axis is oriented at $+\pi/4$ $(-\pi/4)$ with respect to the (1,0) direction. Resonant transmittance through the 2D nanohole array depends on the interrogation angle and wavelength of radiation, and has a Fano-type lineshape for PP and a Lorentzian shape for OP (see Sec. IV.B.3, Fig. IV.13). There have been a number of studies that have investigated and explained the effects of the various geometric parameters on the shape of the resonant transmission (e. g., hole size, metal film thickness, and optical properties of the metal), and we note that the critical feature (assume a relatively "thick" film, STC) is the hole diameter, which increases the scattering rate and hence broadens the resonance linewidth.

We observe the characteristic Fano shape for PP (dotted lines) and a pure Lorentzian shape for OP (solid)- with OP the background contribution is suppressed leaving only the resonance component of the transmission. This data is shown again in Fig. VII.6 The absolute transmittance is low, -23 dB (0.50%) for

PP, due to the small size of the diameter of the holes (thus yielding relatively narrow lines), and drops to about -29 dB (0.13%) for OP due to additional polarization projection onto the analyzer. The extinction ratio of $\sim 15-20$ dB is limited by the linewidth as well as depolarization due to surface roughness in the etched holes. Under wavelength interrogation the background level does not drop to the same deep minimum levels within the tuning range of our laser. The measured full-width at half-maximum (FWHM) for wavelength interrogation are 1.28 meV (2.47 nm) and -2.86 meV (5.53 nm) for OP and PP, respectively, and the PP transmission peak is red-shifted from that in OP by $0.40\, meV (0.77\, nm)$. Similarly, the measured FWHM for angular interrogation (Fig. 2b) are 0.0012 $ak_{//}/2\pi$ (0.092) and 0.011 (0.87) for OP and PP, respectively, and the corresponding peak shift is 0.0005 (0.04).

VII.C.2 Linewidth broadening in aqueous environment

Most of the relevant surface interactions of interest occur in a water based environment. However, because of the wavelength of the high resolution, tunable telecom laser we utilize from 1520-1570 nm, the SPP waves that are excited on this surface are further damped because of the strong absorption of water in this wavelength range. This adds an extra material loss component which one can analyze in the same manner as presented in Sec. II.B- though with an absorptive, lossy dielectric function as opposed to one with gain. In addition, there is reduced scattering from any surface roughness at because of the higher real part of dielectric constant. Because of this multitude of factors, it is rather difficult incorporate all of these effects into our models.

It is rather straightforward, however, to measure the transmission, with both an air overlayer and water overlayer, and deduce that the resulting broadening of the resonance linewidth is due to this extra material damping factor. An example of this linewidth broadening is shown in Fig. VII.7.

Here the data has been normalized to its maximum value, and plotted as

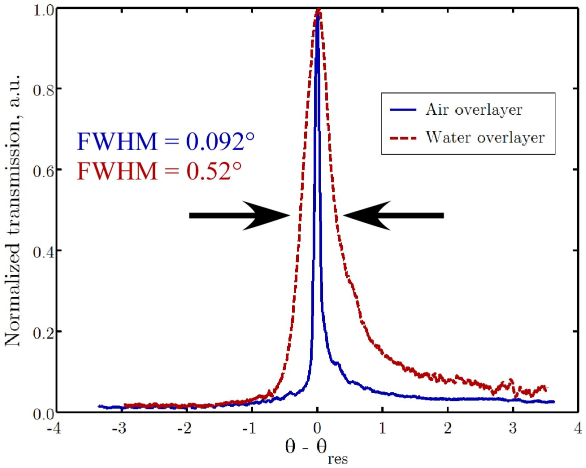

Figure VII.7: Resonance transmission linewidth comparison for an air overlayer and water overlayer

a function of the relative angle with respect to its maximum transmission value. With this representation we can clearly see the linewidth broadening from a FWHM of 0.092° with air in the channel to 0.52° with water. A similar analysis can be applied to the transmission linewidths for both wavelength and angular tuning, and both PP and OP measurement configurations. This analysis has been carried out will be presented in its entirety in the next section with the full sensor characterization results.

VII.C.3 Tuning of index of refraction and sensor analysis

Next we explore the resonant transmission through 2D nanohole array for sensor applications by introducing an index-calibrated solution through the microfluidic channel to create a controlled gold-fluid interface. We repeat our experiments on angular and wavelength interrogation exciting the (+1,0) type SPP modes and vary the refractive index of the overlayer fluid (varying concentrations of Na_2CrO_4 in H_2O).

Since the resolving power and interrogation range are both higher in angular interrogation, we focus our following study on it. Fig. VII.9 shows experimental

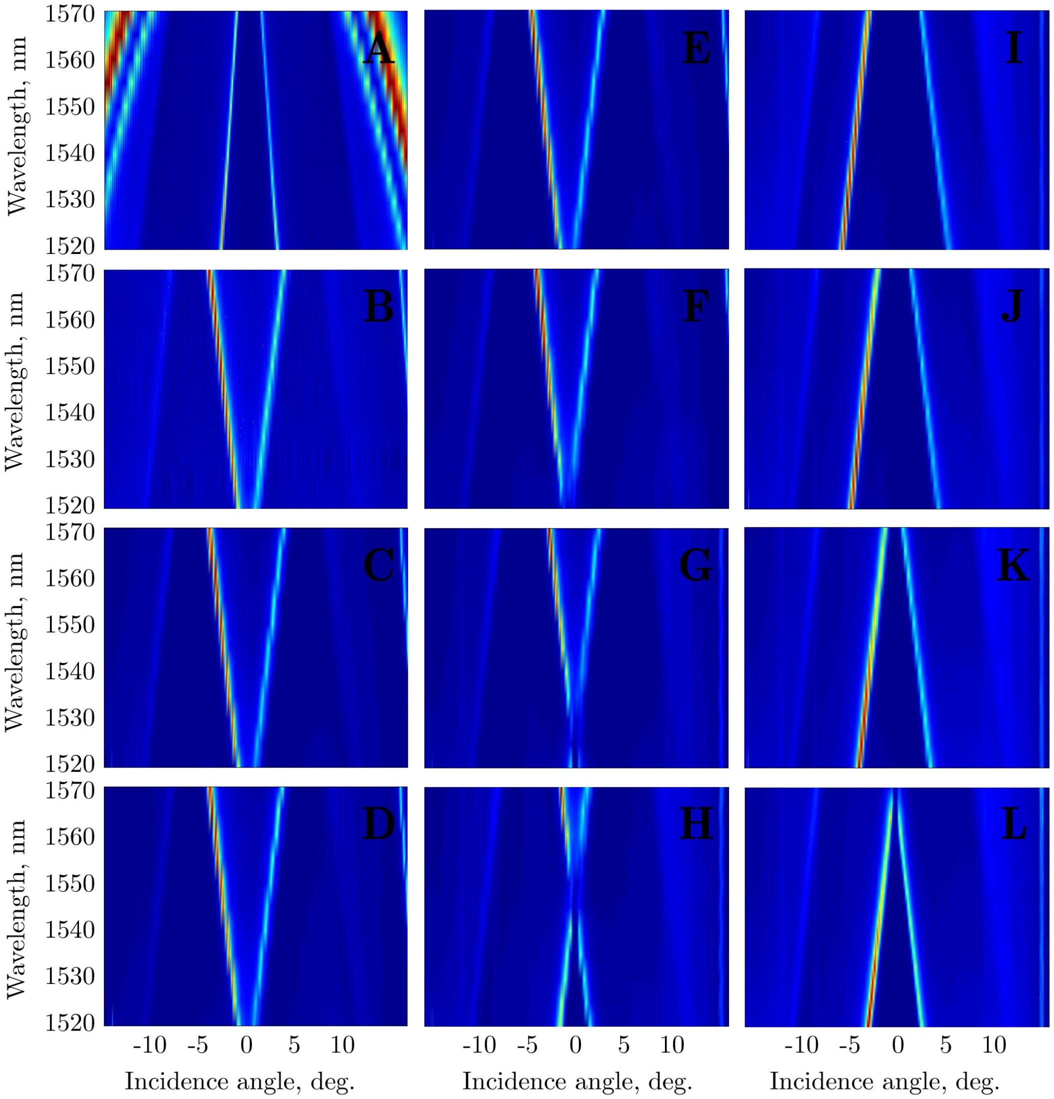

Figure VII.8: Transmission as function of angle and wavelength for various salt concentrations. The first two measurements show (a) an air overlayer, and (b) pure water. Different concentrations of salt in the fluidic overlayer. The other images correspond to a salt concentration of (weight percent) of: (c) 1.0×10^{-4} (b) 1.0×10^{-3} (c) 0.01 (d) 0.05 (e) 0.1 (f) 0.5 (g) 0.1 (h) 0.2 (i) 0.3 (j) 0.4 (k) 0.5 (l) 0.6

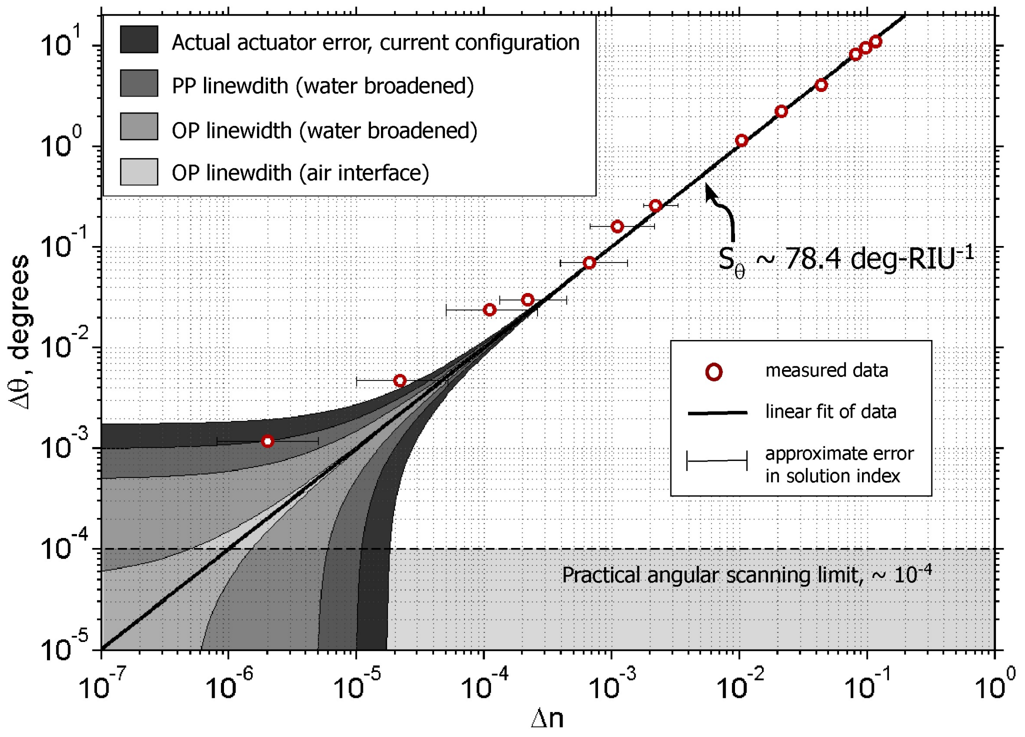

Figure VII.9: Resonance peak position shift versus refractive index change (i.e. salt concentration in water) in the fluidic overlayer. The black line is a linear fit to the datum. Shaded regions correspond to approximate peak position (absolute refractive index) errors in the fitting procedure for the OP and PP conditions for both air and water broadened linewidths as well as estimated theoretical resolution limits.

results on position of the resonant transmission peak through angular interrogation vs. the index of refraction of the fluid on the interface. As discussed in Sec. VII.C.2, due to the strong absorption of water in this wavelength range, the FWHM for wavelength and angular interrogation broaden to values of 4.32 meV (8.31 nm) and 0.0064 $ak_{//}/2\pi$ (0.52), respectively, with OP.

At shorter wavelengths the damping due to water is reduced- however the metal losses are larger. Also, at shorter wavelengths there is a greater mode overlap of the resonant field with the reaction of interest as the extent of the mode into the dielectric is reduced.11 We note that one may well monitor another position on this curve, for example the point of highest slope in the PP (at approximately the SPP resonance position), but by usual convention we monitor the resonance maxima. Error bars in the horizontal direction are from uncertainty in the solution index of refraction as well as possible variations in temperature. Peak positions are determined by both the method of moments (centroid position) and by fitting Lorentzian functions, and the error bounds for these methods in the presence of noise are shown as the various shaded regions. This procedure corresponds to estimated sensing limits of 5×10^{-6} RIU and 1×10^{-5} RIU for OP and PP, respectively. The darkest region corresponds to the observed error 1.7×10^{-3} (standard deviation) due to lack of full optimization in the feedback controls, and therefore limited our direct measurement limit to $\sim 1.5 \times 10^{-5}$. We estimate the limits for a nonabsorbing overlayer (with a gaseous species analyte, for example) with OP and an optimized rotation stage (mechanical limits of $\sim 10^{-4}$ in angle [97]) to be on the order 1×10^{-6} which is shown with the lightest shading. While peak position is typically determined more precisely, it is useful to introduce the metric

$$\chi_{\lambda,\theta} = \frac{S_{\lambda,\theta}}{\Gamma_{\lambda,\theta}}, \tag{VII.1}$$

which is a measure of the resolving power that facilitates comparisons of different sensors and interrogation methods. Here S is the sensitivity (i.e. derivative of resonance position with respect to index of refraction, $d\theta_{res}/d\Delta n$), Γ is the FWHM, and the subscripts λ and θ) refer to wavelength and angular interrogation, respectively. We experimentally determine $S_\lambda = 1022 \pm 8$ nm-RIU^{-1} and $S_\theta = 78.4 \pm 0.6$ deg-RIU^{-1} that yield values of $\chi_\theta \sim 850$ RIU^{-1} and $\chi_\lambda \sim 410$ RIU^{-1} with an air overlayer while these values are reduced to $\chi_\theta \sim 150$ RIU^{-1} and $\chi_\lambda \sim 120$ RIU^{-1} with water broadened transmission. These values compare favorably to values of $\chi_\lambda \sim 108$ (48) RIU^{-1} and $\chi_\lambda \sim 83$ (48) RIU^{-1} for prism (grating) based sensors, respectively, at 850 nm [97]. All of these values are summarized in Tab. VII.1 for reference.

In working towards utilizing this structure as a biochemical sensor, we have also measured a protein green fluorescent protein (GFP) with a molecular

Table VII.1: Resolving power results for nanohole array SPR sensor using calibrated salt solution. These results are compared to values taken in a review of the literature.

χ, RIU^{-1}	wavelength	angle	notes
This work (@1500 nm)	410 (120)	850 (150)	air (water) overlayer
Comparision (@850 nm)	48 (108)	48 (83)	grating (prism) based [97]

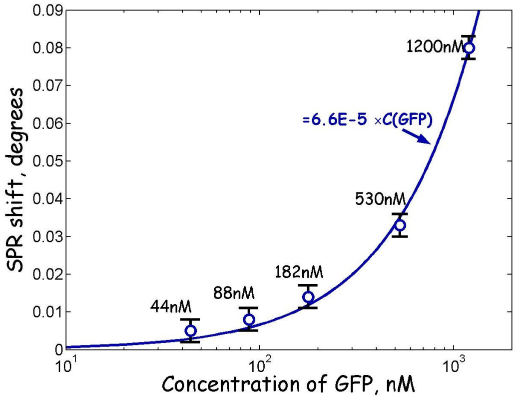

Figure VII.10: Sensor resonance position as a function of green fluorescent protein concentration.

weight of ∼ 28 kDa with results shown in Fig.VII.10. Further work, which is ongoing, seeks to bind a biochemical to the surface and measure an affinity binding reaction with this structure in real time. Very preliminary results, which are not included in this work, with the BSA/Anti-BSA complexes have been promising.

The text of Chapter Seven in part is a reprint of the material as it appears in the following publication:

- K. Tetz, L. Pang, and Y. Fainman, "High-resolution surface plasmon resonance sensor based on linewidth-optimized nanohole array transmittance",Opt. Lett. 31, 1528-1530 (2006).

The dissertation author was the primary researcher and author. The co-authors listed in these publications directed and supervised the research which forms the basis for this chapter.

VIII

Summary and future directions

In this dissertation we have presented a number of contributions to the study of SPP modes on nanohole arrays. We began by investigating the propagation of SPPs across different metal-dielectric configurations in the presence of gain in the dielectric medium. The analytic analysis and numeric simulation results show that the gain medium assists the SPP propagation by compensating for the metal losses, making it possible to propagate SPPs with little or no loss on metal boundaries and guides.

Next, we have presented a detailed, high resolution study of the polarization properties in spectral transmittance of a nanohole array grating in a metal film. To describe the measured data, we have extended the explanation of transmission through nanohole arrays in terms of Fano-type lineshapes resulting from the coherent interference between a discrete and a continuum of states. In particular, we have shown that these components may be weighted- in amplitude and phase- by control of polarization resulting in Fano-type lines with various symmetries and detuning values. While we have shown results for the specific case of a single (1,0) type orders, and derived an analytic expression which fit our measured results quite well, a similar analysis may be applied to any of the various resonant orders, generalized, or applied to periodic structures of different symmetries. It will be of further interest to investigate similar structures at higher frequencies, towards the plasma frequency, where localized surface plasmons and related effects become more pronounced [60].

We then demonstrated the coupling to SPP modes in a cubic array of holes and the direct observation of leaky radiation from such arrays. A wide variety of propagating waves, with different frequencies and in-plane wave vectors can be excited and observed for various sample geometries and under variable excitation conditions. Such techniques may prove useful for investigating the properties of SPP waves for a variety of applications and in interfacing with various nanoplasmonic devices.

We extended this technique to the excitation and characterization of ultrafast SPP pulses, propagating on the surface of the nanostructured metallic film. Optical pulses were coupled from free space into various surface modes using a 2-dimensional array of circular nanoholes. Spatial amplitude and phase characteristics of the scattered surface field are measured with femtosecond scale time resolution. Due to optical field correlation nature of our measurements, only spatial amplitude and phase information of the SPP field can be measured precisely. We envision, however, two-photon absorption realization of our measurements with the possibility of characterizing temporal amplitude and phase of the femtosecond SPP pulses. Demonstrated in-plane focusing of SPP pulse provides additional electromagnetic field localization with possible applications in SPP nanophotonics, nonlinear surface dynamics, biochemical sensing and ultrafast surface studies. In the future, the ultrafast SPP combined with optofluidics will have a significant impact on various applications including nanometrology, nanoscale spectroscopy, live cell dynamics, sensing, hyper-spectral imaging of biological species and nanotomography. Investigation of opto-plasmonic fields and their control on a nanoscale has the potential to lead to new tools to further advance cell biology and medicine.

Finally we have demonstrated a high resolution SPR sensor based on transmission through nanohole arrays. The transmission lineshape function was shown to vary with the input and output polarization states- showing Fano-like dependence with a pure resonant Lorentzian of minimal width when these two states are orthogonal. In these structures, the SPP propagation length may be reduced, from approximately several 10s of μmin this case, to increase the spatial resolution and limit the crosstalk between channels. This leads to a design tradeoff where the spectral or angular resolution (resolving power) may be sacrificed for smaller interrogation volumes depending on the particular application. In addition, one can break the in plane symmetry and use, for example, elliptical [Ref. [17], and Sec. III.C.3] or chiral shaped holes to have polarization dependence even at normal incidence. These results will help in designing future grating coupled surface plasmon resonance sensors, both in the transmission (a nanohole) and the traditional (reflection surface grating relief) geometries. It may be of significant interest to investigate various configurations where there is interference between two or more modes. In many cases, coupling between the modes may lead to linewidth narrowing and increased resolution, as shown in Sec. IV.C.4. Quasiperiodic structures, as shown in Sec. III.C.3, may also be useful for both linear and nonlinear optical spectroscopy due to presence of both extended and localized modes within the same structure. The highly multiplexed sensor should prove useful for a number of highthroughput, combinatorial biochemical studies.

Bibliography

[1] H. Raether, *Surface Plasmons on Smooth and Rough Surfaces and on Gratings* (Springer-Verlag, 1988).

[2] W. L. Barnes, A. Dereux, and T. W. Ebbesen, "Surface plasmon subwavelength optics," Nature **424**(6950), 824–830 (2003).

[3] H. Ditlbacher, J. R. Krenn, G. Schider, A. Leitner, and F. R. Aussenegg, "Two-dimensional optics with surface plasmon polaritons," Applied Physics Letters **81**(10), 1762–1764 (2002).

[4] S. A. Maier, M. L. Brongersma, P. G. Kik, S. Meltzer, A. A. G. Requicha, and H. A. Atwater, "Plasmonics - A route to nanoscale optical devices," Advanced Materials **13**(19), 1501–+ (2001).

[5] W. L. Barnes, S. C. Kitson, T. W. Preist, and J. R. Sambles, "Photonic surfaces for surface-plasmon polaritons," Journal of the Optical Society of America a-Optics Image Science and Vision **14**(7), 1654–1661 (1997).

[6] W. L. Barnes, T. W. Preist, S. C. Kitson, and J. R. Sambles, "Physical origin of photonic energy gaps in the propagation of surface plasmons on gratings," Physical Review B **54**(9), 6227–6244 (1996).

[7] R. A. Shelby, D. R. Smith, and S. Schultz, "Experimental verification of a negative index of refraction," Science **292**(5514), 77–79 (2001).

[8] J. B. Pendry, "Negative refraction makes a perfect lens," Physical Review Letters **85**(18), 3966–3969 (2000).

[9] T. W. Ebbesen, H. J. Lezec, H. F. Ghaemi, T. Thio, and P. A. Wolff, "Extraordinary optical transmission through sub-wavelength hole arrays," Nature **391**(6668), 667–669 (1998).

[10] H. F. Ghaemi, T. Thio, D. E. Grupp, T. W. Ebbesen, and H. J. Lezec, "Surface plasmons enhance optical transmission through subwavelength holes," Physical Review B **58**(11), 6779–6782 (1998).

[11] L. Martin-Moreno, F. J. Garcia-Vidal, H. J. Lezec, K. M. Pellerin, T. Thio, J. B. Pendry, and T. W. Ebbesen, “Theory of extraordinary optical transmission through subwavelength hole arrays,” Physical Review Letters **86**(6), 1114–1117 (2001).

[12] W. L. Barnes, W. A. Murray, J. Dintinger, E. Devaux, and T. W. Ebbesen, “Surface plasmon polaritons and their role in the enhanced transmission of light through periodic arrays of subwavelength holes in a metal film,” Physical Review Letters **92**(10) (2004).

[13] H. Bethe, “Theory of diffraction by small holes,” Physical Review **66**, 163–182 (1944).

[14] C. Bouwkamp, “Diffraction Theory,” Rep. Prog. Phys. **17**, 35–100 (1954).

[15] H. J. Lezec, A. Degiron, E. Devaux, R. A. Linke, L. Martin-Moreno, F. J. Garcia-Vidal, and T. W. Ebbesen, “Beaming light from a subwavelength aperture,” Science **297**(5582), 820–822 (2002).

[16] Q. Cao and P. Lalanne, “Negative role of surface plasmons in the transmission of metallic gratings with very narrow slits,” Physical Review Letters **88**(5) (2002).

[17] J. Elliott, I. Smolyaninov, N. I. Zheludev, and A. V. Zayats, “Polarization control of optical transmission of a periodic array of elliptical nanoholes in a metal film,” Optics Letters **29**(12), 1414–1416 (2004).

[18] H. J. Lezec and T. Thio, “Diffracted evanescent wave model for enhanced and suppressed optical transmission through subwavelength hole arrays,” Optics Express **12**(16), 3629–3651 (2004).

[19] U. Fano, “Effects of configuration interaction on intensities and phase shifts,” Physical Review **124**, 1866–1878 (1961).

[20] D. Jackson, *Electrodynamics* (The Earth, 1975).

[21] N. Ashcroft and N. Mermin, *Solid State Physics* (Brooks Cole, 1976).

[22] C. Vassalo, *Optical waveguide concepts* (Elsevier, 1991).

[23] F. Fernandez and Y. Lu, *Microwave and optical waveguide analysis by the finite element method* (Wiley, 1996).

[24] G. A. Plotz, H. J. Simon, and J. M. Tucciarone, “Enhanced Total Reflection With Surface-Plasmons,” Journal Of The Optical Society Of America **69**(3), 419–421 (1979).

[25] B. Y. Kogan, V. M. Volkov, and S. A. Lebedev, "Superluminescence And Generation Of Stimulated Radiation Under Internal-Reflection Conditions," Jetp Letters-Ussr **16**(3), 100 (1972).

[26] A. Sudarkin and P. Demkovich, "Excitation of surface electromagnetic waves on the boundary of a metal with an amplifying medium," Sov. Phys.Tech. Phys. **34**, 764–766 (1989).

[27] C. Sirtori, C. Gmachl, F. Capasso, J. Faist, D. L. Sivco, A. L. Hutchinson, and A. Y. Cho, "Long-wavelength (lambda approximate to 8-11.5 mu m) semiconductor lasers with waveguides based on surface plasmons," Optics Letters **23**(17), 1366–1368 (1998).

[28] E. Palik, *Handbook of Optical Constants of Solids*, Academic Press Handbook Series (Academic, Orlando, Fla., 1985).

[29] T. Saitoh and T. Mukai, "1.5 Mu-M Gainasp Traveling-Wave Semiconductor-Laser Amplifier," Ieee Journal Of Quantum Electronics **23**(6), 1010–1020 (1987).

[30] N. Hatori, M. Sugawara, K. Mukai, Y. Nakata, and H. Ishikawa, "Room-temperature gain and differential gain characteristics of self-assembled InGaAs/GaAs quantum dots for 1.1-1.3 mu m semiconductor lasers," Applied Physics Letters **77**(6), 773–775 (2000).

[31] K. Wundke, J. Auxier, A. Schulzgen, N. Peyghambarian, and N. F. Borrelli, "Room-temperature gain at 1.3 mu m in PbS-doped glasses," Applied Physics Letters **75**(20), 3060–3062 (1999).

[32] P. Ramvall, Y. Aoyagi, A. Kuramata, P. Hacke, K. Domen, and K. Horino, "Doping-dependent optical gain in GaN," Applied Physics Letters **76**(21), 2994–2996 (2000).

[33] H. Raether, *Excitation of Plasmons and Interband Transitions by Electrons*, vol. 88 of *Springer Tracts in Modern Physics* (Springer, Berlin, Heidelberg, New York, 1980).

[34] J. Sambles, G. Bradbery, and F. Yang, "Optical Excitation of Surface Plasmons: an Introduction," Contemporary Physics **32**(3), 173–183 (1991).

[35] R. H. Ritchie, E. T. Arakawa, J. J. Cowanand, and R. N.Hamm, "Surface-plasmon resonance effect in grating diffraction," Phys. Rev. Lett. **21**, 15301533 (1968).

[36] K. E. and R. H., "Radiative decay of nonradiative surface plasmons excited by light," Z. Naturforsch. A **23**, 21352136 (1968).

[37] A. Otto, “Exitation of nonradiative surface plasma waves in silver by the method of frustrated total reflection,” Z. Phys. **216**, 398 (1968).

[38] M. Sun, R. J. Liu, Z. Y. Li, B. Y. Cheng, D. Z. Zhang, H. F. Yang, and A. Z. Jin, “The influence of hole shape on enhancing transmission through subwavelength hole arrays,” Chinese Physics **15**(7), 1591–1594 (2006).

[39] A. Degiron, H. J. Lezec, W. L. Barnes, and T. W. Ebbesen, “Effects of hole depth on enhanced light transmission through subwavelength hole arrays,” Applied Physics Letters **81**(23), 4327–4329 (2002).

[40] D. E. Grupp, H. J. Lezec, T. W. Ebbesen, K. M. Pellerin, and T. Thio, “Crucial role of metal surface in enhanced transmission through subwavelength apertures,” Applied Physics Letters **77**(11), 1569–1571 (2000).

[41] C. Genet, M. P. van Exter, and J. P. Woerdman, “Fano-type interpretation of red shifts and red tails in hole array transmission spectra,” Optics Communications **225**(4-6), 331–336 (2003).

[42] H. C. Guo, D. Nau, A. Radke, X. P. Zhang, J. Stodolka, X. L. Yang, S. G. Tikhodeev, N. A. Gippius, and H. Giessen, “Large-area metallic photonic crystal fabrication with interference lithography and dry etching,” Applied Physics B-Lasers And Optics **81**(2-3), 271–275 (2005).

[43] N. D. Lai, W. P. Liang, J. H. Lin, C. C. Hsu, and C. H. Lin, “Fabrication of two- and three-dimensional periodic structures by multi-exposure of two-beam interference technique,” Optics Express **13**(23), 9605–9611 (2005).

[44] M. J. Escuti and G. P. Crawford, “Holographic photonic crystals,” Optical Engineering **43**(9), 1973–1987 (2004).

[45] Y. Q. Wang, Y. Y. Wang, S. Feng, and Z. Y. Li, “The effect of short-range and long-range orientational orders on the transmission properties of quasiperiodic photonic crystals,” Europhysics Letters **74**(1), 49–54 (2006).

[46] X. Wang, J. Xu, J. C. W. Lee, Y. K. Pang, W. Y. Tam, C. T. Chan, and P. Sheng, “Realization of optical periodic quasicrystals using holographic lithography,” Applied Physics Letters **88**(5) (2006).

[47] S. P. Gorkhali, J. Qi, and G. P. Crawford, “Switchable quasi-crystal structures with five-, seven-, and ninefold symmetries,” Journal Of The Optical Society Of America B-Optical Physics **23**(1), 149–158 (2006).

[48] Y. Q. Wang, S. S. Jian, S. Z. Han, S. Feng, Z. F. Feng, B. Y. Cheng, and D. Z. Zhang, “Photonic band-gap engineering of quasiperiodic photonic crystals,” Journal Of Applied Physics **97**(10) (2005).

[49] R. C. Gauthier and K. Mnaymneh, "Photonic band gap properties of 12-fold quasi-crystal determined through FDTD analysis," Optics Express **13**(6), 1985–1998 (2005).

[50] M. Hase, H. Miyazaki, M. Egashira, N. Shinya, K. M. Kojima, and S. Uchida, "Isotropic photonic band gap and anisotropic structures in transmission spectra of two-dimensional fivefold and eightfold symmetric quasiperiodic photonic crystals," Physical Review B **66**(21) (2002).

[51] M. Hase, M. Egashira, N. Shinya, H. Miyazaki, K. M. Kojima, and S. Uchida, "Optical transmission spectra of two-dimensional quasiperiodic photonic crystals based on Penrose-tiling and octagonal-tiling systems," Journal Of Alloys And Compounds **342**(1-2), 455–459 (2002).

[52] T. Tokihiro and H. Ezaki, "The effects of quasiperiodic grating on surface-plasmon polariton," Solid State Communications **96**(2), 73–78 (1995).

[53] M. Notomi, H. Suzuki, T. Tamamura, and K. Edagawa, "Lasing action due to the two-dimensional quasiperiodicity of photonic quasicrystals with a penrose lattice," Physical Review Letters **92**(12), 100–104 (2004).

[54] F. Przybilla, C. Genet, and T. W. Ebbesen, "Enhanced transmission through Penrose subwavelength hole arrays," Applied Physics Letters **89**(12), 121,115 (2006).

[55] F. Issue, "Extraordinary Light Transmission Through Sub-Wavelength Structured Surfaces," Optics Express **12**, 3618–3706 (2004).

[56] A. Hessel and A. A. Oliner, "A New Theory Of Woods Anomalies On Optical Gratings," Applied Optics **4**(10), 1275–1292 (1965).

[57] M. Sarrazin, J. P. Vigneron, and J. M. Vigoureux, "Role of Wood anomalies in optical properties of thin metallic films with a bidimensional array of subwavelength holes," Physical Review B **67**(8) (2003).

[58] K. A. Tetz, L. Pang, and Y. Fainman, "High-resolution surface plasmon resonance sensor based on linewidth-optimized nanohole array transmittance," Optics Letters **31**(10), 1528–1530 (2006).

[59] F. J. Garca de Abajo, S. J. J., C. I., and J. S. Dolado, "Site and lattice resonances in metallic hole arrays," Optics Express **14**(1), 7–18 (2006).

[60] S. H. Chang, S. K. Gray, and G. C. Schatz, "Surface plasmon generation and light transmission by isolated nanoholes and arrays of nanoholes in thin metal films," Optics Express **13**(8), 3150–3165 (2005).

[61] D. S. Kim, S. C. Hohng, V. Malyarchuk, Y. C. Yoon, Y. H. Ahn, K. J. Yee, J. W. Park, J. Kim, Q. H. Park, and C. Lienau, "Microscopic origin of surface-plasmon radiation in plasmonic band-gap nanostructures," Physical Review Letters **91**(14) (2003).

[62] S. J. Elston, G. P. Bryanbrown, and J. R. Sambles, "Polarization Conversion From Diffraction Gratings," Physical Review B **44**(12), 6393–6400 (1991).

[63] E. Altewischer, M. P. van Exter, and J. P. Woerdman, "Polarization analysis of propagating surface plasmons in a subwavelength hole array," Journal of the Optical Society of America B-Optical Physics **20**(9), 1927–1931 (2003).

[64] R. Rokitski, K. A. Tetz, and Y. Fainman, "Propagation of femtosecond surface plasmon polariton pulses on the surface of a nanostructured metallic film: Space-time complex amplitude characterization," Physical Review Letters **95**(17) (2005).

[65] R. Muller, V. Malyarchuk, and C. Lienau, "Three-dimensional theory on light-induced near-field dynamics in a metal film with a periodic array of nanoholes," Physical Review B **68**(20) (2003).

[66] V. Lomakin and E. Michielssen, "Enhanced transmission through metallic plates perforated by arrays of subwavelength holes and sandwiched between dielectric slabs," Physical Review B **71**(23), 235,117 (2005).

[67] V. Lomakin and E. Michielssen, "Transmission of transient plane waves through perfect electrically conducting plates perforated by periodic arrays of subwavelength holes," Ieee Transactions On Antennas And Propagation **54**(3), 970–984 (2006).

[68] A. V. Zayats, W. Dickson, I. Smolyaninov, and C. C. Davis, "Polarization superprism effect in surface polaritonic crystals," Applied Physics Letters **82**(25), 4438–4440 (2003).

[69] T. Thio, H. F. Ghaemi, H. J. Lezec, P. A. Wolff, and T. W. Ebbesen, "Surface-plasmon-enhanced transmission through hole arrays in Cr films," Journal of the Optical Society of America B-Optical Physics **16**(10), 1743–1748 (1999).

[70] E. Devaux, T. W. Ebbesen, J. C. Weeber, and A. Dereux, "Launching and decoupling surface plasmons via micro-gratings," Applied Physics Letters **83**(24), 4936–4938 (2003).

[71] C. Sonnichsen, A. C. Duch, G. Steininger, M. Koch, G. von Plessen, and J. Feldmann, "Launching surface plasmons into nanoholes in metal films," Applied Physics Letters **76**(2), 140–142 (2000).

[72] K. A. Tetz, R. Rokitski, M. Nezhad, and Y. Fainman, "Excitation and direct imaging of surface plasmon polariton modes in a two-dimensional grating," Applied Physics Letters **86**(11) (2005).

[73] E. Altewischer, X. Ma, M. P. van Exter, and J. P. Woerdman, "Fano-type interference in the point-spread function. of nanohole arrays," Optics Letters **30**(18), 2436–2438 (2005).

[74] S. Kawata, ed., *Near-Field Optics and Surface Plasmon Polaritons*, vol. 81 of *Topics in Applied Physics* (Springer-Verlag Berlin Heidelberg, Berlin Heidelberg, 2001).

[75] H. Ditlbacher, J. R. Krenn, N. Felidj, B. Lamprecht, G. Schider, M. Salerno, A. Leitner, and F. R. Aussenegg, "Fluorescence imaging of surface plasmon fields," Applied Physics Letters **80**(3), 404–406 (2002).

[76] J. R. Krenn and J. C. Weeber, "Surface plasmon polaritons in metal stripes and wires," Philosophical Transactions of the Royal Society of London Series a-Mathematical Physical and Engineering Sciences **362**(1817), 739–756 (2004).

[77] B. Lamprecht, J. R. Krenn, G. Schider, H. Ditlbacher, M. Salerno, N. Felidj, A. Leitner, F. R. Aussenegg, and J. C. Weeber, "Surface plasmon propagation in microscale metal stripes," Applied Physics Letters **79**(1), 51–3 (2001).

[78] T. Goto, Y. Katagiri, H. Fukuda, H. Shinojima, Y. Nakano, I. Kobayashi, and Y. Mitsuoka, "Propagation loss measurement for surface plasmon-polariton modes at metal waveguides on semiconductor substrates," Applied Physics Letters **84**(6), 852–854 (2004).

[79] A. Dogariu, T. Thio, L. J. Wang, T. W. Ebbesen, and H. J. Lezec, "Delay in light transmission through small apertures," Optics Letters **26**(7), 450–452 (2001).

[80] Y. E. Lozovik, S. P. Merkulova, M. M. Nazarov, A. P. Shkurinov, and P. Masselin, "Time-resolved nonlinear surface plasmon optics," JETP Letters **75**(9), 461–464 (2002).

[81] Y. H. Liau, S. Egusa, and N. F. Scherer, "Ultrafast interferometric measurements of plasmonic transport in photonic crystals," Optics Letters **27**(10), 857–859 (2002).

[82] M. van Exter and A. Lagendijk, "Ultrashort Surface-Plasmon and Phonon Dynamics," Physical Review Letters **60**(1), 49–52 (1988).

[83] R. Muller, C. Ropers, and C. Lienau, "Femtosecond light pulse propagation through metallic nanohole arrays: The role of the dielectric substrate," Optics Express **12**(21) (2004).

[84] R. Rokitski, P. C. Sun, and Y. Fainman, "Study of spatial-temporal characteristics of optical fiber based on ultrashort-pulse interferometry," Optics Letters **26**(15), 1125–1127 (2001).

[85] M. Centurion, Y. Pu, and T. W. H. Z. W. Liu, D. Psaltis, "Holographic recording of laser-induced plasma," Optics Letters **29**(7), 772–774 (2004).

[86] E. Altewischer, M. van Exter, and J. Woerdman, "Polarization analysis of propagating surface plasmons in a subwavelength hole array," J. Opt. Soc. Am. B **20**(9), 1927–31 (2003).

[87] V. Vlad and D. Malacara, *Direct spatial reconstruction of optical phase from phase-modulated images*, vol. XXXIII of *Progress in optics* (Elseiver Science B.V., 1994).

[88] M. Takeda and K. Mutoh, "Fourier transform profilometry for the automatic measurement of 3-D object shapes," Applied Optics **22**(24), 3977–82 (1983).

[89] K. Womack, "Frequency domain description of interferogram analysis," Optical Engineering **23**(4), 396–400 (1984).

[90] D. Bone, H. Bachor, and R. Sandeman, "Fringe-pattern analysis using a 2-D Fourier transform," Applied Optics **25**(10), 1653–60 (1986).

[91] T. Kreis, "Digital holographic interference-phase measurement using the Fourier-transform method," J. Opt. Soc. A. A **3**(6), 847–55 (1986).

[92] M. Takeda, *Spatial-carrier fringe-pattern analysis and its applications to precision interferometry and profilometry: An overview*, vol. 1 of *Industrial Metrology* (Elseiver, 1990).

[93] M. Takeda, H. Ina, and K. Kobayashi, "Fourier-transform method of fringe pattern analysis for computer-based topography and interferometry," J. Opt. Soc. Am. **72**(9), 156–60 (1982).

[94] M. Takeda and M. Kitoh, "Spatiotemporal frequency multiplex heterodyne interferometry," J. Opt. Soc. A. A **9**(9), 1607–14 (1992).

[95] K. Tetz, R. Rokitski, M. Nezhad, Y. Fainman, *Excitation and Direct Imaging of Surface Plasmon Polariton Modes in the Near-Infrared*, IEEE LEOS Annual Meeting.

[96] K. Tetz, R. Rokitski, M. Nezhad, and Y. Fainman, "Excitation and direct imaging of surface plasmon polariton modes in a two-dimensional grating," Appl. Phys. Lett. **86**, 111,110 (2005).

[97] J. Homola, S. S. Yee, and G. Gauglitz, "Surface plasmon resonance sensors: review," Sensors And Actuators B-Chemical **54**(1-2), 3–15 (1999).

[98] S. Y. Wu, H. P. Ho, W. C. Law, C. L. Lin, and S. K. Kong, "Highly sensitive differential phase-sensitive surface plasmon resonance biosensor based on the Mach-Zehnder configuration," Optics Letters **29**(20), 2378–2380 (2004).

[99] I. R. Hopper and J. R. Sambles, "Differential ellipsometric surface plasmon resonance sensors with liquid crystal polarization modulators," Applied Physics Letters **85**(15), 3017–3019 (2004).

[100] J. Dostalek, J. Homola, and M. Miler, "Rich information format surface plasmon resonance biosensor based on array of diffraction gratings," Sensors And Actuators B-Chemical **107**(1), 154–161 (2005).

[101] Y. D. Su, S. J. Chen, and T. L. Yeh, "Common-path phase-shift interferometry surface plasmon resonance imaging system," Optics Letters **30**(12), 1488–1490 (2005).

[102] A. G. Brolo, R. Gordon, B. Leathem, and K. L. Kavanagh, "Surface plasmon sensor based on the enhanced light transmission through arrays of nanoholes in gold films," Langmuir **20**(12), 4813–4815 (2004).

[103] T. Rindzevicius, Y. Alaverdyan, A. Dahlin, F. Hook, D. Sutherland, and M. Kall, "Plasmonic sensing characteristics of single nanometric holes," Nano Letters **5**(11), 2335–2339 (2005).